2013

Monitoring Damage Initiation And Growth In Composite Structures By Acoustic Emission Method

Kassahun Mekonnen Asamene
North Carolina Agricultural and Technical State University

Monitoring Damage Initiation and Growth in Composite Structures by Acoustic Emission Method

Kassahun Mekonnen Asamene

North Carolina A&T State University

A dissertation submitted to the graduate faculty

in partial fulfillment of the requirements for the degree of

DOCTOR OF PHILOSOPHY

Department: Mechanical Engineering

Major: Mechanical Engineering

Major Professor: Dr. Mannur Sundaresan

Greensboro, North Carolina

2013

School of Graduate Studies
North Carolina Agricultural and Technical State University
This is to certify that the Doctoral Dissertation of

Kassahun Mekonnen Asamene

has met the dissertation requirements of
North Carolina Agricultural and Technical State University

Greensboro, North Carolina
2013

Approved by:

Dr. Mannur Sundaresan Major Professor	Dr. John Kizito Committee Member
Dr. Frederick Ferguson Committee Member	Dr. Albert Esterline Committee Member
Dr. Janis Marie Oldham Committee Member	Dr. Devdas Pai Committee Member
Dr. Samuel Owusu-Ofori Department Chair	Dr. Sanjiv Sarin Dean, The Graduate School

Biographical Sketch

Kassahun Mekonnen Asamene was born on May 23, 1981, in Addis Ababa, Ethiopia. He received Bachelor of Science Degree in Mechanical Engineering from Faculty of Technology, Addis Ababa University (AAU) in 2004. He worked as teaching assistant at AAU for the years 2005 – 2008. He also received his Master of Science Degree in Mechanical Engineering in 2008 from Department of Mechanical Engineering, AAU. He was admitted to the Ph. D. program in Mechanical Engineering at North Carolina Agricultural and Technical State University in January 2009. He is a candidate for Ph.D. in Mechanical Engineering.

Dedication

I dedicate this Doctoral Dissertation to my mom and dad, Almaz and Mekonnen, my brother and sisters, Dawit, Hanna and Imuye for their continual support and prayers that have made this work successful.

Acknowledgements

I am very grateful to Almighty God for his gifts of knowledge, strength and energy that have made this Doctoral Dissertation possible. It is also with much appreciation and gratitude that I thank my academic advisor, Dr. M. J. Sundaresan, for his insights and directions to making this work successful.

I offer my regards and blessings to my colleagues Travis Whitlow, Letchuman Sripragash, Kumaran Gopal, Gene Warwick and other members of Intelligent Structures and Mechanisms (ISM) laboratory. I also would like to thank all those who supported me in any respect towards the completion of this work.

Table of Contents

List of Figures

List of Tables

Abstract

In this dissertation, acoustic emission technique is examined as candidate for monitoring the integrity of polymer matrix structural members. Acoustic emission technique has so far been largely limited to laboratory tests and field applications have been mostly limited to qualification tests of aerospace structures. The lack of quantitative indications of damage in composite structural members associated with the complex nature of damage in these materials has been a limiting factor. Generally, a number of failure modes operate simultaneously at a site of damage, and each of these failure modes generates a different type of acoustic emission signal. In addition, issues including anisotropic wave propagation including variation velocities and attenuation in composites leads to difficulties in damage location and assessment of damage magnitude. Further, extraneous noise that is invariably present when the structure is experiencing cyclic loading, increases the uncertainty in interpreting acoustic emission data. The goal of the present work is to address a few of these issues individually. They include (a) experimental measurement of attenuation of fundamental Lamb wave modes and frequency components of acoustic emission signal in representative composite laminates, (b) experimental characterization of friction related acoustic emission signals between two metallic surfaces, (c) monitoring and characterization of acoustic emission signal from delamination growth in coupon specimens and (d) numerical modeling of acoustic emission signals generated by different failure modes in a cross-ply laminate, including mode I and delaminations and matrix cracks. In this report, results and findings from each of the above works, both numerical and experimental are included..

CHAPTER 1

Introduction

Civil and mechanical structures are subjected to fatigue, overloading, impact and seismic loads, and environmental degrading agents which introduce damage. Design of the structures requires implementation of specific design and analysis procedures to ensure safety during operation. However, presence and growth of damage in a structure, whether metallic or composite, reduces the useful strength of the structure which affects safety and reliability at optimum capacity. Therefore, to ensure safety and extend operational life of a component, techniques of damage initiation and growth are needed.

There are a number of nondestructive evaluation (NDE) techniques currently in use. Most of these methods have been developed for periodic inspections of damage growth in structures such as pressure vessels and aircrafts. In the past couple of decades, new techniques of continuously monitoring the integrity of structures, usually termed “Structural Health Monitoring (SHM) techniques” have gained the attention of researchers. Acoustic emissions (AE) based structural health monitoring has been one of the candidate techniques to monitor structural integrity in real time. The implementation of the technique to real field problem, however, has been limited because of its including inability to identify source mechanism, and accurately estimate the magnitude of damage. Some aspects of these issues are addressed in this dissertation.

This research encompasses three topics which are related to the areas outlined above. These are attenuation of acoustic emission signals in composites, signatures of delaminations related acoustic emissions, and acoustic emissions generated due to friction. The materials of interest in this research include both composite materials, specifically carbon fiber reinforced

polymers (CFRP's) and monolithic materials (Aluminum and Steel). In this chapter, overview of nondestructive evaluating mechanisms currently in use, background and objectives of this research and the outline of this manuscript are covered.

1.1 Non-Destructive Evaluation and Structural Health Monitoring

There are several NDE techniques which are currently in use for periodic maintenance and inspection. Table 1.1 shows some of these techniques. The basic mechanism of operation for some of the techniques involves sending energy in some form to the structure and measuring the response under different conditions. For example, infrared thermography sends energy in the form of heat and signals of radiation emitted from the structure are used to detect discontinuity in the structure. In the case of ultrasonic and acoustic detection, mechanical waves which either are introduced by means of transducers or emitted from the structure are used to identify presence of defects. Common behavior among these NDE methods is the periodic or routinely scheduled maintenance reduces the operational availability of the structure.

Table 1.1

NDE test methods

Test Method	Description
Visual inspection	Observation by human eye, also could be assisted by cameras
Dye penetration	Dye liquid seep into structural defects such as cracks, voids
Thermography	Heat applied to the structure and radiation used
Eddy current testing	Fluctuations in the current reading used to detect anomalies
Radiography	Electromagnetic radiation reveal internal defects
Ultrasonic/Acoustic test	Mechanical waves used to detect defects in structures

Condition based maintenance, in contrast to periodic or routine maintenance is ideal to increase availability of the structure to longer periods of service. In condition based maintenance, the structure will be subject to inspection and maintenance based on information about its status of integrity. Successful SHM techniques will be superior to conventional NDE procedures for adopting condition based maintenance procedures. Sensors with real time monitoring capability are used for gathering in-situ real time data.

Structural Health Monitoring (SHM) are analogous to human nervous system. Implementation of SHM involves installing a system in a structure which enables continuous monitoring of the state of integrity of the structure. The objective of an SHM system is providing information regarding damage initiation and propagation in the structure in real time. Damage identification process is commonly divided into five basic steps (Staszewski et al., 2004). These are damage detection, identification of damage location, definition of type or mechanism of damage, quantification of damage size and estimation of life of the structure.

There are active and passive ways of implementing monitoring integrity of structures. The structure, in the case of active mechanisms, is excited by some form of energy from external sources (by means of transducers) and the response of the system is measured at selected spots. In passive approach, on the contrary, release of energy within the structure is detected by transducers. Signals emitted by initiation and growth of damage are monitored through this approach. Acoustic emission technique falls into the category of passive monitoring methods.

1.2 Acoustic Emission Based Structural Health Monitoring

"Acoustic emissions are defined as the class of phenomena whereby transient stress/displacement waves are generated by rapid release of energy from localized sources within a material, or the transient waves so generated" (E1316, 2013). A variety of processes could lead

to generation of such stress waves in solids. Formation of cracks, slip and twinning in crystalline solids and relative movement between surfaces in contact are some of the prominent sources of acoustic emissions. Different damage mechanisms in composites, such as delamination and fiber break result in acoustic emissions.

Acoustic Emission Technique is a method which makes use of these emissions to detect initiation and growth of defects in structures. AE transducers mounted on the structural member can give an indication of damage location and rate of damage growth. Identification of source mechanisms from the received AE waveforms has been an area of considerable research. Some general features of acoustic emission testing are:

- It is a dynamic method providing information about discontinuity growth. Static defects do not give rise to emissions.
- Limited access to monitoring is required. Placing AE transducers in parts of components inaccessible to other methods underlines one advantage of AE based monitoring

As nondestructive evaluation tool, AE have been used to monitor pressure vessels, aerospace structures and bridges (Shull, 2002). Acoustic emission structural health monitoring, however, has largely been limited for proof tests. Some of the major studies in this regard include Acoustic Emission Helicopter health and usage monitoring (AE-HUMS), a device which was used to detect damage in drive trains (Finlayson et al., 2000). A growing crack in a pinion gear was detected prior to its failure. In flight acoustic emission system has also been demonstrated on a Delta clipper technology demonstrator (Finlayson, et al., 2000). These tests indicated acoustic emissions have real place in aerospace SHM. Several challenges such as correlation between obtained data and source mechanisms or establishing baseline data and

interference by noise signals need to be addressed before applying acoustic emission technique (Miller et al., 2005).

1.3 Background of the study

Interpretation of the AE signals depends on several factors. These include the material properties, the geometry and the instrumentation used to detect, condition, and store the signals. A phenomenon common to propagating waves in solid media is attenuation. The intensity of acoustic emission signals decreases as they propagate with in the structure. The inherent effect of these phenomena is that the information contained within the waveforms changes with distance of propagation which is the distance between the AE source and sensor. Acoustic emission sensors placed at different distances provide different signal waveforms which vary primarily because of attenuation even though they originate from the same event. Thus, in acoustic emission analysis, consideration of attenuation behavior of the material and the geometry of wave propagation is crucial for correct interpretation of AE waveforms and estimate the source magnitude. Review of AE literature indicates that not much attention has been paid to the effect of attenuation in analyzing AE signals. The first part of this research focuses on measuring attenuation in composite laminates and evaluating its effect on detected signal amplitudes.

AE has been used to monitor damage in composites. Delamination, the separation of two adjacent plies in composite laminates, represents one of the most critical failure modes. Several researches in the past focused on identifying and quantitatively analyzing the mechanisms of damage during delamination. The delamination behavior including the details of interfacial failure as well as the resulting AE waveforms depends on different parameters such as the location of delamination and the rate of separation between the plies. The second part of this

research deals with analysis of acoustic emissions from delamination in carbon fiber reinforced polymer (CFRP) test specimens

Within a structure, multiple processes that emit acoustic waves take place simultaneously. An example could be generation of waves during fretting fatigue crack in mechanical parts. Rubbing between the contacting surfaces generates waves mainly due to interaction of irregularities on the surfaces. On the other hand, rubbing between the surfaces also leads to formation of cracks on the surfaces, which also give rise to emissions. The sensors mounted to pick signals from crack growth also pick signals from other sources, which are caused by internal or external processes. Thus, in analysis related to those signals from critical processes, the signals from other sources appear as noise signals or "false positives" and could severely affect the interpretation of the obtained data. It is thus necessary to differentiate the signals with respect to their leading sources. This helps to identify the pattern with which processes critical in identifying the remaining life of the material are growing in the material. The third part of this research deals with acoustic emission signals generated due to crack growth and friction between metallic surfaces.

1.4 Specific objectives of the research

Three important problems which form the basis for undertaking this research were discussed in the earlier section. Individual sections related to different aspects of AE based SHM are addressed separately. The general objective of this research is to develop methods for better quantification of AE signals for structural integrity assessment.

The specific objectives are:

Examine how attenuation behavior of CFRP materials affects acoustic emission wave propagation

The attenuation characteristics of crossply and quasi-isotropic CFRP panels with specific layup are studied. Attenuation coefficients for fundamental modes of elastic wave propagation in the composite were obtained for different frequency ranges of laminate directions. These values were applied to numerically simulated AE signal waveforms.

Simulate different damage mechanisms in composite materials experimentally and characterize the acoustic emission behavior in relation to the damage mechanisms

Mode I delamination tests on thin CFRP quasi-isotropic and crossply specimens were done under varying delamination parameters. The different damage mechanisms in composites were observed in these tests. Scanning electron microscope (SEM) images of the fracture surfaces for each test were taken to identify the mechanisms. Acoustic emission signals were obtained during the tests. Features of the acoustic emission data were used to relate the signals with the mechanisms.

Differentiate acoustic emission signals from multiple sources occurring simultaneously in metallic materials

Acoustic emission signals resulting from crack growth in steel bar were obtained. Also, friction between metallic surfaces was obtained using a test fixture developed for this test. The distinguishing features of the signals were identified.

Some of the contributions from this research include:

- Influence of attenuation on wave propagation modes and on acoustic emission events
- Attenuation behavior dependence on laminate type and laminate direction
- Effect of stacking sequence and interfacial properties on acoustic emission events during delamination

- Effect of delamination growth rate on acoustic emission signals during delamination
- Characterize friction related acoustic emission signals in steel
- Differentiating acoustic emission source mechanisms in steel material

1.5 Research Rationale and Benefits

The increasing use of composite materials in several areas has led to extensive research activities in the field of composites. Presence of damage, as mentioned earlier, affects load carrying capacity of structures. Methods which enable detection of dynamic response of a system in response to damage initiation and growth are quite important in overcoming some of these negative tendencies The results obtained from this research are aimed at advancing the implementation of acoustic emission based structural health monitoring in different areas. The target objects considered here are aerospace and civil structures.

1.6 Structure of Dissertation

The present dissertation has been organized on seven main levels with Chapter 1 dedicated to the introduction of the subject matter and the specific objectives for the research work. Chapter 2 presents a thorough literature review on damage mechanisms and progression, acoustic emission and acoustic emission behavior of different failure mechanisms. Findings from previous researchers are also included. Chapter 3 presents the methods, materials and equipment used to successfully carry out the tests in this research work. The results from attenuation measurements on CFRP crossply and quasi-isotropic panels are presented in Chapter 4. Delamination tests performed on beam specimens cut from the panels used in the attenuation tests are presented in Chapter 5. Each of these chapters also discussed numerically simulated AE events. Chapter 6 presents acoustic emission signals from friction and crack growth experiments

in steel material. Methods used to differentiate the signals from these two sources are also discussed. Finally, a comprehensive conclusion and recommendations based on the results are presented in Chapter 7. References and appendices are presented in the final section of this manuscript.

CHAPTER 2

Literature Review

2.1 Fiber Reinforced Polymers Overview

Composites are becoming important components of today's engineering materials because of the advantages they offer. They are broadening the horizon of designers in multiple branches of engineering. The constituents of composite materials are the reinforcing elements and the matrix. The constituent materials combine while retaining their physical properties. The combination of the materials, however, gives new materials that exhibit different mechanical properties as compared to the constituents. The matrix holds the reinforcement to form the desired shape while the reinforcement improves the overall mechanical properties of the matrix. The benefits of combining dissimilar materials to obtain better properties from the constituents have been understood for many years. Using straw to reinforce mud in brickmaking was mentioned in the book of Exodus.

Of the many composite material types, fiber reinforced polymers (FRPs) have been the focus of extensive research and application in advancing materials technology particularly in the aerospace industry since the 1950's. These materials combine fibers which could be made of glass, aramid or boron with matrix material to provide the new material. Epoxy, polyester, and urethane resins are some of the materials used as the matrix constituent. The manufacturing processes used to produce the materials could vary depending on the application desired. The fundamental units of continuous fiber laminate are unidirectional or woven fiber laminae. Laminas are stacked on top of each other at various angles to form a multidirectional laminate.

The composition of the materials for the airframe structure of the Boeing 787 Dreamliner proves the extent of the application of FRPs in the aerospace industry, Figure 2.1. About half of

the material used in the airframe structure consists of composites (CFRPs, glass fiber reinforced polymers (GFRPs) and Carbon Sandwiches). In addition, increasing portions of flight structures, both commercial and military, are being made of FRPs. Construction of composite crew model was completed by NASA in 2009, Figure 2.2. In 1998, 55% to 60% of the carbon fiber production was used in the aerospace industry (Donnet, 1998). In civil engineering applications, CFRPs are being used as reinforcing layers to increase the stiffness of structures. Several research projects are being carried out that show the advantage of having CFRPs as reinforcing or retrofitting components (Ghosh & Karbhari, 2007; Karbhari, 2004)

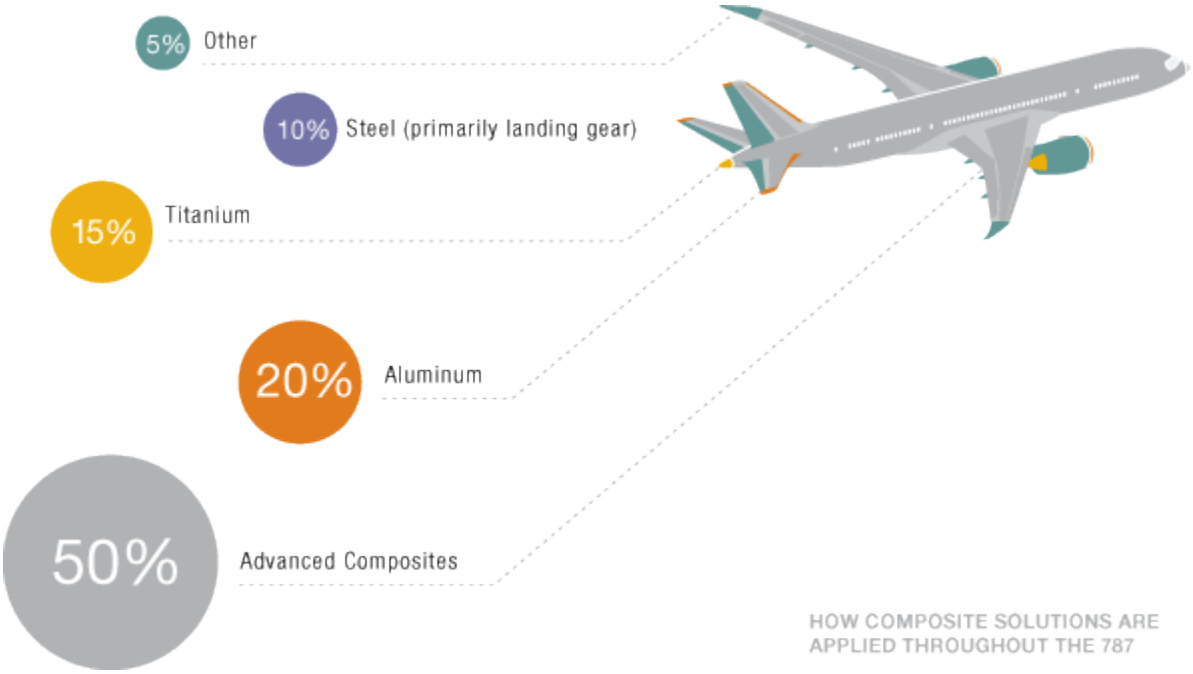

Figure 2.1. Material breakouts on Boeing 787 Dreamliner (http://www.boeing.com).

The driving force behind the progress in the application of FRPs has been improved mechanical properties obtained from the materials, in comparison to traditional structural materials. The advantages of composites include high strength or stiffness to weight ratio and high resistance to fatigue and corrosion degradation. The specific strength and specific modulus of high strength fibers such as carbon are higher than those of traditional aerospace metallic

alloys. Fatigue cracking and corrosion difficulties experienced with traditional aluminum floor beams were minimized by replacing them with beams made of advanced composite materials in Boeing 777 airplanes. The weight savings are significant ranging from 25% to 45% of the weight of conventional metallic designs. This enables one to achieve structures with improved performance.

Figure 2.2. Composite crew module at Alliant Techsystems (http://www.nasa.gov).

Table 2.1 shows some of the mechanical properties of polymer matrix composites and monolithic materials (Kaw, 2010). Other characteristic features of composites include that they are mostly orthotropic and inhomogeneous, are dimensionally stable (they have low thermal conductivity and low coefficient of thermal expansion), and can be tailored to work with a broad range of thermal expansion design requirements and to minimize thermal stresses.

Table 2.1

Typical mechanical properties of polymer matrix composites and monolithic materials

Property	**Graphite/epoxy**	**Glass/Epoxy**	**Steel**	**Aluminum**
Specific gravity	1.6	1.8	7.8	2.6
Young's modulus (GPa)	181	38.6	206.8	68.95
Ultimate tensile strength (MPa)	1500	1062	648.1	275.8
Coeff. of thermal expansion (μm/m/°C)	0.02	8.6	11.7	23

Despite their improved mechanical properties, composites have shortcomings which include high raw-material and fabrication costs and poor out-of-plane properties. The other major issue with FRP composites is susceptibility to impact induced damages. Impact by foreign materials introduces fracture of the matrix material and interlaminar delaminations.

Apart from impact, the presence of inherent defects that could be introduced at several stages in the life of composites could lead to severe consequences. During the pre-manufacturing phase, the resin material and the fiber could contain moisture and other inclusions. Fiber damage could also be present and later affects the total strength. Inclusion of voids, gaps, porosity, wrinkled or wavy fibers, and foreign materials are some of the major defects that can be introduced during manufacturing. During transportation and installation, abrasions indentations, and damaged edges could be introduced. The consequence of these defects in the composite material could be severe. The spots containing the defects create fields of higher stress and strain from which damage can initiate and propagate during fatigue or overloading conditions. The mechanism of damage initiation and propagation could vary depending on the loading conditions and the construction of composite layup. There are different modes in which damage can propagate in composite structures. The description of each is provided in the following section.

2.2 Damage/Failure Mechanisms in Composites

The failure behavior of composites is complex and can be influenced by the composition of the matrix and fiber, the material for the fiber and the matrix, the fiber orientation, the stacking sequence and the angle and the type of load. Common mechanisms of damage initiation and propagation in composites include fiber breaking, matrix cracking, fiber-matrix debonding and delamination.(Milne et al., 2003; Scheirs, 2000) described the different failure modes using a single unidirectional lamina. A unidirectional lamina subjected to axial tension load in the direction of the fibers has a behavior governed by the fibers. The failure modes that could occur for such a case are fiber breaking, shown in Figure 2.3, and failure of the matrix-fiber interface.

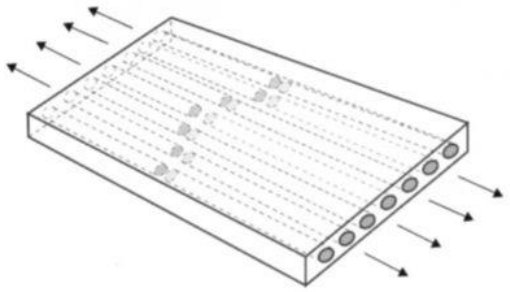

Figure 2.3. Fiber breaking (Milne, et al., 2003).

On the other hand, if the loading direction is turned perpendicular to the orientation of the fibers, the response will largely be determined by the matrix material. Hence, the applied transverse loads create higher strain in the resin material and this can cause formation of cracks in the matrix, see Figure 2.4.

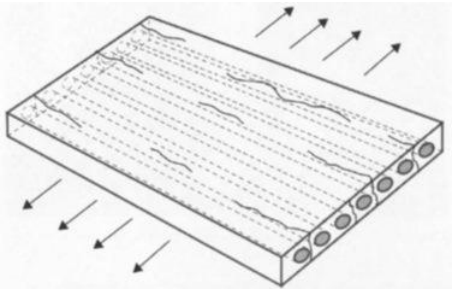

Figure 2.4. Matrix cracking (Milne, et al., 2003).

Delamination refers to the separation between adjacent plies of a composite laminate. It has been classified as the most common and the most dangerous failure mechanism in composite laminates (Martin et al., 1995; Milne, et al., 2003; Sridharan, 2008). It reduces the load carrying capacity of the laminates significantly. The phenomenon of delamination is explained by a model consisting of two laminae with fiber orientation orthogonal to each other. When the laminate is subjected to an axial load along any one of the fiber directions, the magnitude of the contraction or expansion experienced by the laminae is different. This creates a shear stress at the interface which tends to split the laminae apart causing delamination. Delaminations initiate from spots which are weak to resist the shear force such as edges, holes, and flaws. Impact loads are also significant sources of delaminations. A schematic of separation between layers is shown in Figure 2.5.

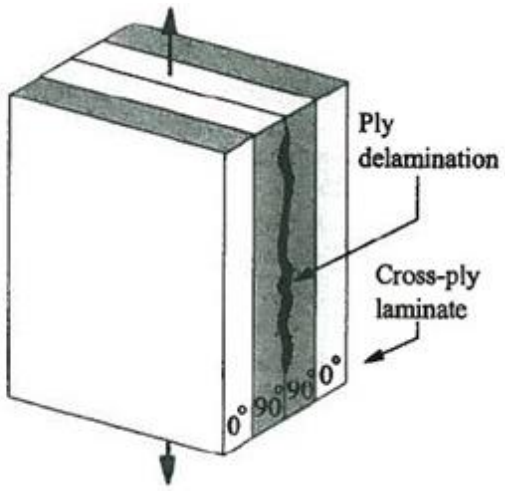

Figure 2.5. Delamination in crossply laminate (Reifsnider & Case, 2002).

2.3 Damage Progression in Composites

(Reifsnider & Case, 2002) describes a material degradation process as shown in Figure 2.6. The degradation process, in addition to being facilitated by mechanical loading, is facilitated by chemical and thermodynamic processes within the service environment. The ultimate effect

of these processes is a reduction in the useful strength of the component. Durability and damage tolerance analyses that deal with how long the engineering component lasts, how safe the engineering component is after some period of service and how reliable the engineering component is depend on the useful strength of the component.

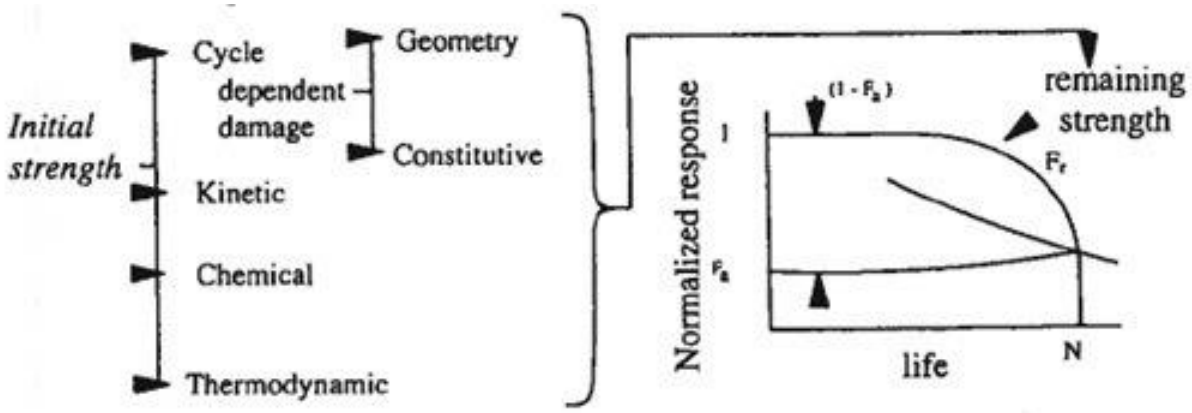

Figure 2.6. Degradation process in a material (Reifsnider & Case, 2002).

Damage progression in composites proceeds with the accumulation of microdamages, which occur in different modes. Failure does not always happen by the growth of single mico crack. The progression of damage is characterized by distribution of mechanisms over the dimensions of the laminates instead of being concentrated over smaller zones (Harris, 2003). The microstructural mechanisms of damage accumulation, discussed in the previous section, occur sometimes independently and sometimes interactively, and the relative presence of each may be affected by both materials variables and testing conditions. The accumulation and subsequent interaction of these microdamages is accompanied by the evolution of material states and stress states. Damage progression is characterized by a statistical nature of occurrence.

Damage accumulation may not always immediately reduce the strength of the composite. However, at even lower stress levels, it reduces the stiffness. At low quasi-static load levels, or in the early life of a composite subjected to fatigue loading, damage spreads throughout the stressed

region. However, most composite systems sustain damage this stage. At a later stage, the accumulated damage in some region could be so great that the residual load-bearing capacity of the composite falls to the level of the maximum stress in the fatigue cycle, Figure 2.7. This does not necessarily relate to the propagation of a single crack, unlike the case with monolithic materials.

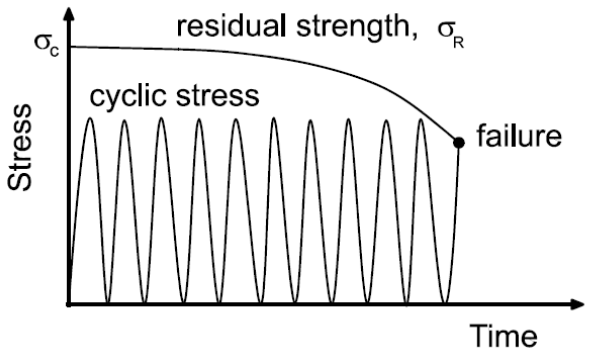

Figure 2.7. Degradation of composite strength (Harris, 2003).

Damage accumulation in composites begins with matrix microcracking in off-axis plies. The immediate effect of microcracks is degradation in the properties of the laminate including changes in stiffness (Figure 2.8), Poisson ratios, and thermal expansion coeffcients. They present the most pervasive type of damage modes in composites.

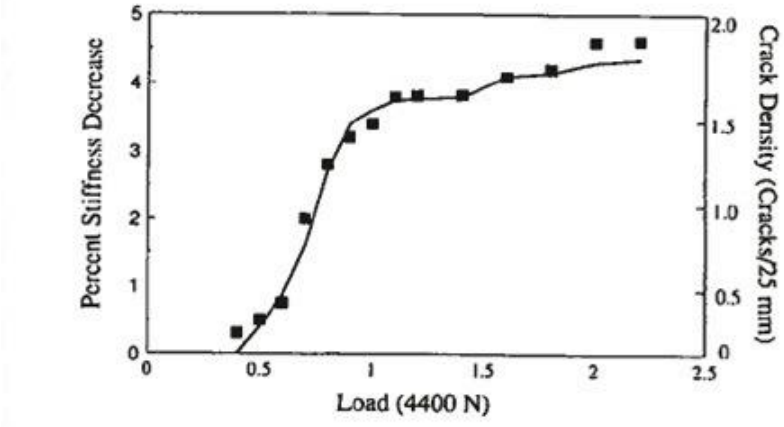

Figure 2.8. Change in stiffness with matrix cracking (Reifsnider & Case, 2002).

The effect on the strength of the composite system is such that the strength is hardly affected by matrix cracking. These modes are densely populated modes which, with an eventual increase of load, get to state of saturation. This state is termed the characteristic damage state. Figure 2.9 shows the reduction in stiffness during fatigue loading of two quasi-isotropic laminates.

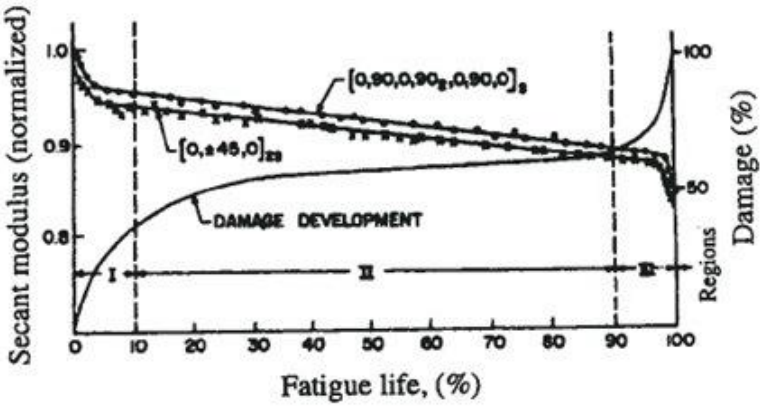

Figure 2.9. Change in stiffness with matrix crack and delamination (Reifsnider & Case, 2002).

The first part of reduction in the stiffness was caused by matrix cracking. During stage II, matrix cracking assumes a characteristic damage state; however, further reduction in stiffness goes on due to nucleation and growth of interlaminar delamination. In fact, matrix cracking zones are considered spots for nucleation of delaminations in the plies, see Figure 2.10.

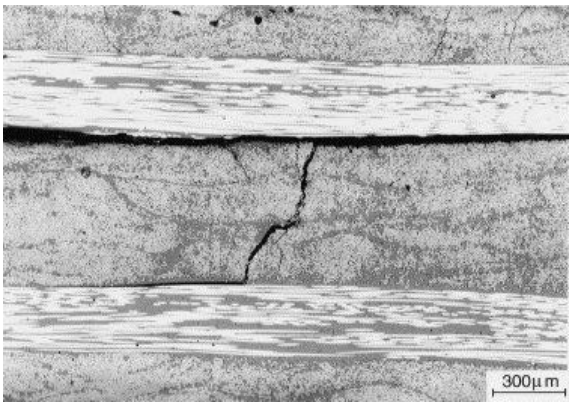

Figure 2.10. Matrix cracking and delamination (Diao et al., 1997).

Adjacent plies of different fiber orientation experience different deformation and due to this difference, energy is stored that separates one ply from the other. Delaminations often start and spread from the edge of laminates. When delamination occurs, the adjacent plies experience different level of deformation and this leads to reduction in stiffness. In some cases, the reduction in stiffness caused by delaminations is larger than that caused by matrix cracking. The decrease in stiffness could be so large that areas that are least affected by delamination growth are forced to carry higher loads. This leads to a reduction in the strength or load carrying capability of the laminates. In many cases, zones of delamination in laminates are characterized by a higher number of fiber fractures and fiber-matrix interface failures.

The design of most composite laminates is such that they depend primarily on the fibers for their stiffness and strength or they are fiber controlled. Therefore, fiber failure significantly affects the strength and stiffness behavior of the composite laminates. Within a composite system, an individual fiber can break many times. The reduction in stiffness and strength due to fiber failure is somehow complex to quantify.

Collective interaction of the individual modes governs the long term response of the composite system. The interactions of the modes, as outlined earlier, are statistical and complex in nature. Matrix cracks are mentioned as causes of fiber fracture and serve as spots for nucleation of delamination. Delamination zones have significant local stress distribution which causes fiber overload and fracture. Depending on the matrix composition, fiber fractures cause fracture of neighboring fibers. During delamination, fiber fracture could also be present due to fiber bridging. This complex interaction characterizes typical damage progression in composites.

2.4 Acoustic Emissions and Wave Propagation

The distinct features of acoustic emissions are that the energy that is detected by the transducers is generated within the material and that the method is sensitive to dynamic processes such as growing discontinuity. The stress level in a structure, under normal operating conditions, could be well below the design limit. However, the presence of structural discontinuity causes zones of higher strain to develop under these same loading conditions. The higher strain zones undergo deformation accompanied by the release of energy. Hence, propagating waves are generated from the deformation and the energy released due to the growing discontinuity. Thus, the growing discontinuity becomes an active acoustic emission source. The propagation of the displacement generated waves is nondirectional resulting in spherical wavefront. As the leading events, in most cases, have a duration in the order of microseconds, the generated displacements are pulse type. These generated pulse type signals, however, change significantly as they propagate in the material. These waves are detected by the sensors and one of the focus areas in acoustic emission technique is to develop the relation between these signals and the source event. The wave propagation behavior, thus, becomes important factor in acoustic emission analysis. Ultrasonic testing, as discussed earlier, is also a method based on the propagation of waves in solid materials.

The physics of wave propagation in solids has been studied in the past. (Giurgiutiu, 2007; Rose, 2004; Shull, 2002) present the current state of our understanding of the phenomenon. A system of solid material perturbed from its equilibrium position experiences waves propagation. The basic types of wave propagation modes for the disturbance are dilatational (longitudinal) and distortional (transverse) modes. However, these are definitions applicable to bulk media. The interaction of the propagating waves with the material boundaries, however, results in different

modes. Depending on the direction of wave propagation and particle motion the waves can be classified into the following types and the schematic representation of each is provided in Figure 2.11.

1. Longitudinal waves
2. Transverse waves
3. Rayleigh waves
4. Love waves

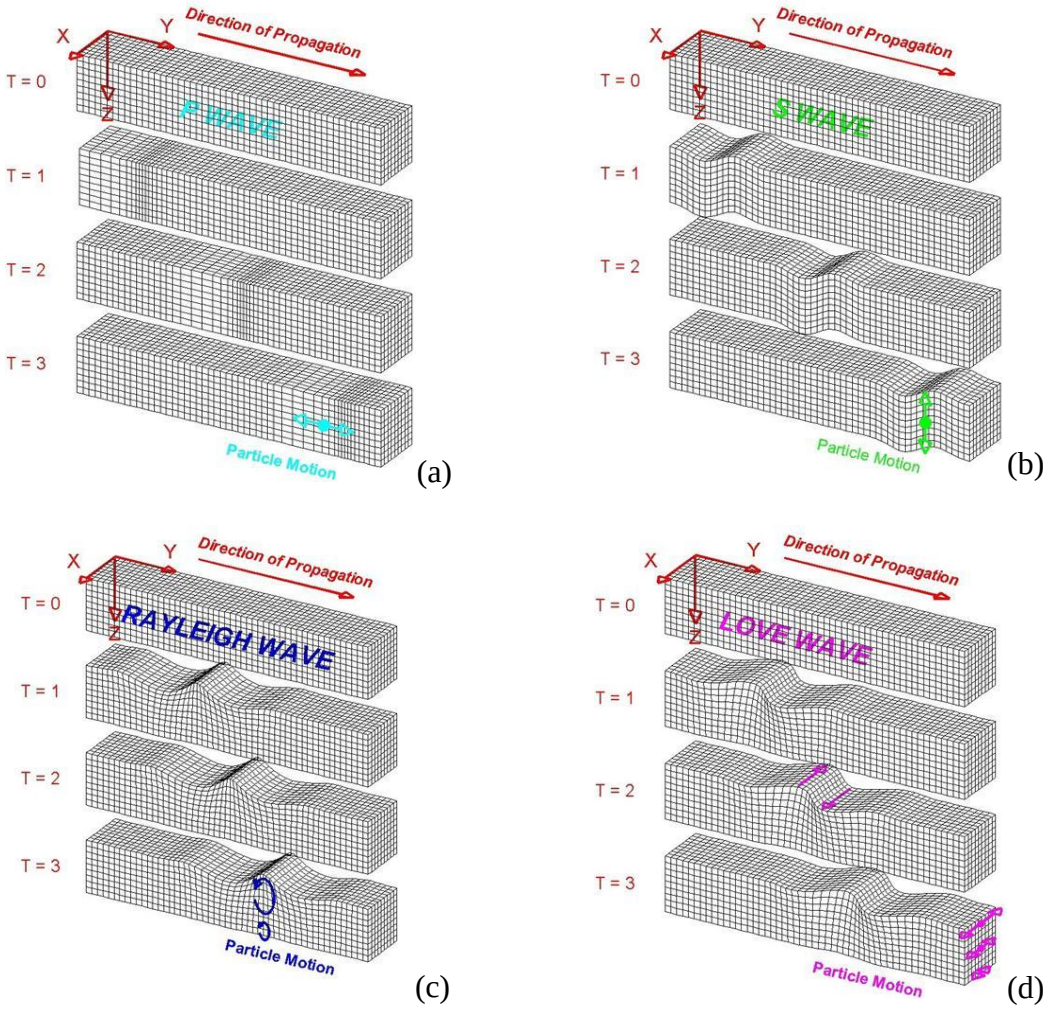

Figure 2.11. Particle displacement and wave propagation in different types of waves (http://web.ics.purdue.edu).

The particle displacement is along the direction of wave propagation for longitudinal waves (Figure 2.11a). The particle displacement is perpendicular to the direction of the waves in the case of transverse or shear waves (Figure 2.11b). A Rayleigh (or surface) wave has an elliptic particle motion in planes normal to the surface and parallel to the direction of the wave propagation (Figure 2.11c). A Love wave is the wave in a layered medium where particle motion is parallel to the plane layer and perpendicular to the wave propagation direction, Figure 2.11 d. Additional categories are also available in (Shull, 2002).

A special case of wavemodes commonly observed in plate type materials are Lamb waves. Longitudinal and transverse waves, in principle, exist in bulk media. In structures of finite dimension mode conversion takes place and the waves attain a different pattern of propagation. Initially, the waves from a source in the material or from an external source start to propagate as longitudinal and transverse waves. An incident wave on a boundary produces longitudinal and transverse components, shown in Figure 2.12 and a series of such interactions within a reasonable distance produces constructive interferences that lead to different pattern of wave propagation, which are termed Lamb waves.

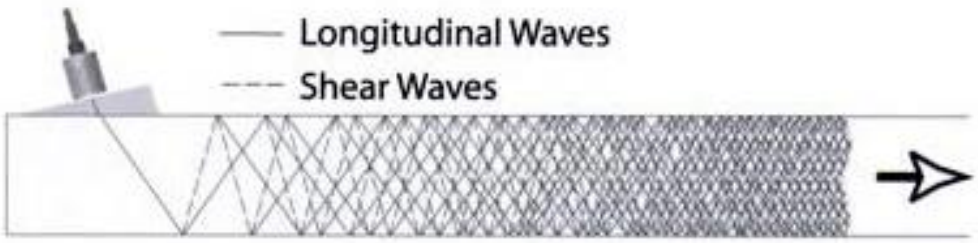

Figure 2.12. Generation of lamb waves (Shull, 2002).

The resulting constructive interference can produce a displacement pattern of particles such that the resulting displacements could be symmetric or antisymmetric about the mid plane or the plane of symmetry of the plate. The symmetric (S) and antisymmetric (A) modes are

shown in Figure 2.13. The speeds with which symmetric and antisymmetric modes travel or propagate vary depending on the material stiffness and density. The acoustic emission waves generated within a plate material propagate in either of the two modes or their combinations. The symmetric and antisymmetric modes have fundamental and higher order versions that vary in the displacement pattern.

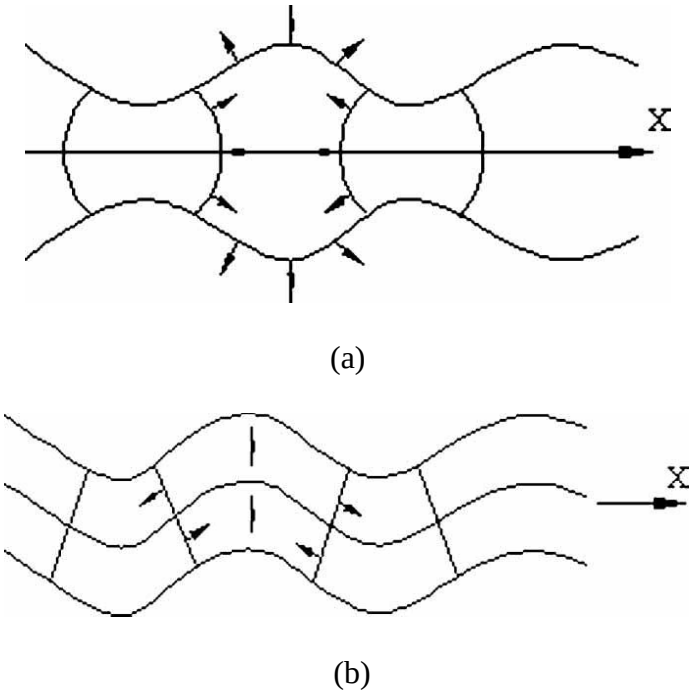

Figure 2.13. Symmetric (a) and antisymmetric (b) modes (Wandowski et al., 2011).

Practical considerations in solid wave propagation include phase and group velocity, attenuation, dispersion, scattering and reflections. The concept of phase and group velocity is explained with the aid of Figure 2.14. Group velocity refers to the velocity of a group of waves that have same frequency. In the figure, the group velocity is depicted as the rate at which an envelope enclosing the group of waves advances (see the points referred to as G1, G2 and G3). Phase velocity, on the other hand, represents the velocity with which a phase of wave propagation advances (see the points referred to as P1, P2 and P3). Attenuation refers to the reduction in intensity or amplitude of the waves as they propagate in the structure. (Details are

presented in section 2.8) The waves propagating in a structure could consist of components of similar frequency but tending to advance at varying speeds. This, with increased distance of propagation leads to a separation of the components. This phenomenon is referred to as dispersion.

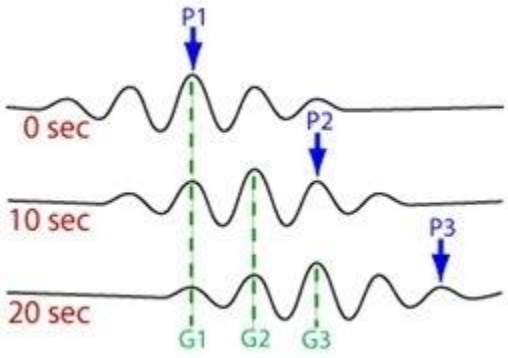

Figure 2.14. Phase vs. group velocity (www.muravin.com).

In wave propagation studies, dispersion curves like the one shown in Figure 2.15 are used. The curves depict the velocity of different modes, including higher order modes such as A_1 and S_1, with respect to the frequency and thickness of the material. Interaction of propagating waves with discontinuities in material geometries results in scattering and diffraction of waves. The curves are generated by solving Rayleigh-Lamb frequency equations (Rose, 2004) given as equations (2.1) and (2.2).

$$\frac{\tan(qh)}{\tan(ph)} = -\frac{4k^2pq}{(q^2-k^2)^2} \qquad \text{for symmetric modes} \qquad (2.1)$$

$$\frac{\tan(qh)}{\tan(ph)} = -\frac{(q^2-k^2)^2}{4k^2pq} \qquad \text{for antisymmetric modes} \qquad (2.2)$$

p and q are given by

$$p^2 = (\frac{\omega}{C_L})^2 - k^2 \quad \text{and} \quad q^2 = \left(\frac{\omega}{C_T}\right)^2 - k^2 \qquad (2.3)$$

In the equations, ω and k represent the circular frequency and wavenumber respectively. The wavenumber k is equal to ω/C_p, where C_p is the phase velocity of the Lamb wave mode. The phase velocity is related to the wavelength, λ, by the equation $C_p = (\omega/2\pi)\lambda$. C_L and C_T designate the longitudinal and transverse wave velocities in the material respectively. The equations were derived for a plate with thickness $2h$.

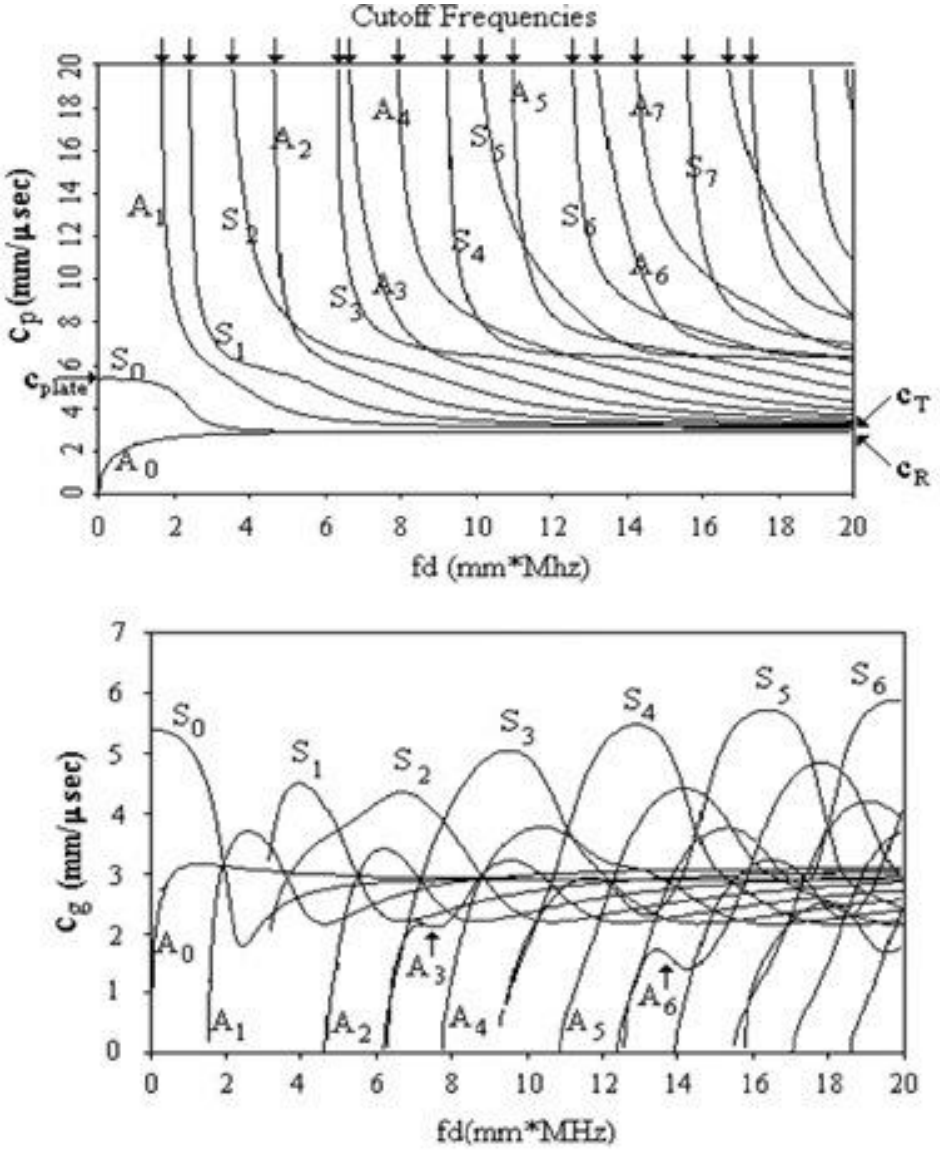

Figure 2.15. Aluminum dispersion curve (Rose, 2004).

All the aforementioned phenomena affect the wave propagation characteristics of acoustic emissions generated by the different mechanisms. The measurement of the generated waves of signal waveforms is accomplished by bonding or attaching transducers on the surface of a structure being investigated. Surface displacements caused by the propagating waves are picked up by the transducers.

2.5 AE Signal Characteristics

An acoustic emission waveform is displayed on voltage vs. time plot. Figure 2.16 shows a typical AE waveform. The waveforms are defined by parameters that later are used for further analysis. Descriptions for some of the features (parameters) of the waveforms are provided.

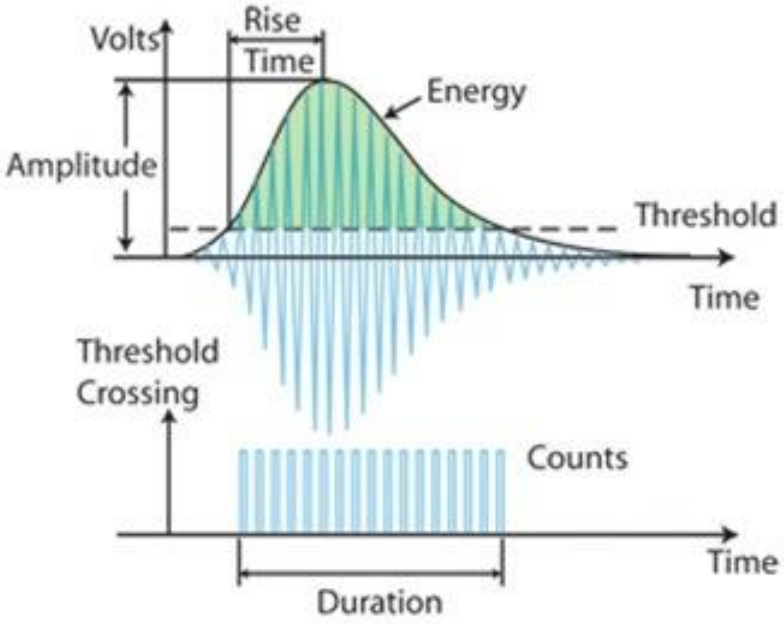

Figure 2.16. AE waveform.

(http://www.mistrasgroup.com/products/technologies/acousticemission.aspx)

Hit – individual signal burst produced by local material change

Peak amplitude (amplitude) – the maximum signal excursion (positive or negative) during a hit

Threshold – A voltage level set during data acquisition such that only events exceeding this level will be recognized. The threshold detection level is set above the background noise level.

Time of hit – the time at which the signal exceeds the threshold

Counts – counts of the waveform signal excursions over the threshold or number of times the signal exceeds the threshold

Duration –the time between the start of an AE event and end of the same event, calculated as the difference between the time of first threshold crossing and the time of the last threshold crossing

Rise time – the interval between the time of first threshold crossing and the time at which the peak amplitude of the signal is recorded

Average frequency – the ratio of the counts to the duration

Peak frequency – the maximum frequency reading in the power spectrum of the signal

Energy – integral of the rectified voltage over the duration of the acoustic emission hit or the area below the curve enclosing the waveform

An AE signal waveform and its features are affected by the source type, geometry of the specimen, transducer characteristics, and measuring/acquisition system used. In some researches pertaining to acoustic emission source characterization in materials, distribution and cumulative plots of the above features are used. The other kind of analysis makes use of pattern recognition methods on a group of features.

2.6 AE in Composites

Any sudden structural change within a composite, such as matrix cracking, fiber fracture, debonding, or interlaminar cracking, causes dissipation of energy as acoustic emissions. There

are several ways to analyze the information obtained by AE monitoring of structures under load, some of which offer suitable quantitative procedures for proof testing or life prediction, and some of which provide deeper insight into the mechanisms of damage accumulation in composites. Acoustic emission data obtained from failure process under different kinds of tests can be analyzed to differentiate the mechanisms involved. Several researchers used this advantage to investigate the different mechanisms of failure using acoustic emission data. (Ni & Iwamoto, 2002; Ramirez-Jimenez et al., 2004) used frequency features of an AE data set that they obtained experimentally. (Bussiba et al., 2008) studied damage accumulation profile up to fracture in quasi-statically loaded composite specimens using counts rate. Wavelet transforms were used in addition to obtain frequency and time information about the different failure mechanisms. (Loutas & Kostopoulos, 2009) used features such as amplitude, number of AE events, cumulative AE energy and peak frequency for clustering AE data obtained from tensile tests and correlated the clusters with the different failure mechanisms. (Haselbach & Lauke, 2003) was able to characterize acoustic emission signals accompanying debonding between fiber and matrix material using the amplitude and frequency of the signals. In the following section, past work regarding failure mechanism identification during delamination by means of acoustic emission data is presented.

2.7 Delaminations and AE

Delamination is an important mechanism that leads to a reduction of the strength of fiber reinforced polymers. Delamination growth involves a large number of microscopic damage events such as matrix cracking and fiber break. The macroscopic growth of interlaminar fracture can easily be identified. However, the microscopic behavior of the damage processes is more difficult to observe. Acoustic emission methods have been proved to have the potential for

detecting and characterizing delamination initiation and propagation. High intensity AE signals can be obtained from the different damage mechanisms that occur during interlaminar fracture (Sridharan, 2008). (Cesari et al., 2007; Huguet et al., 2002) showed that AE is an appropriate tool for monitoring delamination. However, the interpretation of AE signals and, thus the evaluation of the state of damage are major challenges in AE analysis.

Much of the research reviewed here makes use of the (D5528, 2007) standard which is practically used to study or determine the fracture toughness of composite materials under mode I loading conditions for unidirectional layup of fibers. The standard recommends use of a double cantilever beam, as in Figure 2.17, which is fitted with insert film at the mid plane interface so as to initiate delamination. Hinges are bonded at the ends on the insert side. Quasistatic or fatigue type transverse loads are applied at the hinges. The displacement rates for the quasistatic load ranges from 0.5 mm/min to 5 mm/min. During the test, the axial load on the hinges, the crack opening displacement and delamination growth are recorded and these values eventually are used in the calculation of the fracture toughness.

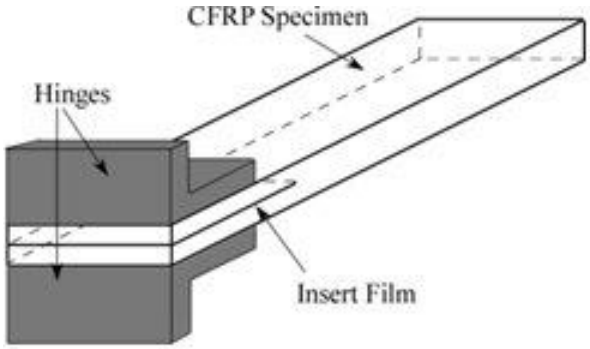

Figure 2.17. Double Cantilever Beam (DCB) test specimen.

The above procedures are adapted to study of acoustic emissions related to mode I delaminations. Transducers are attached on the surface of the specimen and the acoustic emission

events released during the growth of delamination are recorded. Below are presented some of the literature that dealt with acoustic emissions associated with delaminations.

(Arumugam et al., 2011) used the AE energy and peak frequency features of experimentally obtained acoustic emission events to classify them with respect to the corresponding failure mechanisms. The mechanisms investigated were matrix cracking, fiber pullout, fiber breaking, and delamination. The tests were done on DCB specimens cut from unidirectional GFRP 6 ply panels. The crosshead velocity was maintained at 1mm/min. the test has shown that at earlier stages events obtained had lower energy, which could be attributed to matrix cracking. Increasing the AE energy of events with the growth of delamination was associated with occurrence of other failure modes. The peak frequency was also used to classify the events. In the analysis, events with different frequency ranges were classified as caused by matrix cracking, fiber pullout, failure of fiber-matrix interface and fiber failure.

(Oskouei et al., 2011) used the mechanical strain and acoustic energy to define a sentry function by means of which they were able to determine the fracture toughness for glass fiber composites. Three sets of specimens with different layup were used. These were woven-woven, woven-unidirectional, and unidirectional. The sentry function was defined as the logarithm of the ratio of the strain energy to the acoustic energy. Similar to earlier researchers, they tested five DCB specimens loaded at a crosshead speed of 5 mm/min. The strain energy was calculated using the axial load and the crack front displacement (delamination growth). The cumulative acoustic energy was calculated by taking the summation of the energy of the individual events with crack distance. Thus, at a specific crack front displacement, the sentry function can be calculated by taking specific values for the strain energy and cumulative acoustic energy. A Plot of mode I fracture toughness, G_I, with the sentry function provides a curve consisting of two

straight lines connecting at a point forming “knee”. The corresponding reading of the G_I to the “knee” point represented the actual fracture toughness of the specimen.

The fracture toughness results that were obtained were compared to values obtained by other means. It was found that the suggested method using sentry function provided results that were in good agreement with 5% method of fracture toughness calculations provided by ASTM standards. In a similar work, (Davijani et al., 2011) investigated the initiation of delamination and propagation by means of a sentry function. SEM images were used to verify the results from the sentry function. (Fotouhi et al., 2011) simulated delaminations that occur during the drilling of glass epoxy laminates. Rectangular plates with a blind hole were loaded in three-point bending such that the hole was pushed by a thrust force at speeds of 0.2 mm/min and 2 mm/min. The bottom of the hole was provided with thin insert film so as to initiate delamination during loading. Two resonant type PICO resonant sensors recorded the acoustic emission events generated during the tests. The sensors were mounted on the side of the plate from which the thrust force was applied. The sentry function, AE energy and counts of the events were analyzed in association with the growth of delamination. SEM images were taken to observe the damage mechanisms.

(Ndiaye et al., 2000) used acoustic emission signals during delamination tests on unidirectional CFRPs under three different conditions. The three conditions are original specimen at room temperature, a specimen that was delaminated all along its length but rebonded with resin, and a third specimen heated above the glass transition temperature and cooled down to room temperature. Double cantilever beams were considered for the three cases and were loaded at an opening displacement rate of 0.9 mm/min. Cumulative energy plots for the samples indicate that the sample heated above the transition temperature has more resin damage (matrix

crack). The amplitude histograms for the three cases also indicate matrix cracking and fiber breaking in the original sample while matrix cracking occurred predominantly in the sample in which the delaminated specimens were put together by resin.

(Sause et al., 2012) used pattern recognition techniques to distinguish the different failure mechanisms occurring during interlaminar separation. Five DCB CFRP and GFRP specimens were tested with opening an displacement rate of 10 mm/min and the acoustic emission signals generated in the process were recorded by WD type sensors. Three failure mechanisms, which include fiber breakage, matrix cracking and interfacial failures (fiber-matrix debonding, fiber pullout) were studied. Features including average frequency, initiation frequency, peak frequency, and the frequency centroid of the AE signals were used in pattern recognition in order to group the events into three clusters, which correspond to the above three failure mechanisms. Wavelet transforms of waveforms from finite element simulation were also compared with those of selected waveforms from the test.

(Kostopoulos et al., 2007) studied the influence introducing dopants (carbon nano fibers and PZT particles) on the epoxy material for CFRP materials. The damage mechanisms associated with each of the samples were studied by means of acoustic emission techniques. CFRP double cantilever beam specimens were tested with an opening displacement rate of 2 mm/min and the acoustic emission events were recorded by means of a NANO 30 resonant sensor. The collected AE events were clustered into different groups by means of NOESIS software. Four classes of events were obtained. The description of the classified events was provided on the basis of AE energy, number of hits and time. The first class of events were observed to come in very large numbers and were attributed to matrix cracking. The second class of events consisted of higher energy and were more active after some initial period. This group

of events was considered to be caused by fiber break. The third group of events occurred in numbers as high as the second group of events and were thought to be caused by debonding at the fiber/matrix interface. The last group of events were shown to be least connected to any leading event and were determined to be noise signals.

In summary, tests that were mostly based on the double cantilevered beam (DCB) tests were presented. The objective in most cases has been to identify different failure modes in composites. Different sets of specimens, glass fiber and carbon fiber based are investigated. The major failure modes considered in the investigations are matrix cracking, fiber breaking, and interfacial debonding. Different sets of sensors were used for recording data, and the features of the acoustic emission events used for analysis vary. Amplitudes, numbers of hits, counts, and frequency based features were some of them. In most studies, however, the energy of the acoustic emission signals was the feature used for analysis.

2.8 Attenuation Studies

Interpretation of the information contained in acoustic emission signals needs to consider several factors. The features or characteristics of the generated waves vary depending on the source type, material type and geometry of the solid structure, and the instrumentation used to record the signals. As mentioned in Section 2.4, a phenomenon common to propagating waves in solid media is attenuation. Attenuation behavior of materials causes reduction in amplitude of signals as they propagate with in the structure. There are several mechanisms that lead to amplitude reduction as Lamb waves propagate in structures. Some of these mechanisms are associated with energy loss while others cause redistribution of energy.

Geometric spreading involves spreading of the acoustic energy carried by the waves along the geometry of the structure. For Lamb waves propagating in plates, particularly, in

planar isotropic materials, the wavefronts tend to spread in circumferential path. From conservation of energy, the reduction in amplitude due to geometric spreading can be given by the equation:

$$A = A_o * \sqrt{\frac{1}{r}} \tag{2.4}$$

A_o is the amplitude at the source of the signal, and r and A are the distance and the amplitude at the point of measurement. This equation is valid for both symmetric and antisymmetric modes. The second factor in attenuation is material damping (intrinsic attenuation), which causes conversion of acoustic energy or the energy carried by the elastic waves to some other forms of energy in the material. The waves propagate in successive alternate cycles of exchange between kinetic and potential energies. This exchange is accompanied by losses into other forms of energy. The other factors in attenuation are scattering and dispersion. A propagating wave in a material is scattered up on encountering a discontinuity in material composition or the presence of voids and flaws. This contributes to reduction in intensity of the signals. An acoustic emission signal may contain waveforms or modes of different frequency component that tend to move at varying speeds and subsequently separate out as they traverse along the structure (dispersion) and this causes the amplitude of the signal to decrease.

The acoustic emissions generated due to some leading event consist of different wave modes that propagate at different central frequencies. Each of the constituent modes experiences attenuation as it traverses along the material. The inherent effect of these phenomena is that the information contained within the waveforms changes with the distance of propagation or source-to-sensor distance. Acoustic emission sensors placed at different distances provide different signal waveforms which vary primarily because of attenuation even though they originate from

the same event. Thus, in acoustic emission analysis, consideration of the attenuation behavior of the material and the geometry of wave propagation becomes relevant to validate the interpretation of the waveforms.

There has been some work in the past regarding the measurement of attenuation in aluminum and composite structures. (Ramadas et al., 2011) modeled the attenuation of lamb waves using Rayleigh Damping. This model decouples the mass and stiffness portions of damping behavior of materials. The study involved numerical simulations and experiments on GFRP crossply panels. (Pandya et al., 2012) experimentally studied the reduction in peak values of strain waveforms (attenuation) in composites during a ballistic impact. (Drinkwater et al., 2003) studied the effect of compressively loaded elastomer on wave propagation of A_o and S_o modes. It was demonstrated that attenuation of the guided waves increased due to leakage of energy.

(Schubert & Herrmann, 2011) studied the influence of viscoelastic material properties on the measurement of lamb waves. A theoretical model that takes into account dispersive propagation and the effect of sensor size on wave excitation and measurement was considered. MATLAB code was created to implement the model. A test was conducted on a unidirectional CFRP in which the plate was excited by Hann-windowed sinusoidal bursts. The measurements for the responses of the plate were measured at angles of 0, 45 and 90 degrees for input excitations of frequencies between 15 and 400 kHz at steps of 15 kHz. The normalized amplitudes and attenuation coefficients predicted by the numerical model and those obtained from experiment were found to be in good agreement. The normalized amplitudes and the attenuation coefficients were obtained for both symmetric and antisymmetric modes.

(Wandowski, et al., 2011) conducted attenuation measurements on a composite specimen as part of a study on guided wave based detection of damage in composite laminates. The specimen was excited with PZT transducers with a Hanning window of five complete cycles at several frequencies ranging from 100 to 150 kHz, with increments of 10 kHz. It was found that the attenuation increases with increasing frequency.

(Kerber et al., 2010) used a Chirplet transform in attenuation analysis of symmetric and antisymmetric lamb wave modes. Numerically simulated lamb wave signals were used for the analysis. Amplitude ratios and attenuation coefficients due to geometric attenuation were calculated using the CT (Chirplet transform) algorithm and in the regions of the model, where A_o and S_o modes were clearly separated, the results obtained were quiet comparable to those expected from theoretical predictions. However, the method showed considerably less accuracy when the method was applied to experimental data due to noise.

(Biwa et al., 2003) studied a theoretical model for attenuation of wave modes in viscoelastic composite materials. The model takes into account scattering and absorption (viscoelastic) losses. The attenuation coefficient was defined in terms of scattering, absorption loss in the matrix, and absorption in the reinforcing element for a single inclusion. As an example, attenuation coefficients of longitudinal and transverse waves were computed for unidirectional CFRP specimens. The results showed that the attenuation coefficients show high dependence on frequency and that the matrix material is the major element affecting the results.

(Sun et al., 2009) studied the effects of attenuation due to the presence of viscoelastic material by modeling an isotropic plate with varying viscoelastic properties. They discovered that the viscoelasticity had no effect on the velocity of the lamb wave but decreased the

amplitude of the waveform. More specifically, they discovered that the higher frequency components of the A_o mode showed more attenuation than the lower frequency components.

In summary, the literature reviewed here focused on

- Theoretical models to quantify the reduction in amplitude
- FE models to model propagation of lamb waves
- Experimental work to validate the findings in the theoretical and numerical approaches

2.9 AE from friction in Materials

In the previous sections, it was discussed that AE signals are generated during several processes in composites. Incremental crack growth in monolithic materials is also source of these emissions. Processes that involve relative motion in bearings, gears, and turbine blade root joints as well as bolted and riveted joints also give rise to acoustic emissions. The contacting surfaces in these parts, while smooth on a macroscopic scale, have roughness or asperities whose dimensions may be of the order of microns. During the relative motion between two surfaces in contact, the asperities on one surface attempt to slide past the asperities on the opposite surface, which results in the collision between these asperities and the sudden loading and unloading of regions in their immediate vicinity. The interactions between pairs of asperities may last a very short duration, of the order of few microseconds. The transient forces accompanying such interactions between asperities are a prolific source of elastic waves that are sensed as acoustic emission signals. Further, such relative displacement between surfaces can also lead to plastic deformation and fracture of asperities and the accumulation of wear particles between surfaces, all of which can also generate acoustic emission signals. (V.M. Baranov et al., 2011) summarizes the sources of AE during friction conventionally into three groups: impact of the friction surface

at the microscopic level (asperity collision), surface damage and formation and rupture of adhesion junctions.

Repetitive relative motion of the surfaces over longer periods leads to change in the roughness and texture of the surface, and it can be expected that acoustic emission signals may be indicative of these changes. The first group of papers reviewed here examines the relationship between the acoustic emission signal characteristics and the conditions prevailing at the contacting surfaces. (Dornfeld & Handy, 1987) performed early studies to understand the relationship between the AE signals and sliding friction. (Jibiki et al., 2001) studied AE signals generated by friction over a small contact area between two cylinders arranged such that their axes were 90 degree apart. The friction noise for repetitive cycles of sliding at "point" contact of the cylinders was recorded using a microphone. The main frequency component of the detected acoustical signal was a little over 1 kHz. The amplitude of the AE signal was found to increase as the fretting stroke or the frequency was increased. Further, the amplitude of the AE signal was also found to increase with the level of surface wear. (Ferrer et al., 2010) studied the acoustic emission waves generated during transition from static to dynamic friction. Resonant frequency AE sensors were used in these experiments to record the signals. They experimentally simulated stick-slip conditions between a pair of pads and a flat plate during a single stroke and recorded the resulting acoustic emission signals. The different segments of the recorded waveforms were related to different segments of the slip process including micro-slip, partial slip and gross slip. (Ben Abdelounis et al., 2010) examined the noise generated by friction between two flat surfaces using microphones. As the surface roughness was increased, the amplitude of the acoustical signal was found to increase as a logarithmic function of the surface roughness. The relationship between AE signal characteristics and friction and wear was also studied by

(Hase et al., 2008; Hisakado & Warashina, 1998). Parameters of the signals, such as count, count rate, amplitude, were considered in the analyses.

Theoretical models of acoustic emission signal generation due to friction are also available. (Fan et al., 2010) analyzed the relationship between AE energy and the surface characteristics, contact load, and sliding velocity. (V. M. Baranov et al., 1997) determined the AE activity levels in terms of acoustic emission counts, count rate, and the energy corresponding to different conditions that exist at the contact surfaces. (Alam & Sundaresan, 2010) numerically simulated the AE signal generation and propagation in a flat plate. Detailed characteristics of AE signals corresponding to different conditions prevailing at the contact surface were determined.

The second group of papers addresses the use of acoustic emission for diagnosis of the condition of machinery, specifically surface degradation in bearings and gear trains. (Li, 1995) used pattern classification to monitor defects in bearings using AE signals. (Al-Dossary et al., 2009) investigated the variation in RMS voltage of AE bursts to quantify implanted defects in roller bearings. Measurement and analysis of AE signals were used in condition monitoring of gears (Al-Balushi, 2002; Toutountzakis et al., 2005). Experiments based on back-to-back gearbox setup were used to monitor changes in AE RMS voltage and energy.

(Jayakumar et al., 2005) provided a review of application of AE technique for online monitoring of a variety of manufacturing processes. It was found that acoustic emissions generated during different forming processes provide useful information for detecting die wear and cracking, friction properties, state of lubrication, and others. (Meriaux et al., 2010) studied crack propagation mechanisms in fretting fatigue using acoustic emissions.

In summary, the above studies considered acoustic emission signals due to relative motion between surfaces in contact. The first group of papers reviewed here examines the

relationship between the acoustic emission signal characteristics and the conditions prevailing at the contacting surfaces. The second group of papers is on the use of acoustic emission for diagnosis of the condition of machinery, specifically surface degradation in bearings and gear trains. Theoretical models of acoustic emission signal generation due to friction are also available. In addition, some findings from other studies, which directly look at the relationship between the surface features and coefficient of friction, were also relevant for interpreting acoustic emission signals.

2.10 Summary

Several issues regarding acoustic emission for the implementation of SHM systems have been discussed in this chapter. Researchers in the past dealt with different segments of these issues. In this chapter, previous studies regarding acoustic emissions and attenuation, delamination, and friction were summarized. The summary of the results from each section were considered for the coming chapters which focus on attenuation, delamination and friction tests.

CHAPTER 3

Test Materials and AE Instrumentation

3.1 Introduction

The features or characteristics of acoustic emission signals vary depending on the source type, material type, geometry of the solid structure, and the instrumentation used to record the signals. The wave propagation characteristics exhibited by different materials are dependent on the level of homogeneity and anisotropy exhibited by the material. In this chapter, the instrumentation used for the tests reported in subsequent chapters are discussed. Comparative analysis between AE transducers is also presented. Wave propagation in aluminum and composite panels, excited under the same input signal were compared with each other. Results from sample lead break tests on steel are also presented.

3.2 CFRP Test Laminates

Two CFRP panels, labeled as panel A and panel C, were used for measuring attenuation coefficients and for performing delamination tests. Panel A had crossply $[0/90]_{6s}$ layup with total of 24 plies and panel C was a quasi-isotropic laminate having $[+45/90/-45/0]_{3s}$ layup which also had total of 24 plies. The dimensions for the panel A were 600 mm by 600 mm by 3 mm. Panel C had dimensions of 425 mm by 425 mm by 3 mm. The panels were manufactured by the process of vacuum bagging at NASA Dryden center. Before the tests were done, the panels were checked for presence of any major defects by thermography scan. Figure 3.1 shows the thermal images for the two panels.

The thermal images were taken by dividing the panels into scan areas of 100 mm by 100 mm. The images shown in Figure 3.1were assembled from a series of such smaller images. In the two images, there is a strip of darker region seen near the bottom edge which corresponds to a

teflon film inserted at the mid thickness to initiate delamination. Apart from these, the figure shows mostly uniform color distribution throughout the panels with some irregularities. Those could be attributed to presence of minor voids.

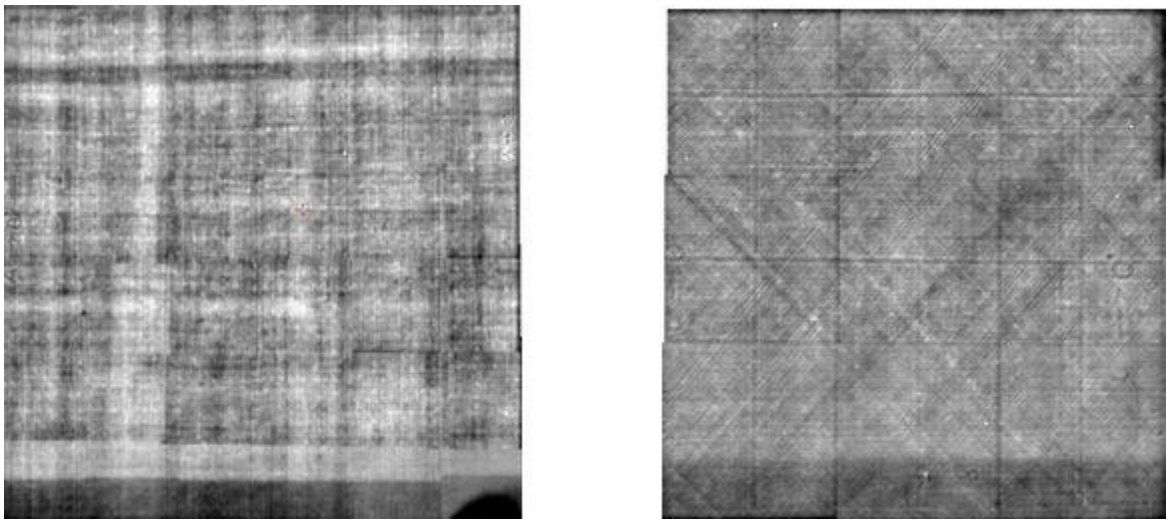

Figure 3.1. Thermal images of panel A (left) and panel C (right).

3.3 AE Instrumentation

Bonded PZT transducers (Figure 3.2). Bonded PZT transducers were the first set of transducers used for measuring stress waves in this study. The dimensions for these sensors are 20 mm by 10 mm by 0.5 mm. They are bonded on to specimens with cyanoacrylate adhesive. A reasonably strong bond can be formed between these sensors and the substrate after 24 hours of cure. The bonded PZT sensors were shown to have wide band characteristics and are sensitive to stress wave components in the range between 100 and 700 kHz. Wavelet analysis of some signals obtained using these sensors, from crack growth and friction related experiments, revealed components of the signals with frequency of 500 kHz and above (K. Asamene & Sundaresan, 2012). For crack growth and friction tests, Chapter 6, two bonded PZT sensors were used for source location.

Figure 3.2. Bonded PZT sensors on CFRP specimen.

Wideband Ultrasonic and Resonant Frequency AE Transducers (Figure 3.3). The attenuation tests (Chapter 4) were done using both bonded PZT transducers and V110 6 mm diameter, 5MHz highly damped ultrasonic transducers that exhibited reasonably flat frequency response between 100 and 700 kHz. However, these sensors were nearly an order of magnitude less sensitive than the PZT sensors. Different types of Couplant were tested to ascertain good connection between these transducers and the test panels. Ultrasonic gel, a low temperature melt solid Couplant-salol, and commercially available 3M-double sided tapes were tested. It was found that connections with less level of rigidity (double sided tape, ultrasonic gel) provide high amplitude A_o modes while connections with higher level of rigidity (Salol) give higher S_o modes. Attenuation measurements reported in Chapter4 were obtained using 3M-double sided tape. The PAC R30 resonant transducers were used in the friction tests. The primary purpose of their use in the tests was source location. In identifying the geometrical position of AE events, signals from multiple channels were used. They have operating frequency range between 100 to 400 kHz (PCI-2 based AE system manual 2004).

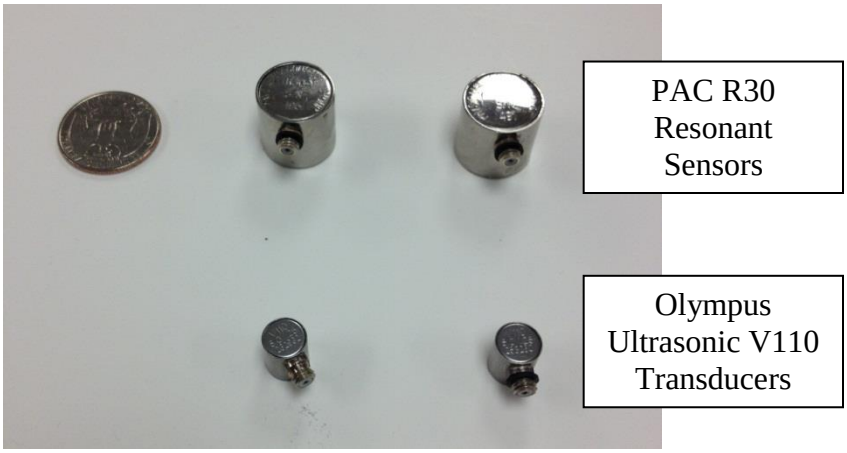

Figure 3.3. Ultrasonic wide band and resonant transducers.

Preamplifiers (Figure 3.4). The acoustic emission signals from the sensors were first amplified by PAC 2/4/6 preamplifiers before acquisition. These amplifiers have three options to multiply an input signal. These are 20 dB (10 X), 40 dB (100 X), and 60 dB (1000 X). The choice of amplification was made based on characteristics of the signals. These preamplifiers have internal filters which eliminate frequency components of signals beyond certain limit. The two types of filters were 100 – 400 kHz bandpass filters and 50 kHz highpass filters.

Figure 3.4. PAC preamplifiers.

Function Generator and Oscilloscope (Figure 3.5). In the attenuation studies and trial tests reported in this chapter, input signals to excite test panels were generated using personal

computer and HP 33120 function generator. In some cases, it was necessary to further amplify the signals from the function generator. ENI model 2100 NL 50 dB (316 X) was used for this purpose. The frequencies and amplitudes of the signals applied to the transmitting transducer were monitored using Lecroy LT344 Oscilloscope.

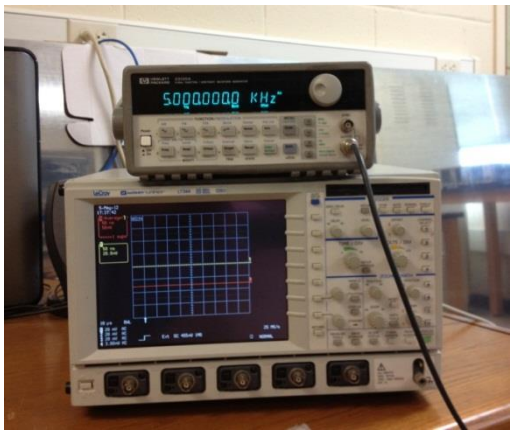

Figure 3.5. Function generator and oscilloscope.

PCI-2 Data Acquisition and AEwin3.2 Software (Figure 3.6). All the signals from the receiving sensors were recorded by PCI-2 data acquisition system. AEwin 3.2 software was used for data acquisition and replay. This software is capable of recording the waveforms from AE sensors and extracting AE features.

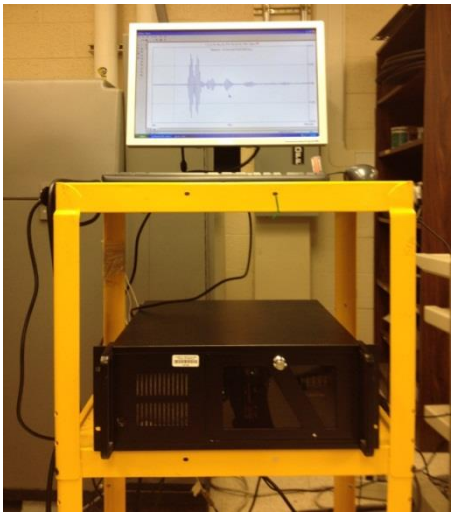

Figure 3.6. PCI-2 data acquisition system.

Material Test system (MTS 810) – Delamination tests and friction tests were done using MTS 810's. The machines are capable of applying loads of 20 kips (88 kN) and 50 kips (222 kN) respectively. Load, displacement and strain values measured by the sensors in the MTS machines were directly connected to the PCI-2 data acquisition system so that the parameters corresponding to each AE event could be recorded.

3.4 Comparison between Transducers

The characteristics of signals are dependent on the type of transducer used in a test. A comparative study was done on the three types of transducers discussed in the earlier section. The transducers were mounted on an aluminum test panel. The panel was excited by Gaussian pulse of know frequency. Each of the transducers were located at a distance of 150 mm away from the source of excitation. An ultrasonic transducer was used as the transmitting transducer. Stress wave signals received by the three sensors for a range of frequencies between 100 and 700 kHz were compared. Figure 3.7 shows the signals received for input pulse at 300 kHz.

The figures indicate that the bonded sensors provide an amplitude response which is far higher than the ultrasonic and resonant transducers. Bonded PZT sensors were found to have an order of magnitude higher sensitivity compared to other sensors in some frequencies. The amplitude readings over some frequency ranges go beyond 10 times that of the amplitude from the ultrasonic and resonant transducers. All the sensors had weak response to S_o modes for frequency ranges less than 150 kHz. On the other hand, the A_o modes had the least of presence above 400 kHz. The resonant sensor, as expected, had its peak oscillation near 300 kHz and it was particularly sensitive to A_o modes. With sufficient distance of propagation, the symmetric and antisymmetric modes of wave propagation were distinguishable in the case of ultrasonic and PZT transducers which are displayed as the initial two pulses.

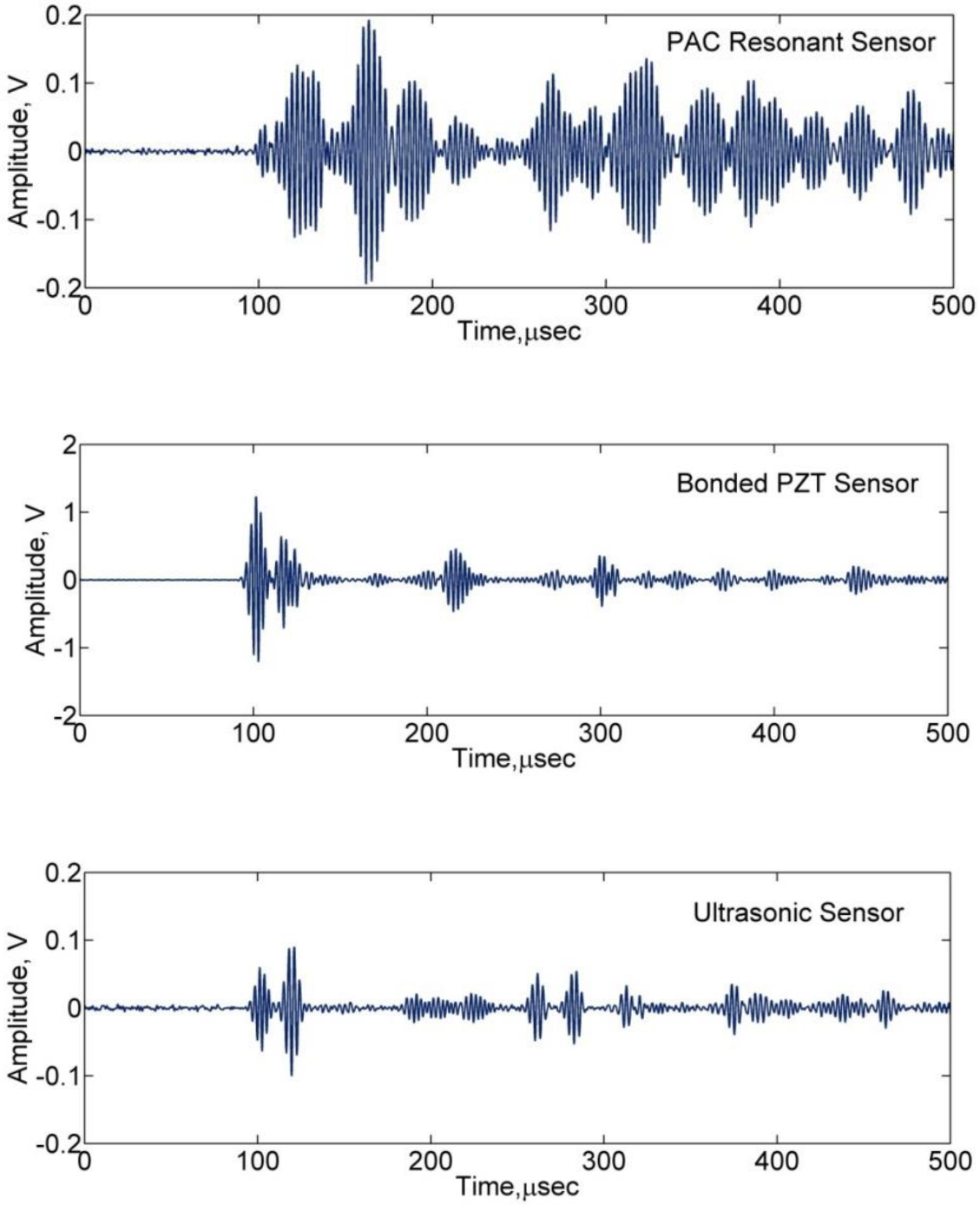

Figure 3.7. Comparison of the three different sensor responses to 300 kHz pulse in a 3 mm aluminum panel.

Sensitivity of receiving transducers to different frequency components and modes were examined. A series of experiments were conducted in which Gaussian pulses with frequencies ranging from 100 kHz to 700 kHz were applied to the transmitting V110 ultrasonic transducer attached to the crossply laminate. The resulting stress waves were measured by the transducers after propagation distance of 75 mm in the 0 degree direction of the laminate. The Bonded PZT transducer was highly sensitive to frequencies below 400 kHz and in particular for S_o mode. Response of the transducers to different frequency components of a signal may not be uniform and is an important characteristic feature. Similar to the earlier section, Gaussian pulses which vary in central frequency were used to excite the crossply laminate and the responses were obtained. Figure 3.8 shows the relative amplitude distribution of the response waveforms obtained using the bonded PZT and ultrasonic V110 transducers.

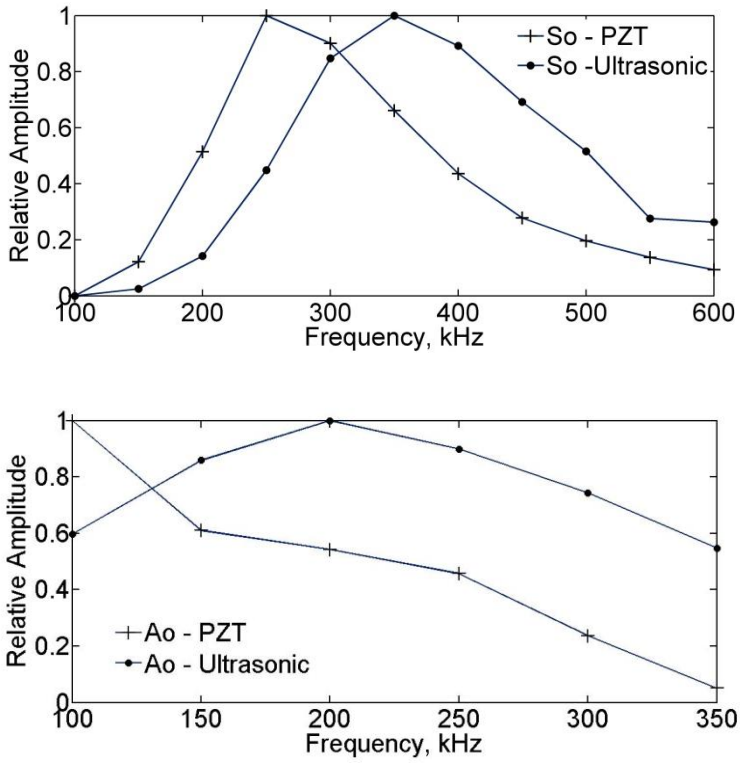

Figure 3.8. Receiving transducer's efficiency across the frequency band for the different modes.

The PZT transducers have higher amplitude response at 250 kHz for S_o mode and the amplitude decays faster as the frequency increases. They have peak amplitude response at 200 kHz for A_o modes. However, the reduction in amplitude response to A_o modes is moderate as compared to PZT transducers. The ultrasonic transducers have peak amplitude response to S_o modes at 350 kHz and the percentage reduction of amplitude with increase in frequency is lower than PZT transducers. To take advantage of high amplitude response of PZT transducers lower frequency ranges, i. e. frequency range less than 300 kHz, combination of these two sensors was used in the attenuation studies.

3.5 Lead Break Tests

It is a common practice to use lead-break tests to verify performance of acoustic emission sensors and systems before the loading of test specimens. In this research, before conducting any of the tests reported in the later chapters and the preliminary tests reported in this chapter, lead break tests were conducted on the test specimens to check connection of the sensors and examine the noise level exhibited in the signal waveforms. Breaking lead on the specimen is assumed to simulate discrete events such as crack growth. The signals from lead break tests also serve as base line for comparison and this helps to interpret signals of interest. Figure 3.9 shows a waveform obtained from lead break test on a steel bar. PZT sensors were bonded on the steel bar surface. A 3 mm long and 0.5 mm diameter HB pencil lead was broken 50 mm away from the PZT sensors to generate the waveform. Here both the waveform and its wavelet transform are included. AGU Vallen wavelet software was used to obtain the wavelet diagram. These waveforms had peak amplitude of nearly 2 volts and started with large amplitude which drops rapidly. There is a second segment after about 110 μs, due to reflections from the ends of the bar. There is a period of very little signal amplitude between the initial pulses and the reflections.

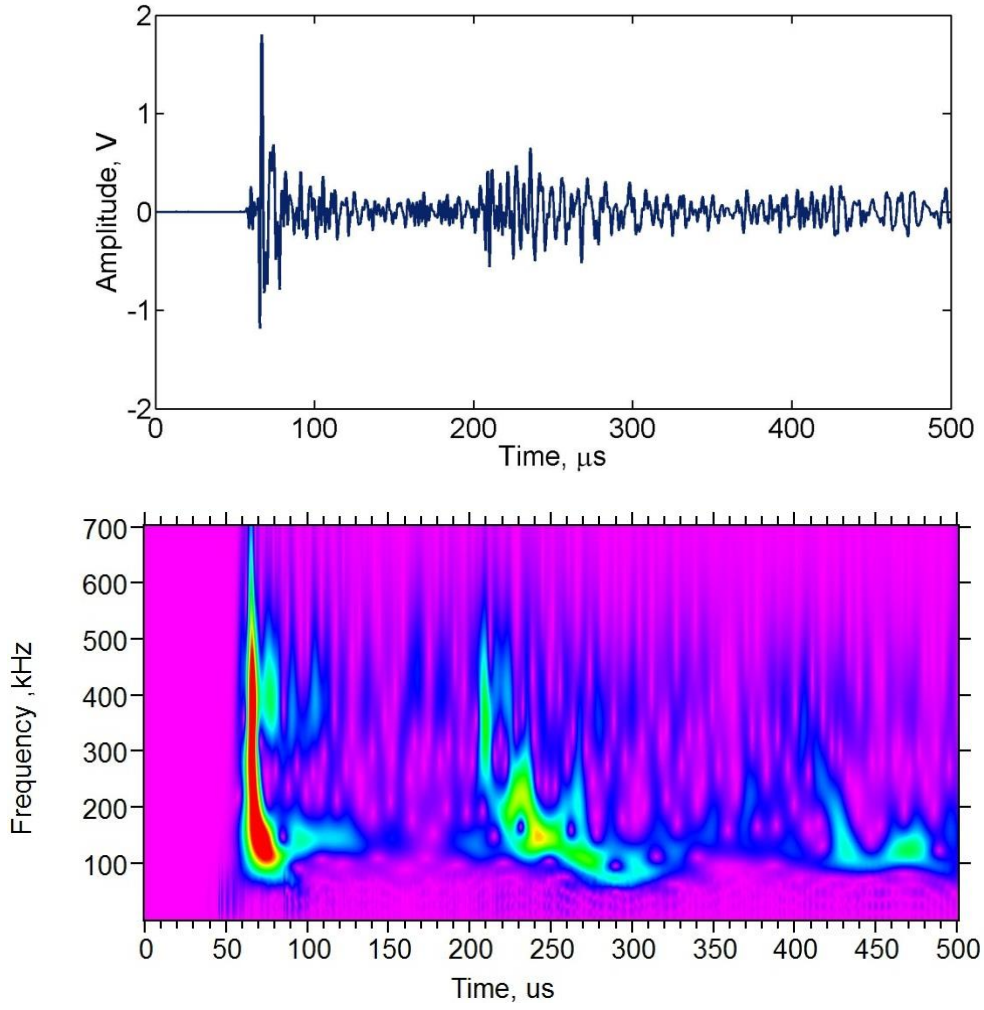

Figure 3.9. Waveform and wavelet from a lead break acoustic emission event.

3.6 Cases of Wave Propagation in Aluminum and Composite Panels

The properties of guided waves such as the group velocities and dispersion of the different modes depend on the geometry and material properties of the wave guide along the propagation path. Figure 2.15 showed the dispersion curves for aluminum plate. Similar dispersion curves which were generated experimentally for the two types of CFRP panels. The results are presented in figure 3.10. Here the curves are generated for the fundamental A_o and S_o modes along 0 deg direction for the two laminates.

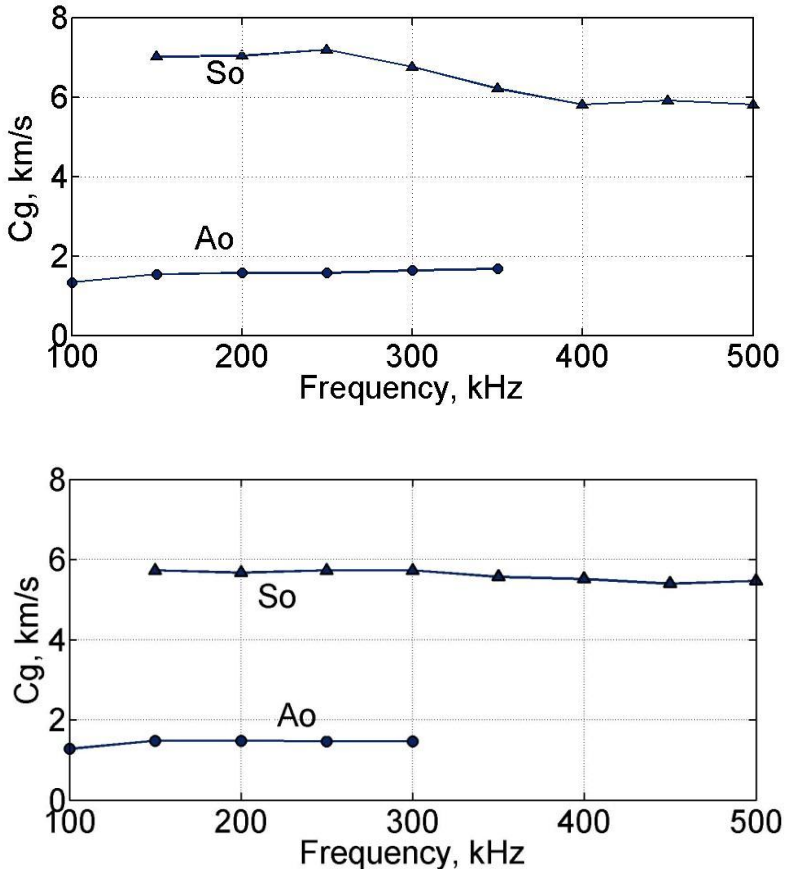

Figure 3.10. Dispersion curves for crossply (top) and quasiisotropic (bottom) panels along 0 degree directions.

The influence of difference in the dispersion characteristics and attenuation is depicted by variations of the response waveforms obtained under similar test conditions, i.e. same type of transducers, input signals and data acquisition settings. Sample waveforms received in aluminum panel and crossply laminate are in Figure 3.11 for the purpose of comparison. The initial series of pulses seen in these waveforms correspond to different modes arriving at different times because of the differences in their velocities. Pulses in the later portion of the waveforms correspond to multiple reflections from the edges of the panels. Reflections decay more rapidly in the composite laminates because of higher level of attenuation.

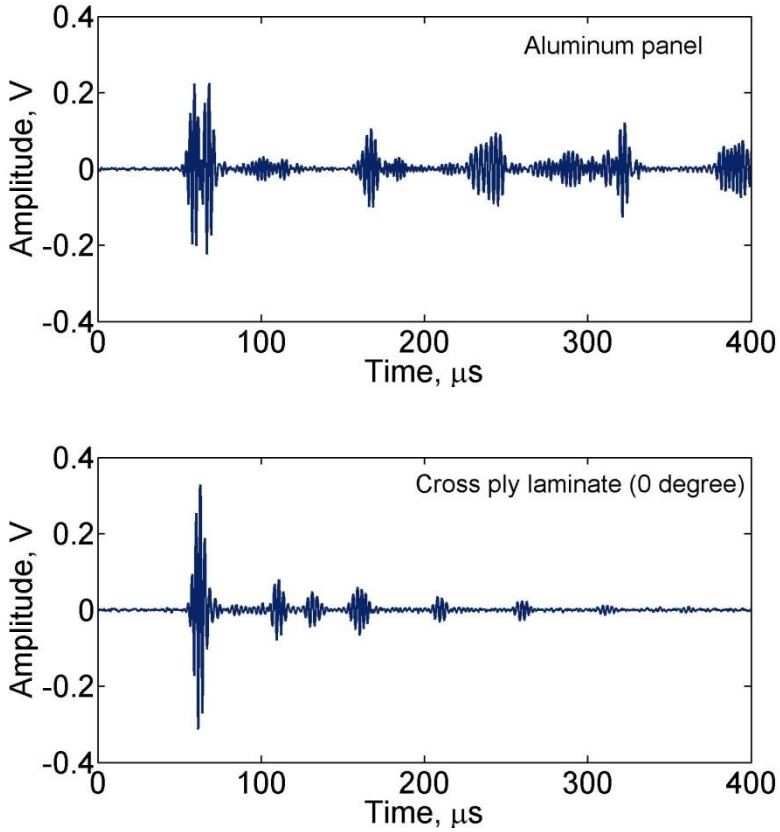

Figure 3.11. Response waveforms at 400 kHz as detected by an ultrasonic transducer after propagation of 75 mm.

CHAPTER 4

Attenuation Tests

4.1 Introduction

Influence of attenuation on acoustic emission signals in CFRP panels is examined in this chapter. Acoustic emission events occur as combinations of several modes of wave propagation over varying frequency ranges. The features of these signals as well as the constituent modes change with distance of propagation. It was mentioned in the second chapter that attenuation due to different mechanisms affects the features of acoustic emission signals. Attenuation coefficients were determined experimentally for the two types of CFRP panels, A &C, described in the earlier chapter. The coefficients were determined for the fundamental symmetric and antisymmetric wave propagation modes. The panels were excited at different frequencies and the responses were measured at different distances along different directions. The objective of this part of the research has been to characterize the attenuation behavior of the panels with respect to distance, direction and frequency, and demonstrate how the attenuation due to material absorption and scattering affect the features of acoustic emission signals. Acoustic emission events consisting of the fundamental modes were numerically simulated for the panels. The numerical simulations considered geometric spreading and dispersion experienced by the wave modes during propagation. The attenuation coefficients obtained experimentally were applied to the numerical waveforms to include the effect of material absorption and scattering. The energy feature of the resulting waveforms was calculated and plotted with respect to distance of propagation to show influence of attenuation on the signals. The details are presented in the following sections.

4.2 Experimental Setup

Attenuation coefficients for two different laminate configurations were measured. They consisted of a cross-ply laminate with stacking sequence of $[0/90]_{6s}$ and a quasi-isotropic laminate with stacking sequence of $[+45/90/-45/0]_{3s}$, both of which had a total of 24 plies. The dimensions of the cross-ply and quasi-isotropic laminates were 600mm x 600 mm x3 mm and 425 mm x 425 mm x 3 mm respectively. The laminates were inspected using thermography to ensure that they were free from major defects.

Single frequency gated sine pulses at frequencies ranging from 100 kHz to 700 kHz, in 50 kHz increments, were introduced at locations selected to minimize the effect of reflections from the edges and the amplitudes of received pulses were measured along the directions along 0, 30, 45, 60, and 90 orientations as shown in Figure 4.1. Along each of these directions, the received signal amplitude was measured at points spaced 25mm apart up to a maximum distance of 200 mm.

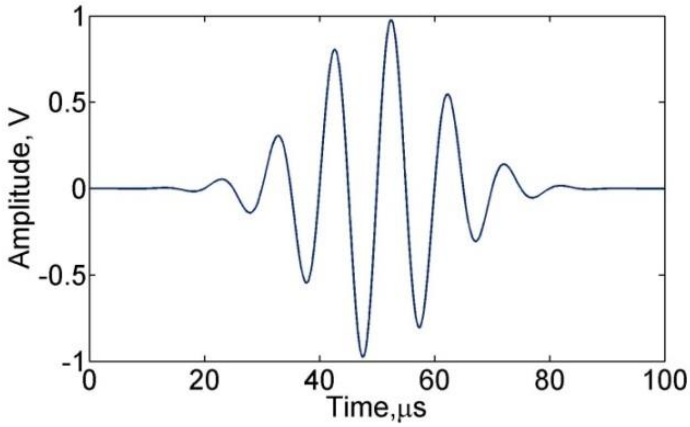

Figure 4.1. Gaussian pulse at 100 kHz.

At each of these locations, the amplitudes of the received signals were measured on both surfaces of the laminate, so that the symmetric and antisymmetric components of the signals could be separated by the addition and subtraction of the signals. The stress wave signal was

introduced into the laminate in the majority of cases using a 5 MHz, 6 mm diameter, damped ultrasonic V110 transducer. It was used to generate A_o modes in cases. The amplitude of the received signals, for all cases, were measured over the entire range of frequencies using a similar ultrasonic transducer. To efficiently generate S_o mode, particularly below 350 kHz, bonded PZT wafer bonded to the surface of the laminate was used.

Depending on the laminate stacking sequence, direction of wave propagation, lamb wave mode, and frequency of excitation, the excitation signal amplitude and gain applied to received signal were varied to obtain adequate signal to noise ratio. The received waveforms were amplified by a preamplifier with 50 kHz high pass filter and recorded in a commercial AE monitoring system set to 5 MHz sampling rate.

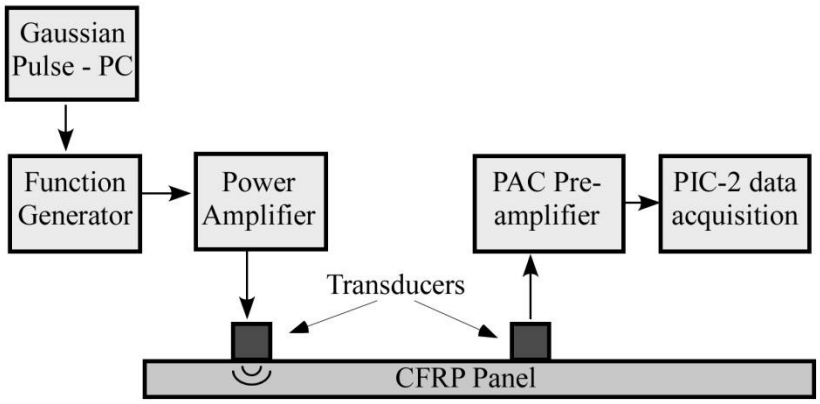

Figure 4.2. Schematic representation of attenuation measurement.

Depending on the panel or laminate type, mode type and direction of measurement, the amplitude and preamplification of the input signal to excite the panels were varied. To measure A_o mode attenuation, 200 mV peak-to-peak Gaussian pulses amplified by 50 dB gain was applied. For S_o mode measurement in panel C, Gaussian pulse of 5V peak-to-peak amplitude without amplification was used. Similarly, For A_o mode measurement in panel A, Gaussian pulse of 5V peak-to-peak amplitude was used without amplification. However, for degrees of 30, 45,

60 degrees, 100 mV peak-to-peak amplitude pulse which was enhanced by 50 dB gain power amplifier was applied to excite the panels. Peak-to-peak voltage levels were chosen based on the resolution level in the waveforms and saturation magnitudes of the data acquisition system.

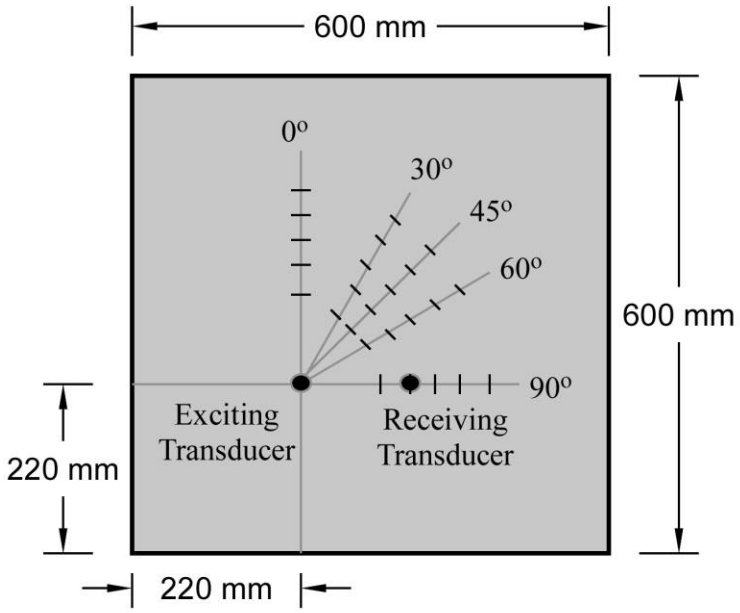

Figure 4.3. Angles of measurement for panel A.

4.3 Data Analysis

4.3.1 Identification of wave modes. The A_o and S_o modes were identified from a signal waveform by making use of two waveforms obtained from opposite faces of a panel. Two points at exactly same distance from the source, but located on opposite faces, experience out of plane displacement which is symmetric with respect to the mid plane of the panel in the case of S_o mode propagation. The displacement pattern is antisymmetric in the case of A_o mode propagation. Thus, the z-displacements or strains detected by transducers on opposite faces are in-phase with each other for S_o mode propagation and out of phase with each other for A_o mode propagation. Figure 4.4 shows two waveforms obtained at the same location but on opposite faces. The waveforms were obtained for measurement on panel A along 0 degree direction at

frequency of 200 kHz. At the beginning the two waves are coincident with each other - S_o mode. After about 50 μsec, the displacements become out of phase - A_o mode.

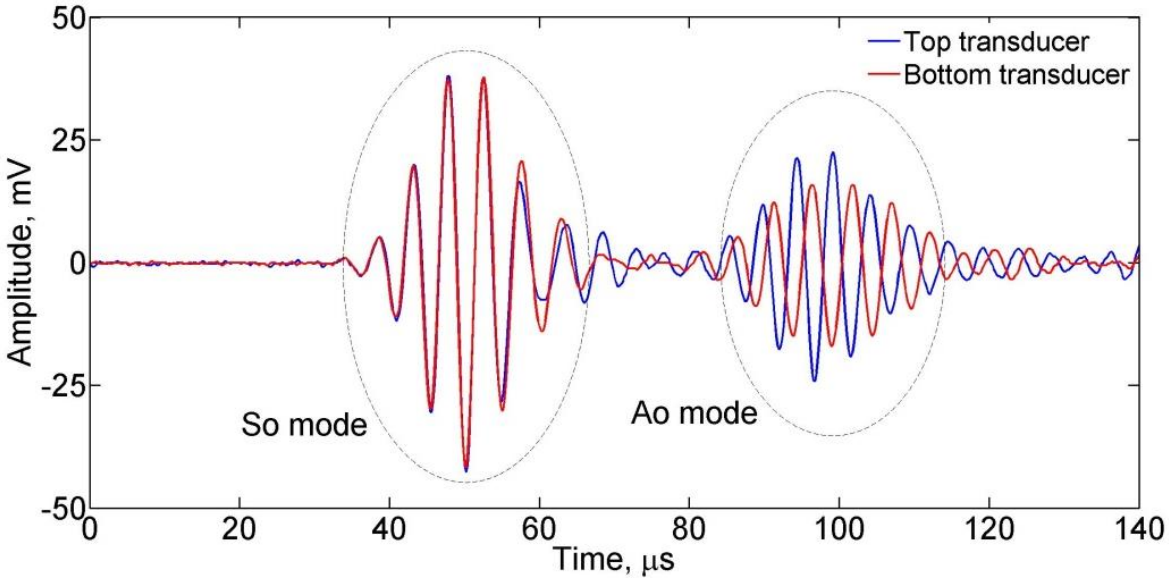

Figure 4.4. Identification of S_o and A_o modes.

4.3.2 Calculation of attenuation coefficients. The procedure to calculate attenuation coefficients from the experiments are detailed in this section. The attenuation behavior, as discussed earlier, is affected by geometric spreading, material absorption, dispersion and scattering. Using two points, located at distance x_1 and x_2 from source, Equation 3.1 is used to calculate the attenuation coefficient (α).

$$\alpha = \left(\frac{1}{x_2 - x_1}\right)\ln\left(\frac{V_1\sqrt{x_1}}{V_2\sqrt{x_2}}\right) \tag{4.1}$$

In the equation, v_1 and v_2 represent the voltage amplitudes of the waveforms obtained at the two locations. In this test, peak amplitudes of both A_o and S_o modes correspond to the $v_{i's}$ used for the calculation of the attenuation coefficients. At a given direction, measurements of points were made at multiple points located 25 mm from one another. Hence, multiple attenuation coefficients were obtained for a given frequency along that direction.

Least squares method was used to obtain the value which minimizes the error function (equation 4.2). v_i represents the voltage measure at a location and x_i is the distance from the source to the location. *V* refers to the strength of the signal at the source.

$$\varepsilon = \sum_{i=1}^{N}(|v_i| - |V|e^{-\alpha x_i})^2 \tag{4.2}$$

Thus, when multiple attenuation coefficients are available, the following equation (4.3) was used to determine an attenuation coefficient at a specific central frequency. *N* represents the number of locations at which signal waveform, and hence signal amplitude was measured for attenuation calculation.

$$\begin{Bmatrix} -\alpha \\ \ln(V) \end{Bmatrix} = \begin{bmatrix} \sum_{i=1}^{N} {x_i}^2 & \sum_{i=1}^{N} x_i \\ \sum_{i=1}^{N} x_i & N \end{bmatrix}^{-1} \begin{Bmatrix} \sum_{i=1}^{N} x_i \ln(v_i) \\ \sum_{i=1}^{N} \ln(v_i) \end{Bmatrix} \tag{4.3}$$

For S_o modes, despite the measurements were taken at ten different locations, at a specific frequency, the measurements of the waveforms made at seven different locations were chosen. Six attenuation coefficients were obtained from these. The coefficient which best averages the different values was obtained using equation (4.3). Similarly, there were four locations chosen for the A_o modes. For both Panel A and Panel C, the attenuation coefficients were calculated using these procedures along the five directions discussed earlier. For the S_o modes, the range of frequencies chosen were between 200 and 500 kHz, while for the A_o modes, the range considered was between 100 and 300 kHz.

4.3.3 Amplitude vs distance. The symmetric modes were identified from each of the measured waveforms along all directions. Figures 4.5 (a) and (b), and Figures 4.6 (a) and (b) show the reduction in amplitude and the percentage reduction in amplitude of S_o modes for panel A and C. The results are obtained for measurement at angle of 0 degrees.

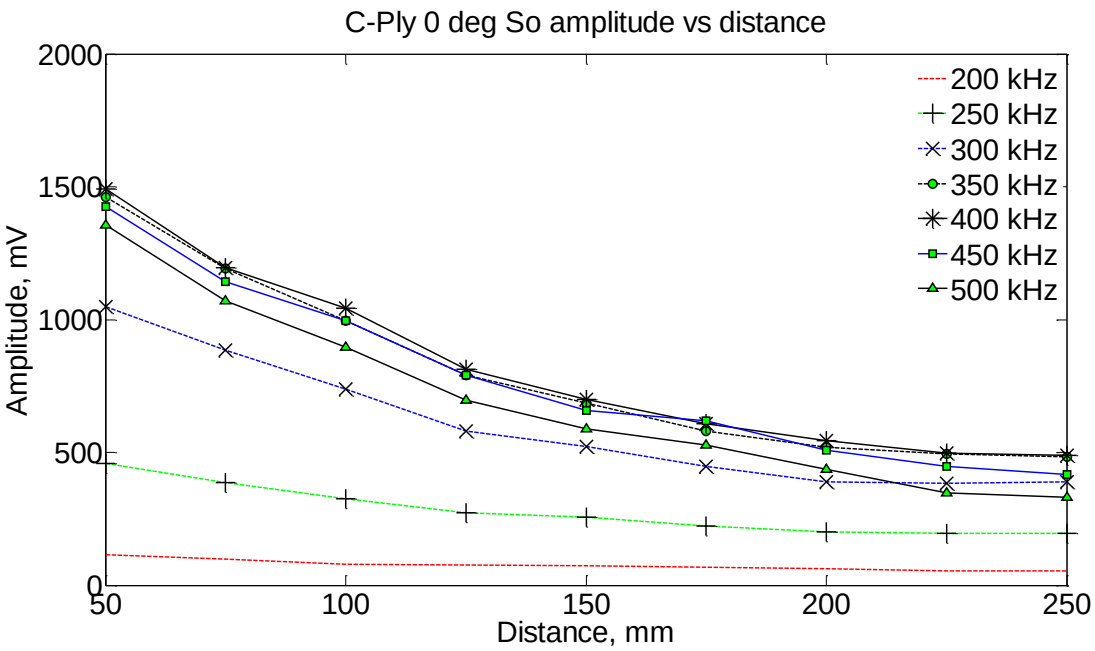

(a)

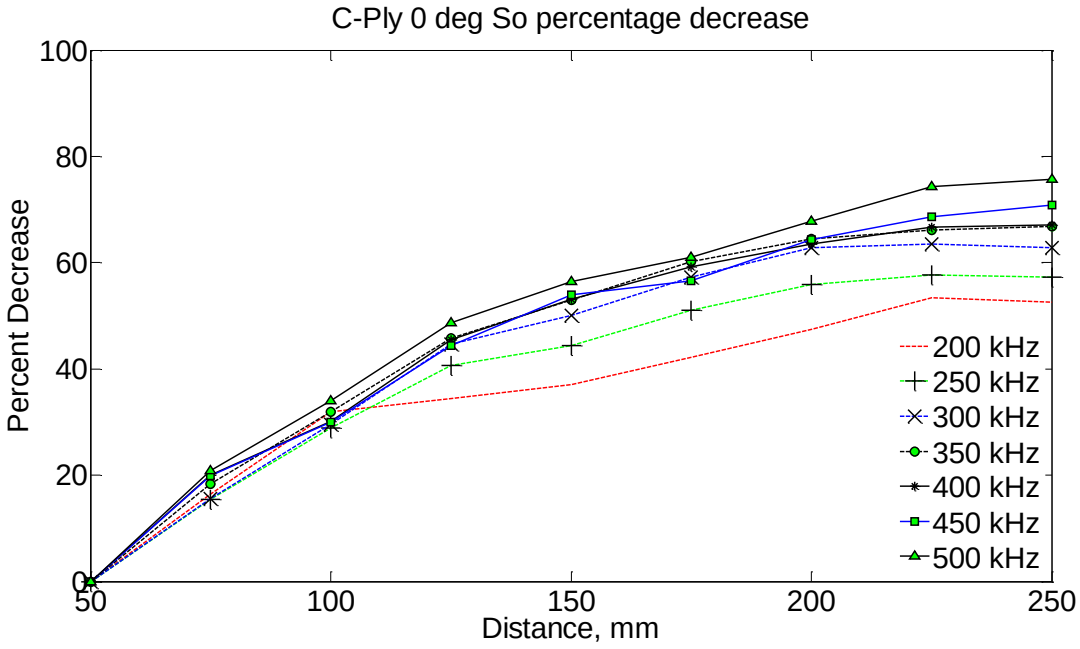

(b)

Figure 4.5. S_o mode for panel A (a) amplitude vs. displacement (b) percentage of reduction in amplitude with distance.

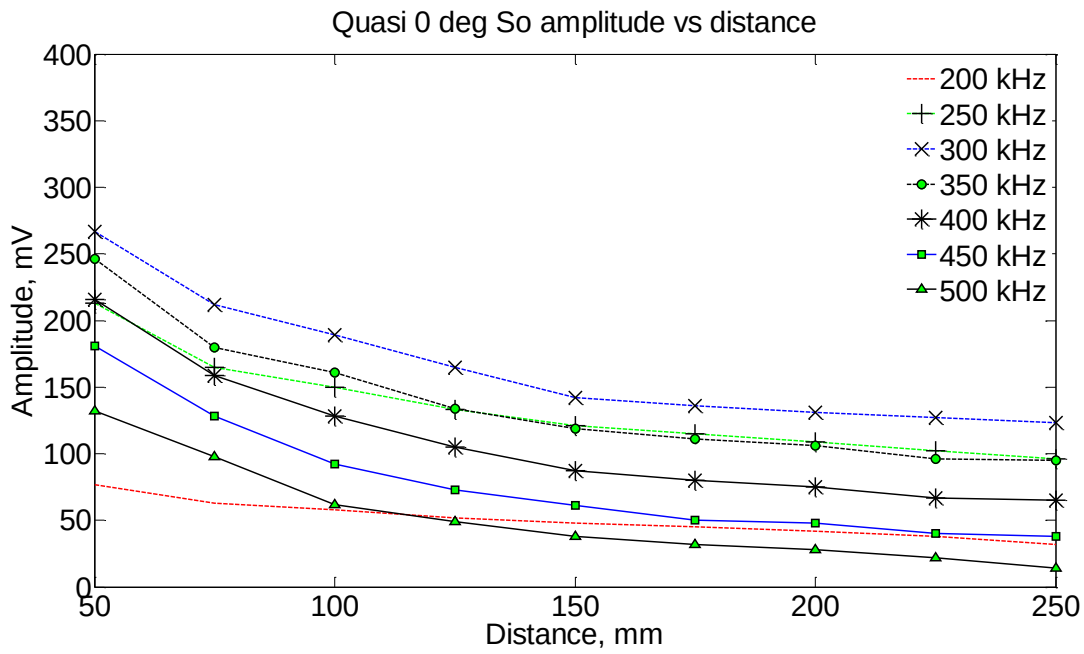

(a)

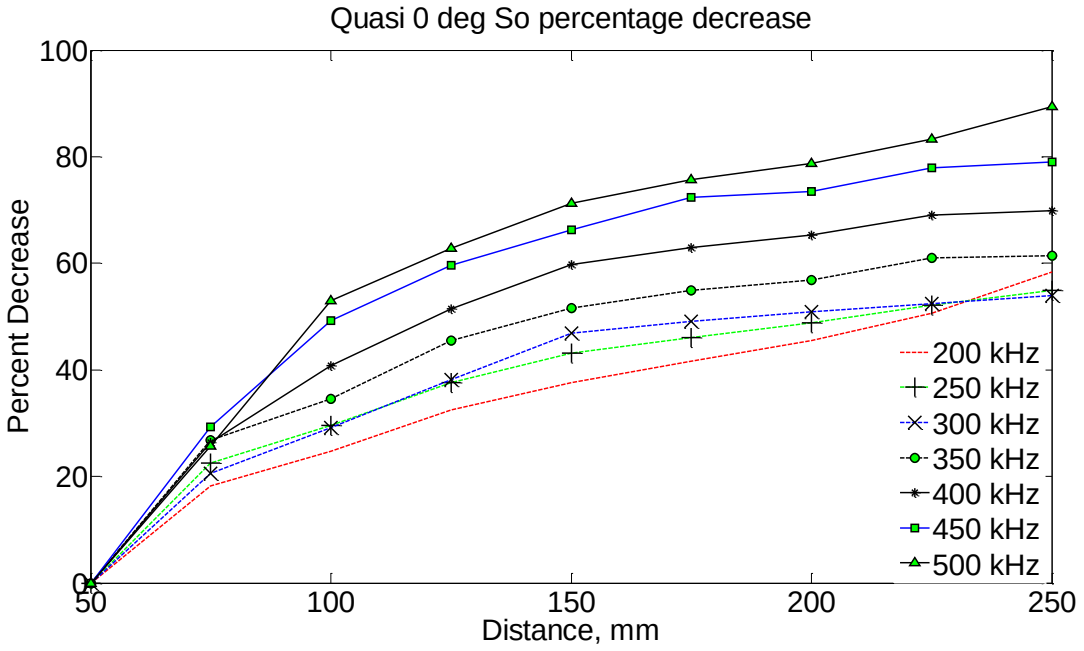

(b)

Figure 4.6. S_o mode for panel C (a) amplitude vs. displacement (b) percentage of reduction in amplitude with distance.

The waveforms obtained for panels A and C indicate that the maximum amplitudes for S_o modes occur at frequencies of 300 and 350 kHz. The amplitudes increase with increase in frequency up to these values and start to fall down with further increase in frequency. The amplitude of the S_o modes remains comparable with respect to angle variation for the quasi-isotropic laminate (panel C). However, the amplitudes vary significantly with angle of measurement for the case of crossply laminate (panel A). At 45 degrees of measurement, the maximum amplitude at 300 kHz is about a tenth of the maximum amplitude at the same frequency for 0 degree of measurement. In crossply laminates, the amplitude of S_o mode signals at angles of 30^o, 45^o, and 60^o over a wide frequency range was about $1/6^{th}$ of the amplitudes at 0 degrees. The percentage of decrease in amplitude, as can be seen in Figures 4.5 and 4.6 (b), increases with increasing frequency. In both cases, it was shown that the amplitudes decay faster at 500 kHz than any other signal frequency. The percentage decrease in amplitude was slightly lower for 0 and 90 degrees for panel A, while it was nearly similar or consistent along all directions for panel C.

Similar to the case of symmetric modes, the antisymmetric modes were identified from each of the measured waveforms. Figures 4.7 (a) and (b), and Figures 4.8 (a) and (b) show the reduction in amplitude and the percentage reduction in amplitude of A_o modes for both panel A and panel C. The results are obtained for measurement at angle of 0 degrees.

The range of frequencies and distances chosen for the two panels were different because of considerations of reflections. For panel C, the reflections of S_o modes from the boundaries were found to interfere with A_o modes for distances of 85 mm and beyond. Thus, the measurements were taken up to distance of 75 mm only. At distance of 25 mm, for frequencies of 250 and 300 kHz, there is slight merger of the S_o and A_o modes. However, the occurrence of

the peak points for the modes were well separated and the amount by which the interference affects the A_o amplitude is less than 2%.

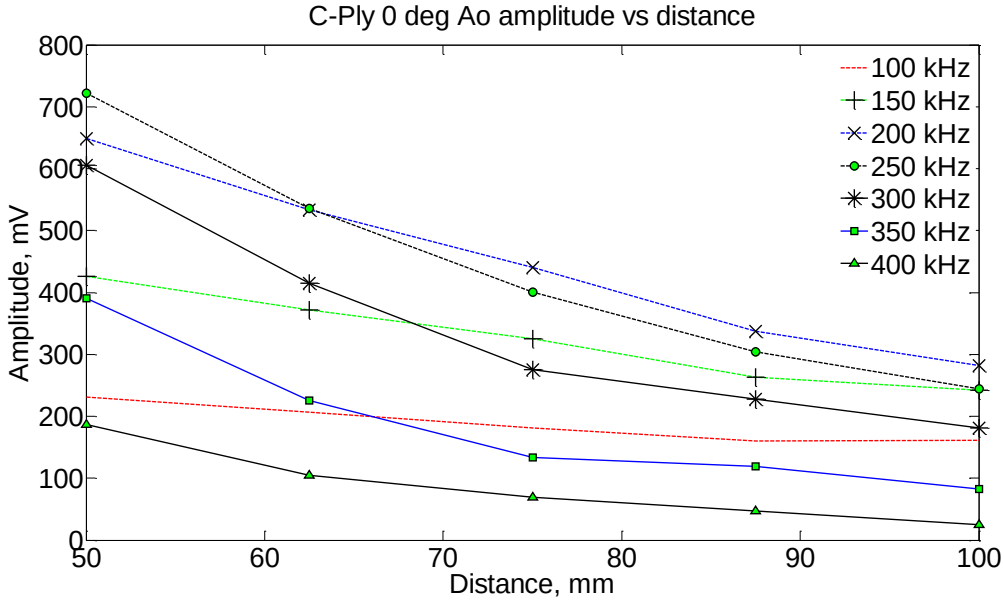

(a)

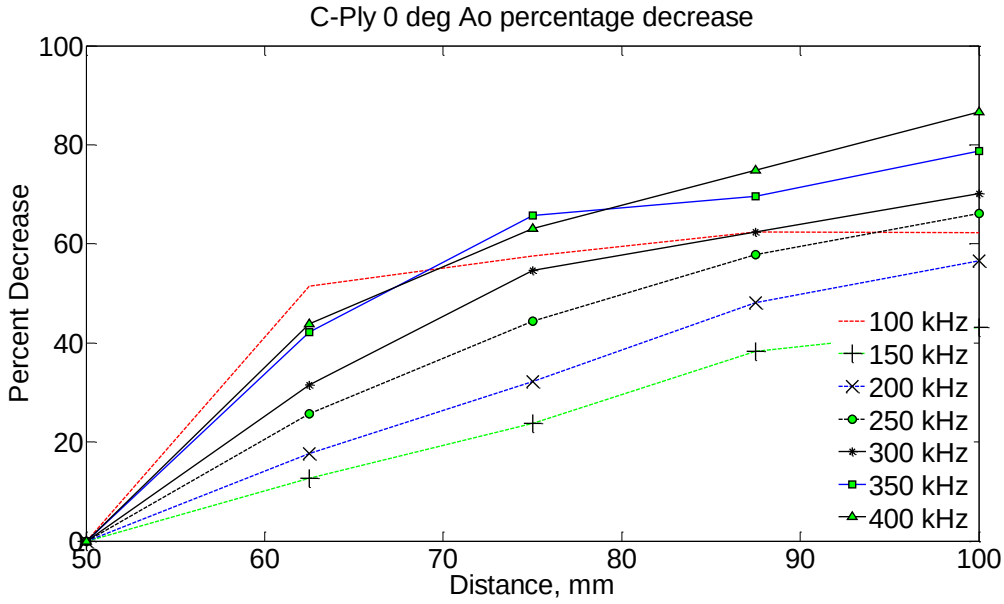

(b)

Figure 4.7. A_o mode for panel A (a) amplitude vs. displacement (b) percentage of reduction in amplitude with distance.

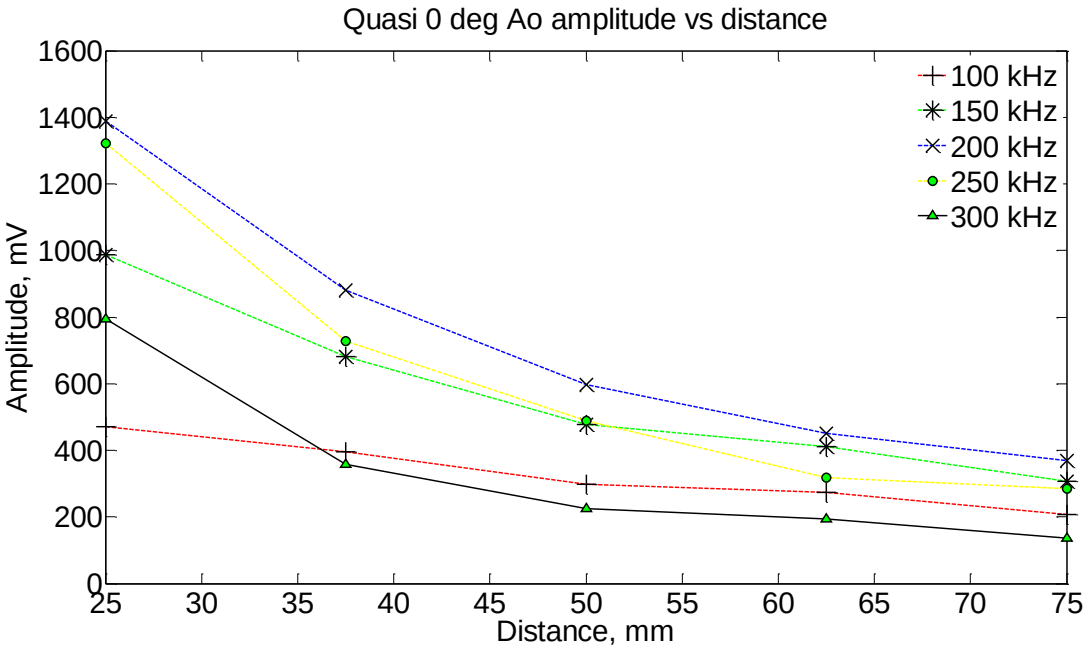

(a)

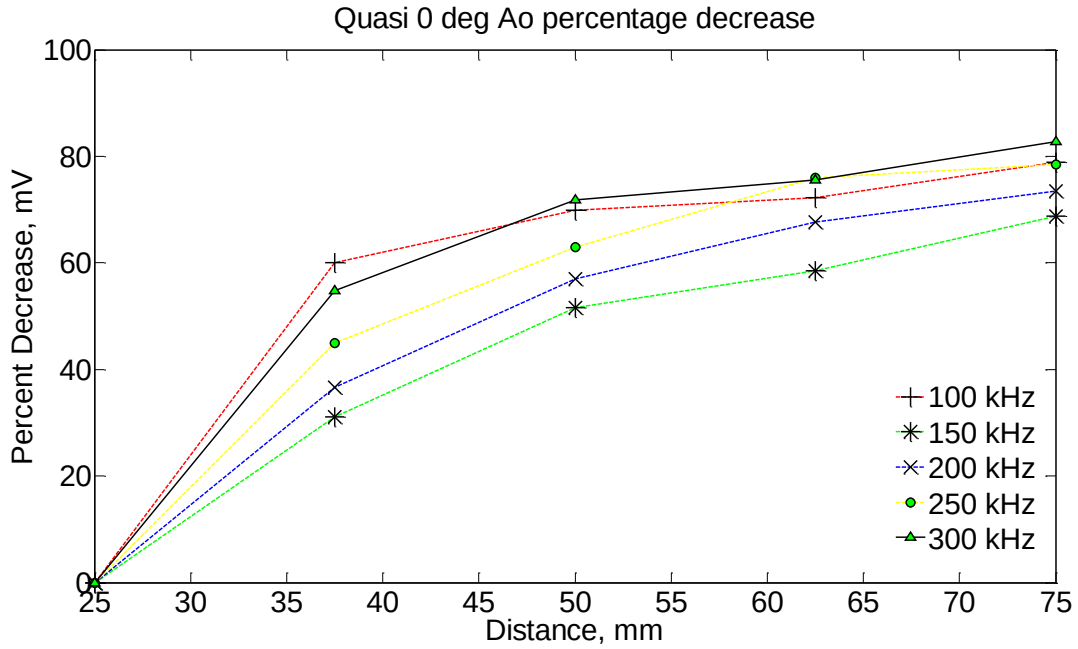

(b)

Figure 4.8. A_o mode for panel C (a) amplitude vs. displacement (b) percentage of reduction in amplitude with distance.

The highest A_o mode amplitude in both panels occurred at frequency of 200 kHz at all distances at and at all directions. Similar to the case of S_o modes, the amplitudes were nearly direction independent for the quasi-isotropic panel (panel C). The lowest percentage decrease occurred along 0 deg direction for panel A and slightly lower percentage decrease was noticed in Ao modes measured along 45 degree direction for panel C. The reduction in Ao mode amplitudes for frequencies of 150 kHz and above is quite drastic in which is in contrast to S_o modes. 40% to 60% reduction in amplitude occurs over the first 25 mm of propagation distance, and 70% to 90 % reduction occurs over 75 mm of distance. In S_o modes, depending on the frequency of excitation, it takes a propagation distance of 225 mm and beyond to experience 70% to 90 % reduction in amplitude which is three times the propagation distance for A_o modes.

4.3.4 Attenuation coefficients for the CFRP panels. Equation 4.3 was used to calculate the attenuation coefficients. Figures 4.9 (a) and (b) show the S_o mode attenuation coefficients obtained for panels A and C along directions of 0 degrees. Similarly, Figures 4.10 (a) and (b) show the A_o mode attenuation coefficients for the same panels along direction of 0 degrees. Attenuation coefficient plots generated for other cases are attached in Appendix A.

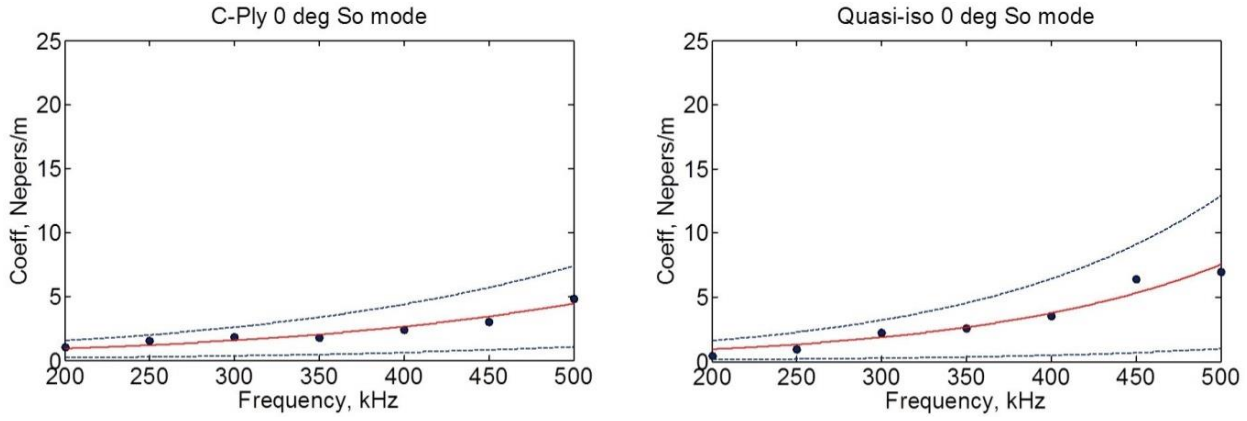

(a) (b)

Figure 4.9. S_o mode attenuation coefficients (a) Crossply (b) Quasi-isotropic.

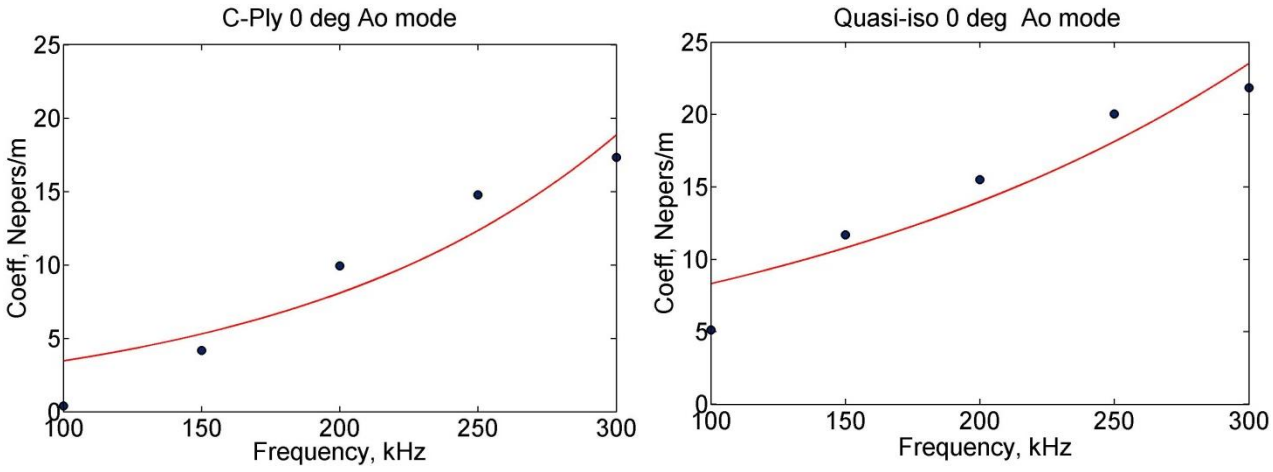

(a) (b)

Figure 4.10. A_o mode attenuation coefficients (a) Crossply (b) Quasi-isotropic.

A_0 mode attenuation coefficients in crossply specimens*:* Because of the steep increase in attenuation with frequency seen in A_0 modes, measurements could be made only to a maximum frequency of 300 kHz in the composite laminates. At 100 kHz frequency, attenuation was observed to be lower in the 0 and 90 directions with a value of about 3 Nepers/m while along 30, 45, and 60 degree directions, the attenuation was over 10 Nepers/m. The rates of increase of the attenuation with frequency were found to be different for different directions. The attenuation coefficient at 300 kHz was found to lie between 17 to 23 Nepers/m along the five directions considered here.

S_0 mode attenuation coefficients in crossply specimens: Attenuation in S_0 modes were found to be much smaller compared to A0 modes and could be measured between the frequencies of 100 kHz and 500 kHz. There was significant variation of attenuation levels in the 5 different directions considered. At 100 kHz the attenuation was in the range of 0 to 2 Nepers/m in all the five directions. However, at 500 kHz, the attenuation was found to be only 2.5 Nepers/m along 60 degree direction while along 90 degree direction it was about 8 Neper/m. In the other three directions, attenuation values were between these two values.

A_0 mode attenuation coefficients in Quasi-isotropic specimens*:* As in the case of cross-ply specimens, there was a steep increase in attenuation with frequency of A_0 modes, in quasi-isotropic laminates as well. At 100 kHz frequency, attenuation values varied between 6 and 11 Nepers/m. The values had lower values at 30 and 60 degrees direction. The attenuation values at 300 kHz varied between 13 and 31 Nepers/m. Similar to the case of crossply laminates, the rate at which attenuation increased frequency was different along the different directions.

S_0 mode attenuation coefficients in crossply specimens: Attenuation values of S_0 modes in quasi-isotropic laminate were much lower compared to A_0 modes. Attenuation values of 100 kHz signal in the five directions considered here were about 1 Neper/m. However, the rate at which S_0 mode attenuation increased differed with frequency significantly among different directions. Along the 60 degree direction, attenuation remained unaffected by the frequency within the range considered. Along the other four directions, the attenuation values at 500 kHz ranged from 6 Nepers/m to 10 Nepers/m.

In general, A_0 modes were found to have significantly higher levels of attenuation compared to S_0 modes in both the cross-ply and quasi-isotropic laminates. In these polymer matrix composite laminates, each combination of modes and frequency is likely to result in a different state of strain including in-plane strain components and their variation across the thickness. The resulting deformation of the material is unevenly distributed between the reinforcing fibers and the polymer matrix. It is expected that when the matrix material shares the bulk of deformation, the viscoelastic nature of the matrix will result in greater attenuation of the propagating stress wave. Variations in the modes and frequencies result in changes in the strain and deformation components among the different laminae within the laminate which in turn will affect the attenuation values.

The directionality of attenuation behavior was exhibited to a limited extent. Comparison of S_o mode attenuation values gave results which were very comparable with each other, for both laminates. However, attenuation values for 30 and 60 degrees in both laminates were higher particularly for crossply laminates as shown in Figure 4.11.

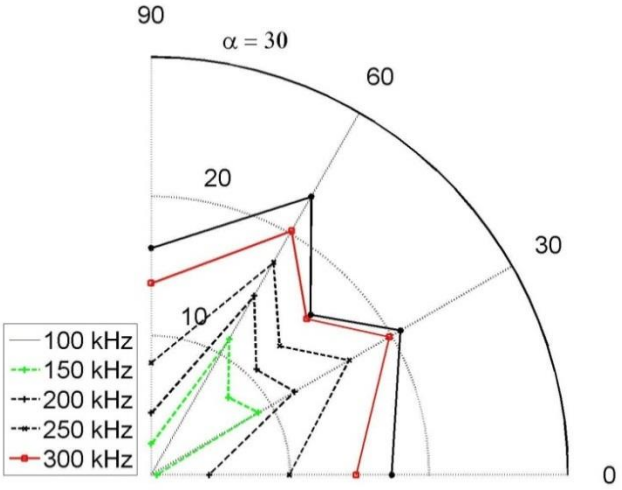

(a)

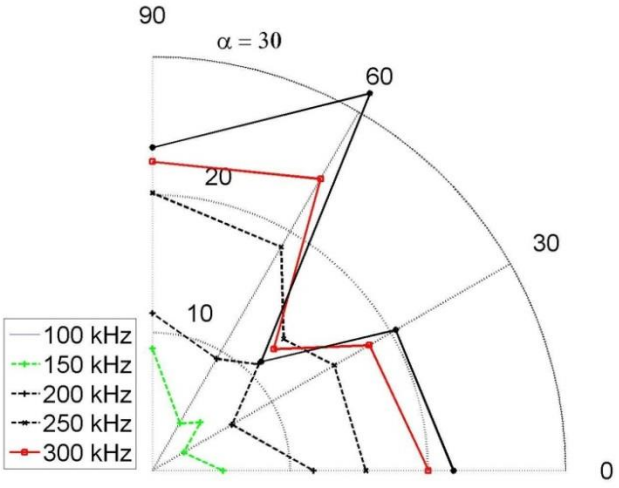

(b)

Figure 4.11. A_o mode attenuation coefficients vs direction (a) Crossply (b) Quasi-isotropic.

4.4 Numerical Simulation

Wave propagation due to an acoustic emission event was simulated using VPG and ANSYS LS-DYNA and the results were displayed on LS-PREPOST. The simulation mainly consisted of symmetric and antisymmetric modes of wave propagation in the composite panels. The method used here considers that the energy released during an acoustic emission event can equivalently be represented by short duration impulse type load applied on the numerical model. Hence, in the models, triangular impulse having width of 1us was used to simulate the acoustic energy release. Application of the pulse type load at the neutral axis of the numerical model gives rise to symmetric modes while when the impulse is applied at a surface node of the model, symmetric and antisymmetric modes of wave propagation were noticed. The method was tested on aluminum model and sample waveform is shown in figure 4.12.

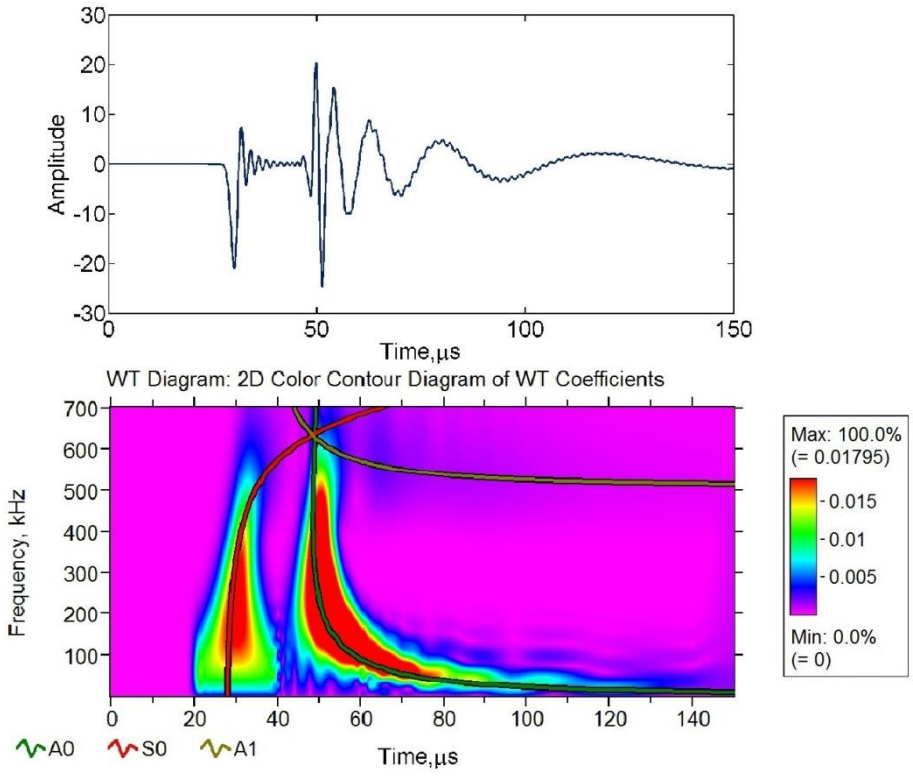

Figure 4.12. AE waveform and its wavelet in aluminum.

The waveforms from the aluminum model displayed a dispersion behavior quite in agreement with aluminum dispersion curves available in literature (Rose, 2004). The curved lines on the wavelet represent the respective symmetric and antisymmetric modes of wave propagation. In the plot, the displacement/strain pattern was of interest and assignment of interest and assignment of specific quantity has been omitted from the time domain waveform both here and in a similar plot shown later for the CFRP models.

For CFRP panels, however, the method was slightly modified. The application of pulse load on the numerical model gave rise to additional oscillation components. The presence of such components affected the features of symmetric and antisymmetric modes, which are the principal focus of this study. Hence, to remove these oscillation components, the numerical model was modified by appending a "dummy" isotropic material having modulus of elasticity the same as the stiffness along the principal direction of the CFRPs. The pulse type load was applied on the isotropic segment of the model and this enabled to propagate a wave displacement pattern consisting primarily of symmetric and antisymmetric parts.

Simulations were done on 2D plane strain model, which was assumed to represent the wave propagation along one of the principal stiffness direction for the panels. The length of the model, both in the CFRP and isotropic part was maintained long enough to avoid reflections from either edge. The lamina material properties used for both panel A and panel C in the models are listed in Table 4.1 (Barbero, 2008). In the simulations, the average laminate properties were used in the models. The shell element size used for the 2D simulations was 0.5 by 0.5 mm. The element size was chosen based on literature (Moser et al., 1999; Rose, 2004) The velocity of wave propagation from the experiments (CFRP dispersion curves in section 3.5) and the numerical simulation were compared to verify validity of the model. LS-DYNA explicit finite

element analysis was used to determine the response of the panels to the applied the pulse type loads.

Table 4.1

Lamina Properties

E_1, Pa	E_2, Pa	E_3, Pa	G_{12}, Pa	G_{23}, Pa	G_{13}, Pa	Nu_{12}	Nu_{23}	Nu_{13}
133.86e9	7.706e9	7.706e9	4.306e9	2.76e9	4.306e9	0.301	0.396	0.301

The pulse was applied at a location such that the symmetric and antisymmetric parts were clearly separated before hitting the composite part. The modes which were generated this way continued to propagate on the composite part with the antisymmetric mode showing significant deviation in wave velocity as compared to the isotropic part. This method enabled the elimination of the higher oscillation components noted when the pulse was applied directly on the CFRP model.

Responses of the models to the applied pulse type loads depend particularly on the shape and pulse width. In these simulations, as mentioned earlier, triangular pulse load of 1μs width was used. The small pulse width applied here enabled generation of waveforms with frequency components in hundreds of kilohertz's which are typical of AE signals. The triangular shape gave rise to signals with frequency component over a wide range. Figure 8 shows a waveform and its wavelet obtained at distance of 50 mm from the interface between the isotropic segment and the CFRP part.

It can be seen that the generated waveform consisted of waveforms with symmetric and antisymmetric modes of wave propagation. During the analysis, the symmetric (first strong pulse) and antisymmetric (second strong pulse) parts of the waveforms were identified using the

method discussed earlier. The frequency range for each component was mostly between 100 to 400 kHz. The symmetric components had a slightly higher frequency range.

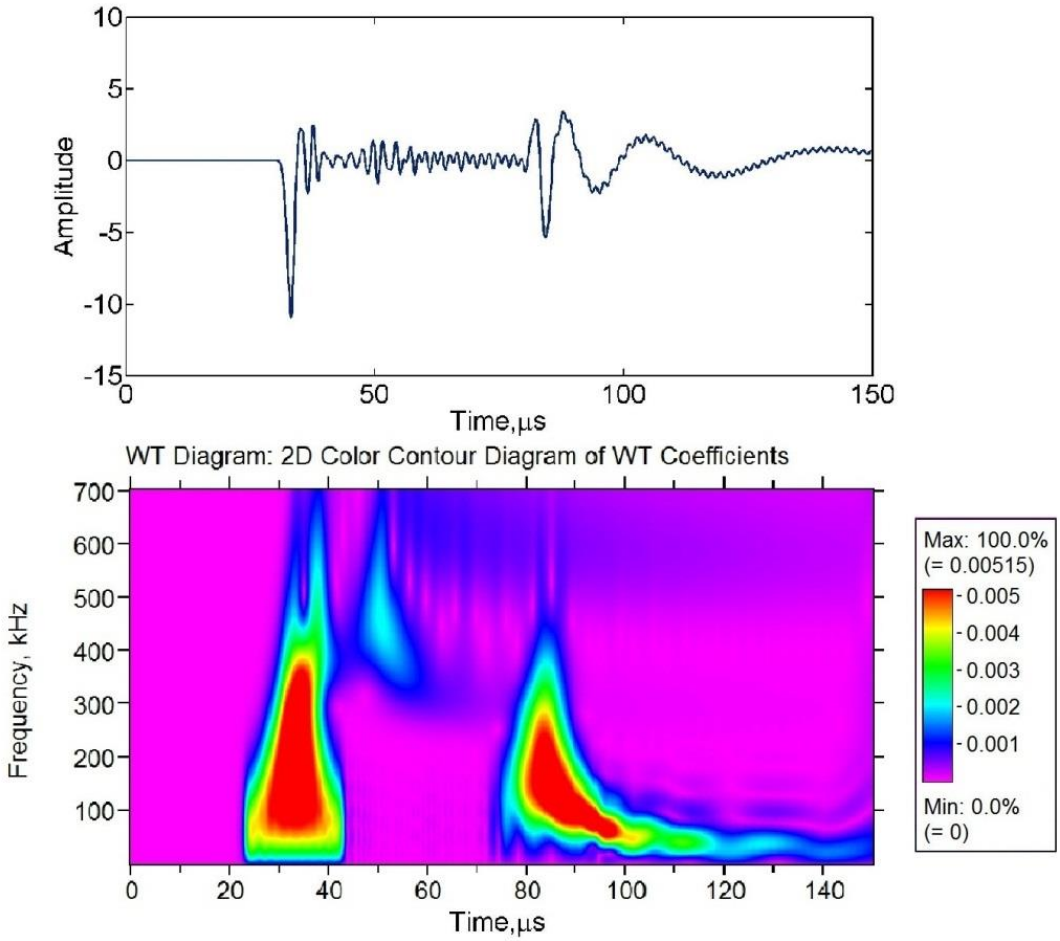

Figure 4.13. AE waveform and its wavelet in CFRP panel.

The waveforms were filtered to avoid low frequency components i.e, below 100 kHz which practically are not picked by solid piezoelectric sensors. The dispersion behaviors of the generated waveforms were compared with those obtained experimentally and happened to be in good agreement. For wide frequency range, between 100 kHz and 500 kHz, the wave velocity for S_o and A_o modes in quasi-isotropic panels were found to be about 5.7 and 1.5 km/s respectively. The velocities in the crossply laminates were slightly higher with 6 and 1.65 km/s respectively for the two modes.

4.5 Effect of Material Absorption in the Acoustic Emission Waveforms

4.5.1 So and Ao mode attenuation. The attenuation coefficients determined experimentally revealed that the symmetric and antisymmetric modes behave differently. On the other side, AE events occur as combination of symmetric and antisymmetric modes. The numerically simulated waveforms were free of any material damping influence. Also, as the simulations were 2D along the wave propagation direction, the geometric spreading had no influence on the signals. Thus, the only factor which is expected to affect the waveforms along the wave propagation direction is dispersion which occurs due to the presence of multiple frequency components.

In this and later sections, how material absorption progressively affects the signals with the distance of propagation is quantitatively detailed. The attenuation coefficients obtained from the experiments were applied to the numerical waveforms to incorporate the effect of material absorption. Several waveforms at different distances were taken to see how the material absorption effect goes with distance. The effect, at first, is seen separately on the two modes, i. e. the symmetric and antisymmetric modes. The combined effect on the acoustic emission event is considered later. The symmetric and antisymmetric modes from the event, as discussed earlier, were separated and conditioned using bandpass 100-500 kHz Chebyshev type II filter to filter frequency components outside this range using MATLAB.

The method used here considers the frequency range for the waveforms. The acoustic emission event simulated consisted of frequency components over a wide range. The FFT's (Fast Fourier Transforms) for the waveforms were obtained. The amplitude of the discrete frequency component was multiplied by the attenuation coefficient obtained from experiments for that specific frequency component. The attenuated signal waveforms, hence, were obtained through

inverse transform of the product of the attenuation coefficients and the FFT amplitudes. This approach was applied to the A_o and S_o modes separately since the range of attenuation values for these two modes are different.

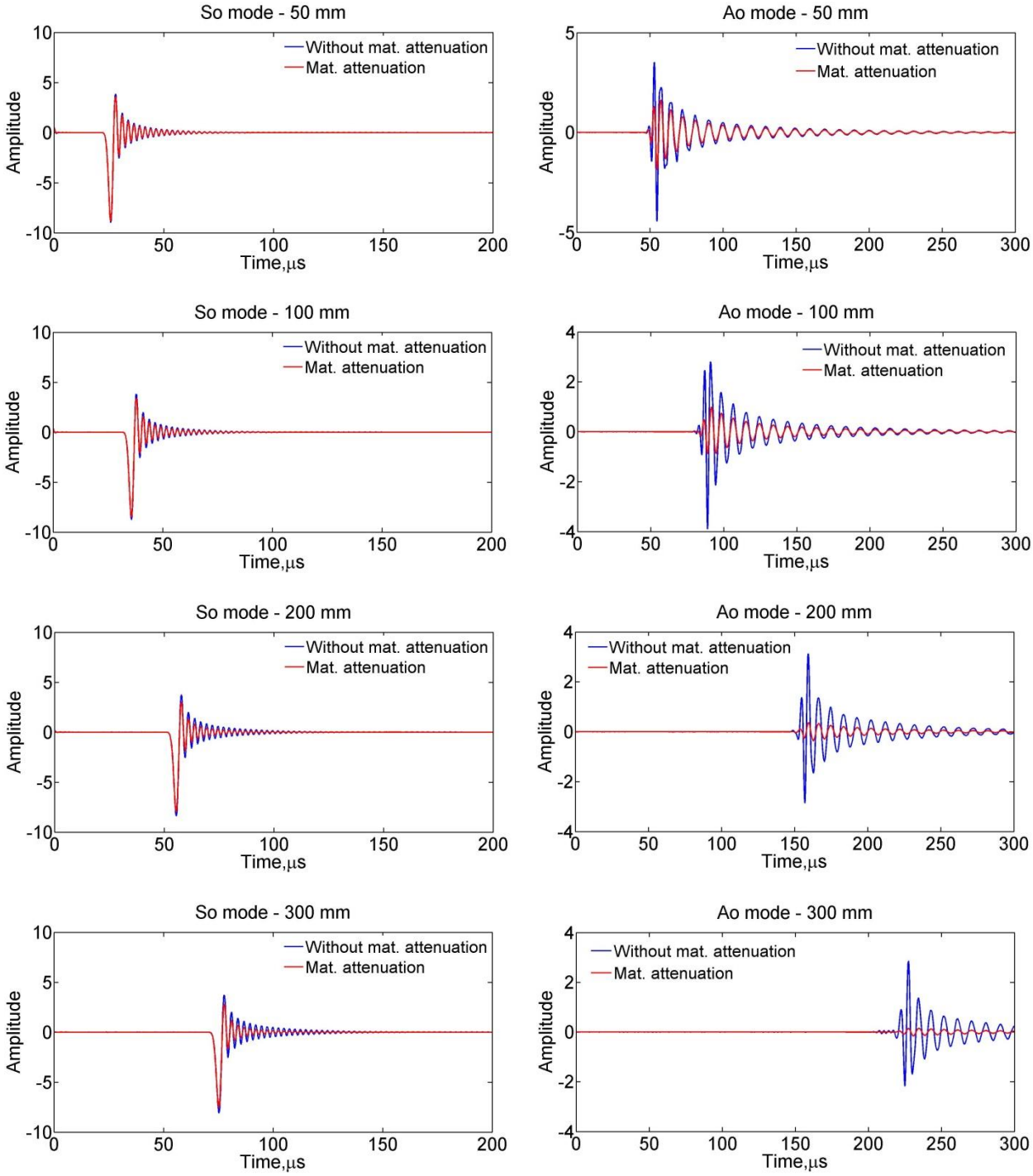

Figure 4.14. Amplitude reduction with and without material absorption.

Figure 4.14 shows S_o and A_o waveforms obtained from the numerical simulations, free of material absorption in combination with waveforms obtained by superposing the effect of material attenuation. The waveforms were taken at different distances from the source stretching up to distance of 250 mm. The waveforms shown here were obtained from the quasi-isotropic panel simulation results. The outcomes were shown to have the same tendency in C-ply laminates.

It is quite evident that the effect of material attenuation is more severe in the A_o modes. Even under the condition which is free of material absorption, the reduction in amplitude for A_o modes is higher than S_o modes. Figure 4.15 (blue curve), shows the reduction in amplitude from the numerical simulations. In the figure, it is shown that the reduction in amplitude for S_o modes was about 8% after 250 mm distance of propagation while it was about 50 % reduction in amplitude for A_o modes. As mentioned earlier, since the only cause of reduction in amplitude reduction in the numerical simulations is dispersion, it is evident that the A_o modes are more dispersive than the S_o modes.

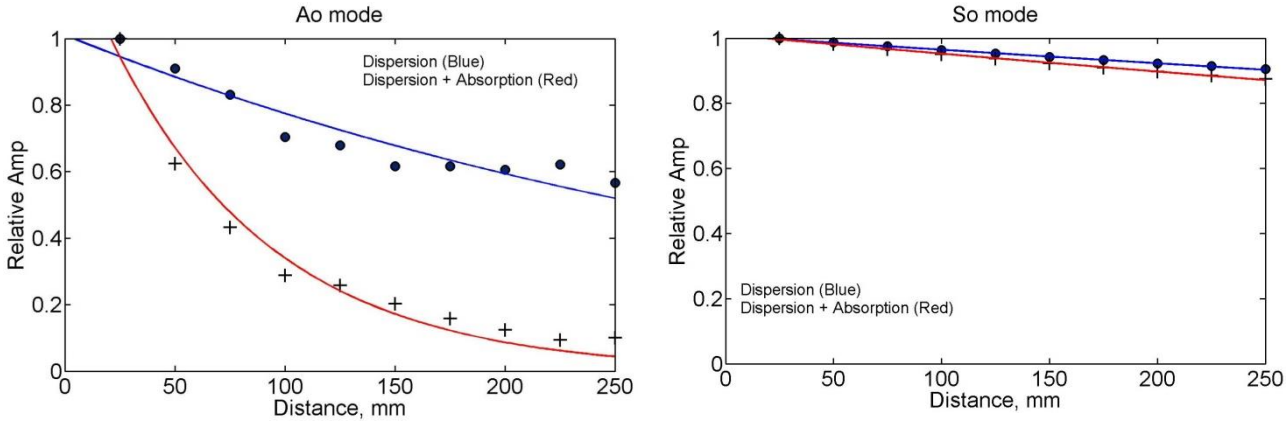

Figure 4.15. Amplitude reduction in A_o and S_o modes.

When the attenuation coefficients were imposed on the S_o modes, the waveform characteristics exhibited minimal changes. The envelope enclosing the mode waveforms was shown to vary slightly. Figure 4.15 shows that under the effect of material attenuation, the

amplitude of the S_o modes, even after propagation of 250 mm, was reduced by an additional 4% to the reduction which was caused by dispersion.

This makes the total reduction of amplitude due to dispersion and material attenuation to 12% after 250 mm distance of propagation. The effect of both dispersion and attenuation was different in the case of antisymmetric modes. Figure 4.14 shows the waveform shapes, and hence the envelopes enclosing the waveforms changed over distance. The accompanying reduction in peak amplitude was very high as compared to S_o modes. Within a distance of 100 mm, material attenuation, combined with dispersion had decreased the peak amplitude by about 70%.

The results displayed in Figures 4.14 and 4.15 indicate that the effect of both dispersion and material attenuation had more severe effect in the A_o modes. Numerical simulations on the CFRP panels were done to determine the influence of the mechanical properties on the wave propagation characteristics. The in-plane principal stiffness ($E_{1,}$ and E_2) of the panels were shown to affect the nature of S_o mode propagation. On the other hand, the shear stiffness (modulus, G_{12}) properties were shown to affect the nature of A_o mode propagation. Particularly, the group velocity and dispersion in the waveforms were very sensitive to the fluctuation in these stiffness values. Taking into account the constituent materials of the CFRP panels, the fibers provide higher in-plane stiffness. This enabled the S_o mode propagation to advance over a longer distance. On the other hand, the viscoelastic matrix material provides weak shear stiffness and is characterized by lower G_{12} values. Comparison of the material properties of aluminum with average laminate principal stiffness of the crossply laminates indicates the in-plane stiffness was equivalent to the modulus of elasticity of aluminum. The shear modulus, however, was only about 20% of aluminum that makes the panels far less stiff for propagation of flexural type modes. Similar comparison with quasi-isotropic panels indicates the average in-plane principal

stiffness was about 80 % of that of aluminum. The viscoelastic properties of the matrix as well as the least stiffness could contribute to the higher level of dispersion and material absorption shown in the case of A_o modes.

4.5.2 Geometric Spreading. Two important causes of attenuation have been considered so far: material absorption and dispersion. The third most important factor is geometric spreading. This is caused by energy redistribution which takes place during wave propagation in planar structures. The simulations discussed earlier were 2D plain strain models for the panels. Hence, the effect of geometric spreading was omitted as the wavefront was considered to traverse along the principal stiffness direction alone. On the other hand, when dealing with wave propagation in plates, the pattern of propagation is such that the wavefront tends to propagate circumferentially outward from the source. This has significant effect when recording waveforms along some direction. The amplitude reduction is mode independent and is affected by the distance from the source.

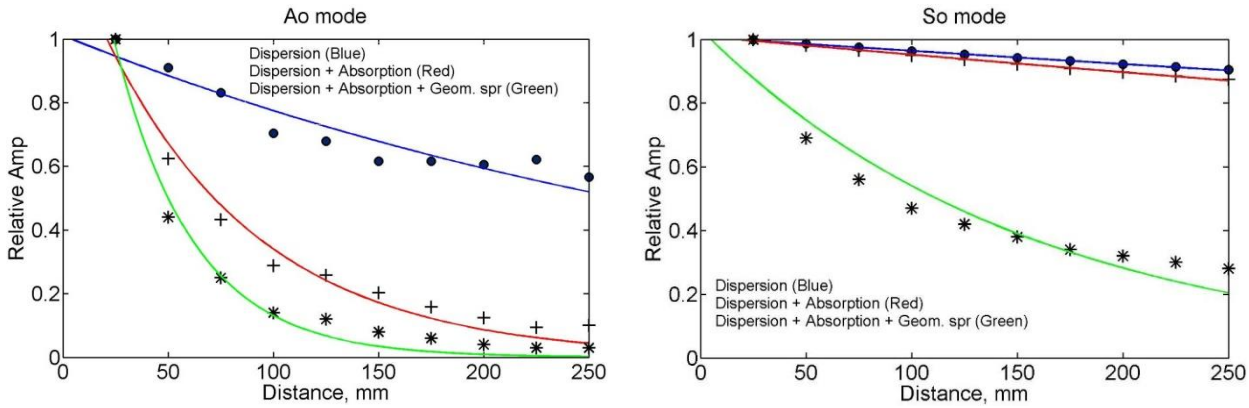

Figure 4.16. Amplitude reduction due to geometric spreading, absorption and dispersion.

Figure 4.16 shows the amplitude reduction obtained when the effect of geometric spreading was imposed on to the waveforms. Here it should be noted that, the frequencies at which peak amplitudes of the waveforms could shift. The wavelets for the consecutive waveforms from the numerical simulations indicated the frequencies at which peak coefficients

obtained shifted, however, by small margins. When calculating the effect of geometric spreading, it was assumed that the peak amplitudes were peaked at a specific central average frequency. It is evident that the geometric spreading has a more severe effect on S_o mode than the effect noticed due to material attenuation and dispersion. The combined effect of dispersion and material attenuation was 12% reduction in peak amplitude for distance of propagation equal to 225 mm. However, the reduction in amplitude grew to 70 % when the geometric spreading effect was included. This makes geometric spreading as the major factor contributing to amplitude reduction of S_o modes in the CFRP panels.

In the A_o modes also, the influence of geometric spreading was quiet significant. However, the combined effect of dispersion and material attenuation was the major contributing factor to decrease he amplitude. For example, after propagation distance of 100 mm, as shown in the figures, the peak amplitude had reduction of 70% due to dispersion and material attenuation. However, this reduction grew to 85% with inclusion of the effect of material spreading. This indicates combination of material absorption and dispersion had more influence. Also, over a distance of 100 mm, the A_o modes had reduction of amplitude by 70 % within 65 mm distance of propagation, while it took over 225 mm for S_o modes to experience reduction by the same percentage.

4.5.3 AE event consisting of the fundamental modes. The earlier subsections discussed attenuation with reference to the fundamental symmetric and antisymmetric modes of wave propagation. Also, the influence of the different mechanisms of attenuation on these modes is also discussed. An acoustic emission event, in actual conditions occurs as combination of the fundamental and higher order modes of wave propagation. All the attenuation mechanisms discussed here also affect the acoustic emission wave propagation.

An important feature used in AE analysis is energy of the signal waveforms. In the earlier discussions, it was mentioned that the amplitude and frequency features of the signal waveforms were affected by the different attenuation mechanisms. In Figure 4.17,the energy of waveforms taken at intervals of 25 mm are plotted as function of signals. The waveforms were separated to their constituent A_o and S_o modes and the values were summed to obtain the energy of the simulated AE event. Energy of the signals were calculated according to the following equation. However, the threshold level, which sets the integration limits, is neglected in these calculations. Nonetheless, reasonable approximations of signal energy were obtained.

$$E = \int_{t_1}^{t_2} f_+^2(t)dt - \int_{t_1}^{t_2} f_-^2(t)dt \tag{6.1}$$

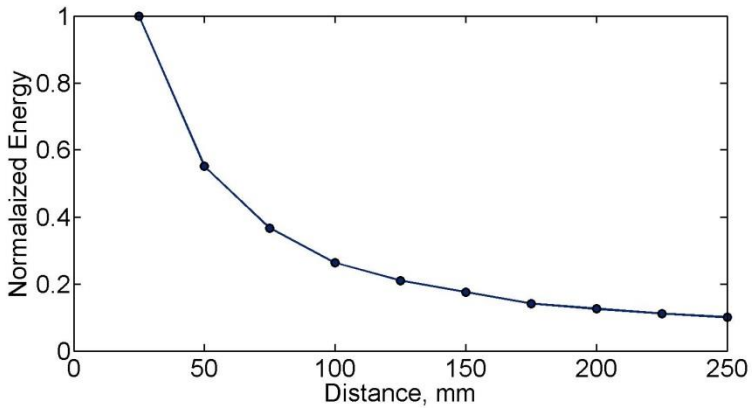

Figure 4.17. Energy of AE signals with distance.

It can be seen that there is a reduction in energy of the waveforms modes by about 80% and more within a distance of 100mm and will be more with further increase in distance. This reduction in energy will have significant impact in the interpretation and analysis of waveforms obtained from an acoustic emission event. The same tendency is expected to be shown in other parameters used in acoustic emission analysis. This indicates the need to pay much consideration to the inclusion of attenuation in acoustic emission analysis.

4.6 Summary

In this part of the research, the influence of attenuation on acoustic emission signals, their constituent wave propagation modes and features of their waveforms was analyzed. Two representative laminates of crossply and quasi-isotropic layup were used for experiments. The panels were excited by Gaussian type pulses at different frequencies. The response of the laminates were measured along different directions and distances.

The attenuation coefficients obtained from the experiments indicated that the fundamental modes of wave propagation had varying attenuation levels. The antisymmetric wave propagation modes in the signals had attenuation levels, which were three to four times that of the symmetric modes. The distance of propagation for the symmetric modes, because of less attenuation levels, was about three times that of antisymmetric modes.

The two laminates exhibited different amplitude distribution with direction. The quasi-isotropic laminates had in plane isotropy and because of which amplitudes measured at different directions, for both symmetric and antisymmetric modes were, for similar input amplitude and frequency, were of equivalent magnitude. However, the amplitudes of the signals measured along the non-principal directions were much smaller than the amplitudes from the principal directions.

Examination of the influence of the different attenuation mechanisms indicated that significant reduction in amplitude of S_o modes resulted from geometric spreading. The other attenuation mechanisms such as dispersion and material attenuation had comparable effect on the antisymmetric modes. The antisymmetric modes were also found to be more dispersive than their symmetric counterparts were.

The last section of the chapter discussed one of the most important features of AE signals, i.e energy of the signals. It was found to change much with reasonably short distance of propagation. Several sources in the literature are available which make use of energy and other features. However, the effect of attenuation with distance or sensor location is missing in the analyses. This affects the accuracy of results from analyses of AE data. Analyses of data from acoustic emission tests should, therefore, include attenuation effects.

CHAPTER 5

Delamination Tests

5.1 Introduction

Damage progression during delamination is examined experimentally in this chapter. Carbon Fiber Reinforced Polymer (CFRP) double cantilever beams (DCB) were used to simulate delamination and the acoustic emission events generated in the process were analyzed. In Chapter 2, it was discussed that the different failure mechanisms affect the stiffness and strength of a structure in different ways. Signatures from acoustic emission signals could be used to identify these failure mechanisms. In addition, in previous studies, the fracture toughness or delamination resistance of the laminates was shown to vary with different parameters such as the rate of loading or, in this case, the rate at which crack tip opening displacement occurs (Corigliano et al., 2006; Corigliano & Ricci, 2001). The resistance is also affected by fiber orientation of the laminae bounding the delamination. (Johnson et al., 1989). These factors determine the nature of the damage that evolves in the structure. In addition, it is expected that the acoustic emission signatures from delaminations will be affected by these factors.

The objectives of this part of the research are to monitor the acoustic emission activity during initiation and growth of delamination in the CFRP specimens and distinguish the different failure mechanisms occurring within the delamination process using the acoustic emission data. Scanning Electron Microscopy (SEM) images were also used for identifying the failure mechanisms. Influence of loading rate and the lamina orientations on acoustic emission signals and fracture surface morphology are examined in detail. Details of the tests and analyses are presented in the following sections.

5.2 Test Specimens and Test Procedure

Two types of DCB test specimens were cut from an orthotropic laminate (panel A) and a quasiisotropic laminate (panel C), described in Chapter 2. The dimensions for the specimens were in accordance with the D5528 ASTM test standard for mode I delamination. The beams were cut from the edge of the panels which was provided with a thin insert film that extended up to length of 55 mm from the edge. The thin film serves the purpose of initiating delamination during loading of the specimens. Ten specimens were cut from each panel. Five of the specimens are shown in Figure 5.2. Each arm of the beams was transversely loaded in tension by means of a hinge bonded at one edge. The respective dimensions of the test specimens are shown in Figure 5.1.

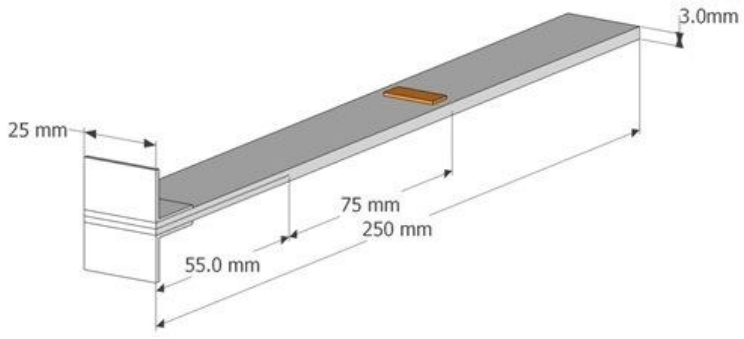

Figure 5.1. Dimensions of delamination test specimens.

PZT sensors were bonded to the specimens at distance of 75 mm from the tip of the film insert. As mentioned in the earlier chapter, the amplitude of the antisymmetric mode of a wave propagating in these CFRP specimens reduces significantly over short distances. The delamination in these tests was made to grow up to 50 mm. Thus, with the selected location of the sensor, the distance between the crack front and the sensor reduces from 75 mm to 25 mm when the crack growth reaches 50 mm. This enables collection of AE signals without losing much of the antisymmetric components.

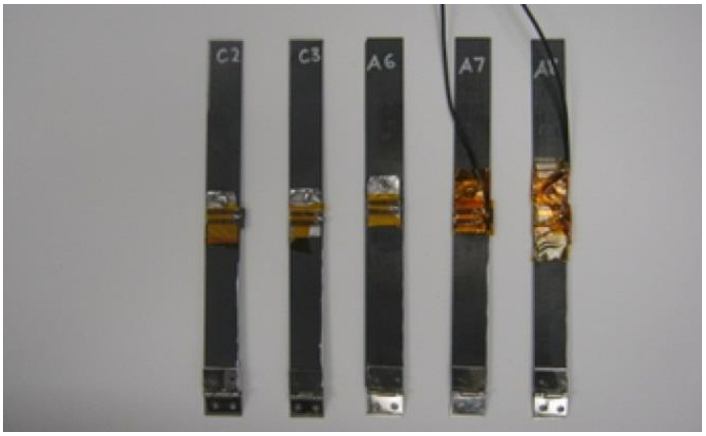

Figure 5.2. Delamination test specimens.

The tests were done under displacement-control. As listed in Table 5.1, individual specimens were tested at different displacement rates applied at the hinges that include 0.5, 2, 5, 10 mm/min. Acoustic emission signals, the applied opening displacement, and the transverse load applied to the specimens were continuously recorded by the acoustic emission data acquisition system while the delamination grew by 50 mm.

Table 5.1

Displacement rates for delamination tests

Delamination tests					
Cross-Ply			Quasi-Static		
Test No	Specimen	Displacement	Test No	Specimen	Displacement
1	A1	10 mm/min	6	C1	10 mm/min
2	A2	5 mm/min	7	C2	5 mm/min
3	A3	5 mm/min	8	C3	5 mm/min
4	A4	2 mm/min	9	C4	2 mm/min
5	A5	2 mm/min	10	C5	2 mm/min
11	A6	0.5 mm/min	12	C6	0.5 mm/min

The acoustic emission signals and their features were recorded during the tests by a PCI-2 data acquisition system. The signals were preamplified at 40 dB gain before acquisition, and the threshold for avoiding noise signals was set at 35 dB. Each AE waveform was recorded for a duration of 1 ms with a sampling rate of $5X10^6$ samples per second. In addition, the edges of the specimens were painted white and inscribed with marker for monitoring the position of the crack tip. Videos of the delamination growth were recorded for tests A1, A2, A4, A6, C1, C2, C4 and C6. The displacement and time readings from these videos were used to plot the delamination growth with time.

5.3 Data Analysis

5.3.1 Damage progression. The initial delamination due to the film insert in the crossply specimens was between two 90 degree laminae while in the quasi-isotropic specimens, it was between two 0 degree laminae. Hence, the delamination crack front was parallel to the fiber direction in crossply specimens and perpendicular to fiber direction in quasi-isotropic specimens. The effect of this fiber orientation on the delamination growth direction is shown in the snapshots of videos for the two types of laminates, Figure 5.3. The snapshots were taken from specimens A2 and C2.

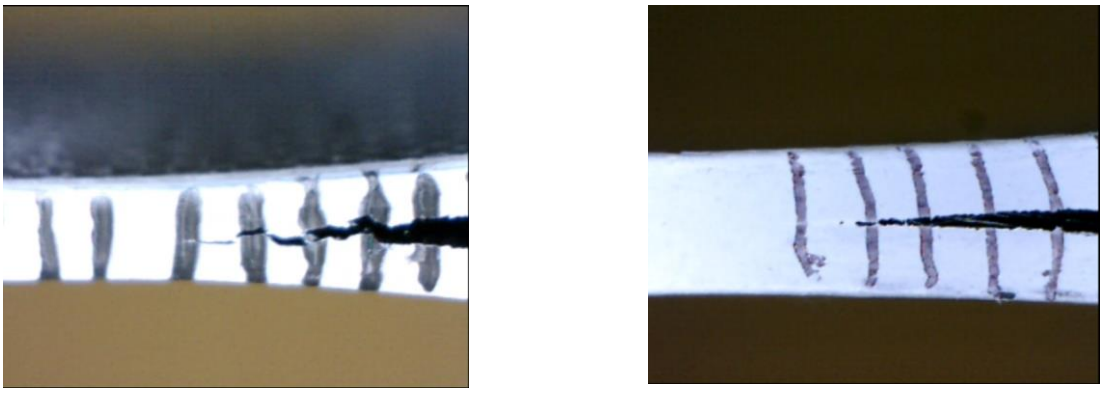

(a) (b)

Figure 5.3. Delamination trajectory (a) Crossply (b) Quasi-isotropic.

As can be seen in the figures, a planar delamination growth is seen in the quasi-isotropic specimens. The crossply specimens, however, exhibited delamination growth that had an uneven fracture profile in which the delamination appeared to wander through the thickness of the 90 degree laminae. The crack growth displacement for the crossply specimen is shown in Figure 5.4. As these delaminations grow, the different damage mechanisms including matrix cracking, fiber break and debonding accumulate and interact with each other. In the case of the quasi-isotropic laminates, the delamination front is forced to propagate nearly along the interface between the adjacent 0 degree laminae by the resistance offered by the fibers. However, in the case of the cross-ply laminates, the matrix crack could propagate both parallel and transverse to the delamination growth. Thus, the interface at which delamination advances could jump from one lamina to the next due to cracking in the resin material. Figure 5.3 (a) shows the resulting zigzag path of the interlaminar. In the quasi-isotropic tests, as the fibers are aligned along the delamination growth direction, bridging caused by the fibers between two adjacent plies is also possible.

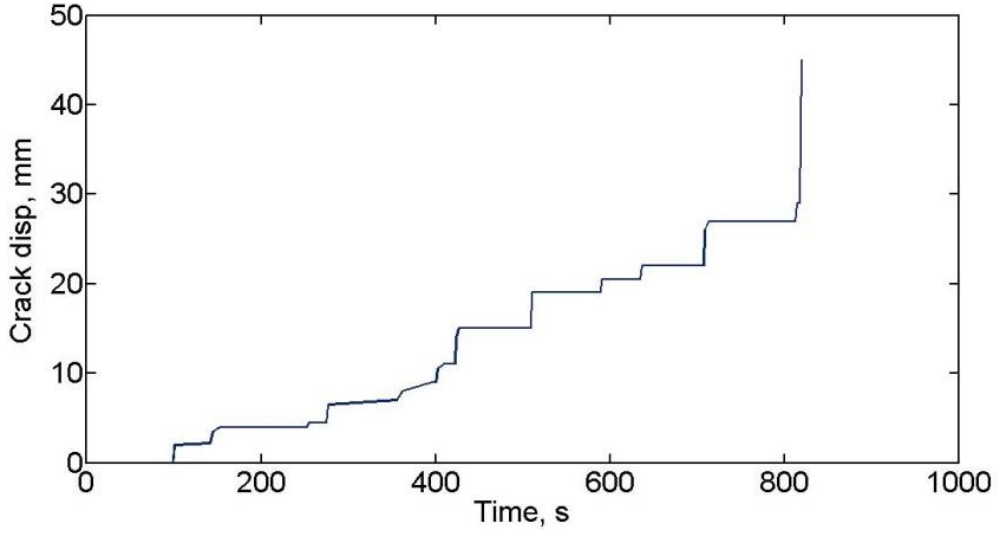

Figure 5.4. Delamination growth with time for test A2.

5.3.2 Delaminations and AE bahavior. When the DCB specimens were gradually loaded under displacement control, there was short delay before the delamination started propagating from the tip of the film insert. This start of propagation was marked by a simultaneous increase in the AE events. For delamination growth by 50 mm, cumulative event counts in the order of tens of thousands were obtained. In some cases, 500 signals, on average, were recorded for a delamination growth of 1 mm. This confirms acoustic emission as a useful means to detect onset and growth of delamination in CFRP structures. The cumulative occurrence of events was, however, dependent on different parameters, as explained in later sections. Several features of these events were recorded, which eventually are used for analysis in identifying the different damage mechanisms involved.

Occurrence of the different damage mechanisms in the specimens was verified with the help of SEM images. Several images of the fracture surfaces, from both the quasi-isotropic and crossply laminates, and from the tests under different loading rates were taken. The images of the fracture surfaces were taken at a magnification of 500X. Figure 5.5 shows an SEM image of a quasi-isotropic specimen fracture surface. Three major failure mechanisms were identified from the images. These are matrix crack, fiber breakage, and debonding at the fiber-matrix interface. Presence of voids, which were displayed in the thermal images of the laminates, shown in figure 3.1, was also noted. In addition, the images revealed the uneven fracture growth in the crossply specimens, which rather have occurred in steps. Each of these damage modes have been source of AE signals, and the thousands of AE events revealed the occurrence of the modes in the thousands during the delamination growth. Despite the density of the damage mechanisms on a unit area varied from one area to another, the presence of the mechanisms in higher numbers was supportive of generation of the thousands of AE events.

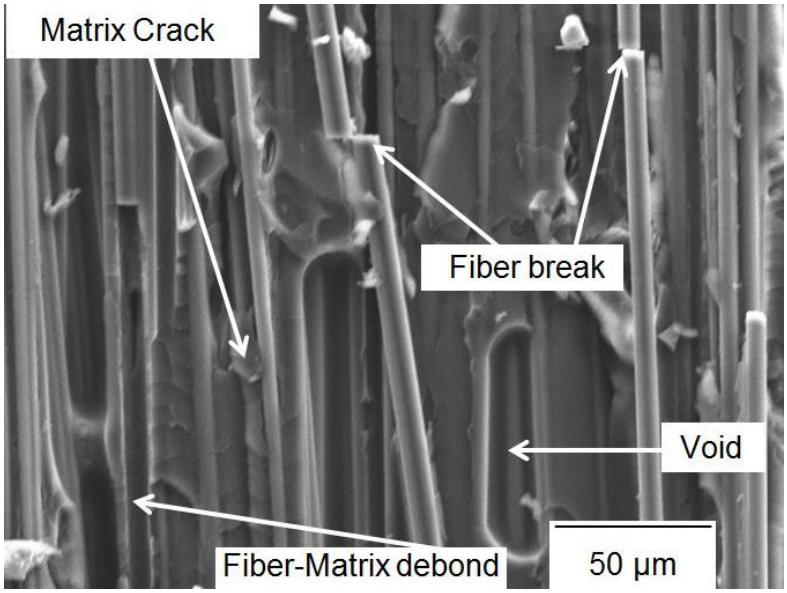

Figure 5.5. SEM image of quasi-isotropic specimen fracture at 500X magnification.

5.3.3 Delamination growth rate and AE behavior. The rate of delamination growth determined the fracture surface morphology as well as the acoustic emission signals. In this section, we examine how the acoustic emission data changed in response.Load-displacement curves such as the one in Figure 5.6 were generated for each test. Displacement, here, refers to the opening displacement applied at the hinges. The points at which the load-displacement curves deviate from linearity were visually compared to assess the resistance to delamination initiation from the insert tip (ASTM D5528). The range of velocities used here was narrow, in contrast to those considered in (Corigliano & Ricci, 2001), so that the delamination resistance of the laminates has hardly changed with the opening rates. However, delamination resistance of the crossply specimens was higher than that of the quasi-isotropic specimens. The load level required to initiate delamination (deviation from linearity) from the crack (insert film), was, on average, 16 N for the quasi-isotropic specimens and 30 N for the crossply specimens. It was noted that, the load-displacement drops after initiation of delamination in the quasi-isotropic

specimens, while it the curve went up with further growth of the delamination length in crossply laminates.

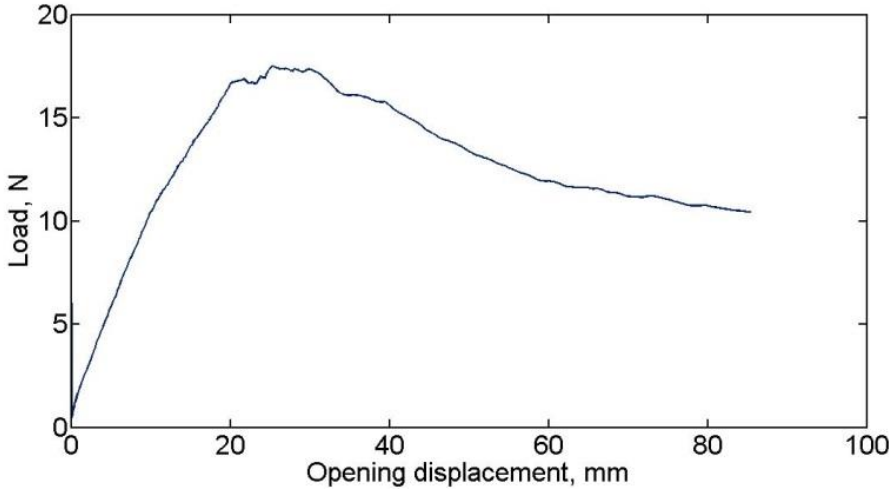

Figure 5.6. Load-diaplacement curve for test C2.

Despite the insignificant differences in the fracture toughness behavior, some features of the signals were sensitive to the rate of delamination growth. The Amplitude density distribution, i.e, the distribution of the number of events having a specified range of amplitude with a unit time was indicative of how damage accumulation and interaction varied depending on the rate of delamination growth. Figure 5.7 shows the amplitude density plots for the quasi-isotropic laminate at opening rates of 5 mm/min, 2 mm/min, and 0.5 mm/min. Depending on the displacement rates used, the number of AE events generated were different. To facilitate processing of the waveforms afterwards with a limited number of events, the acquisition data files were split into two or more files. Thus, ordinate scales of the plots shown in the figures were accordingly different. In addition, the plots shown in Figures 5.7 (b) and (c) are generated from files that contained waveforms after delamination has already started to grow unlike Figure 5(a) which included the waveforms from the initiation of delamination. Thus, the initial faint region in Figure 5.7 (a) before time of 200 μs is not shown in Figures 5.7 (b) and (c).

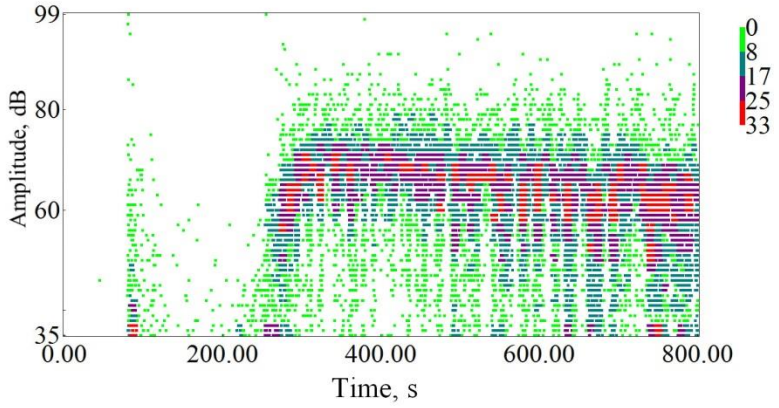

(a)

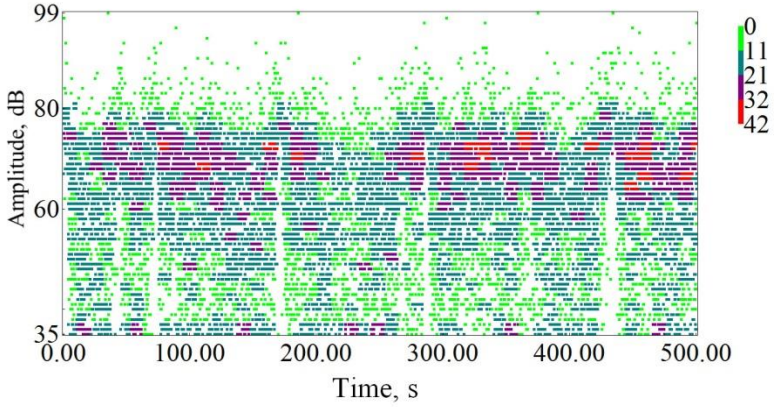

(b)

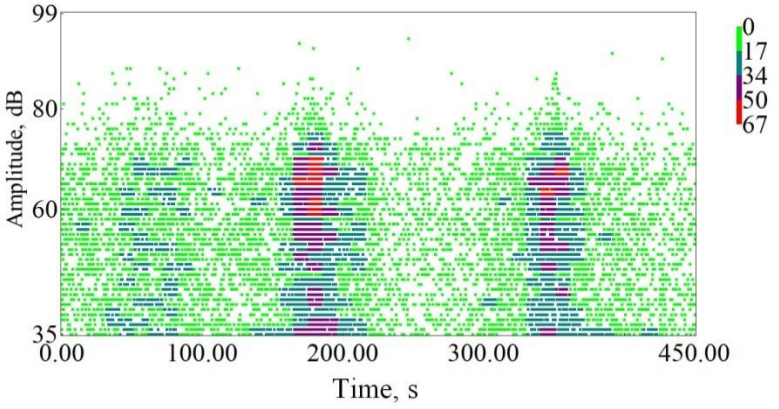

(c)

Figure 5.7. Amplitude density plots for quasi-isotropic specimens (a) 5 mm/min (b) 2 mm/min (c) 0.5 mm/min.

The figures indicate that, distinct amplitude density plots were obtained corresponding to each displacement rate. When the rate is 5 mm/min, figure 5.7 (a), the density plot indicates that events with amplitude in the range 60 to 75 dB occur in large numbers as compared to events in lower amplitude range. A similar tendency is shown for the test at 2 mm/min, Figure 5.7 (b). However, events with amplitude range 35 – 60 dB have higher presence in comparison with the previous case. In the third case, Figure 5.7(c), peak densities are shown in intermittent fashion unlike the previous two cases. The range of events from 35 to 70 dB shows peak densities, however, occurring at intervals, instead of the continuous high amplitude and high density fashion exhibited in the earlier two cases. Scatter plots of the amplitudes of these events were also indicative of these variations.

In the case of quasi-isotropic specimens, faster displacement rates, 10 mm/min and 5 mm/min, resulted in higher amplitude AE events at a steady rate, indicating that the crack growth rate was nearly constant. The slowest displacement rates resulted in smaller amplitude signals and the event rates fluctuated indicating nonuniform delamination growth rate. Intermittent emission of events in large numbers was typical behavior of damage progression in crossply specimens for which the fiber orientation was perpendicular to the direction of delamination growth. Amplitude density plots for the crossply specimens are shown in Figure 5.8. For the crossply specimen loaded at 0.5 mm/min rate, there were zones of intense AE activity separated by intervals of markedly lower AE activity. As the loading rate increased, the duration of the lower activity decreased and at the loading rate of 10 mm/min, the rate of AE activity exhibited a nearly uniform behavior. At loading rate of 10 mm/min, both the crossply and the quasi-isotropic specimens exhibited uniform generation of events. However, the amplitude distribution shown by amplitude density was different.

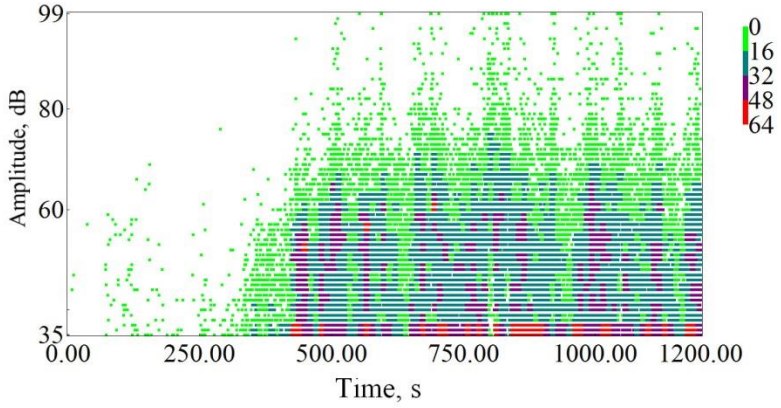

(a)

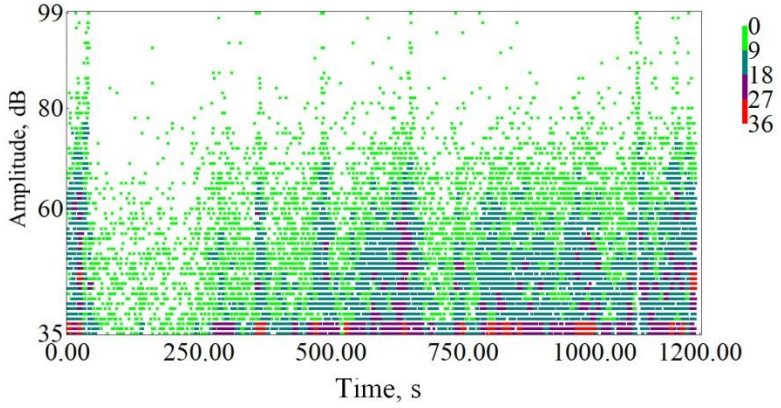

(b)

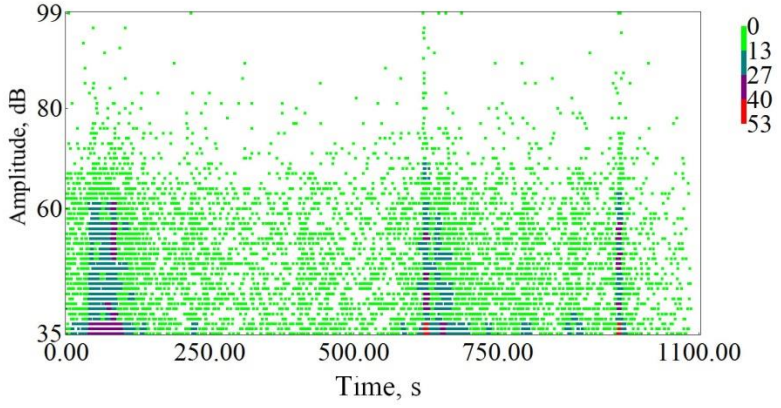

(c)

Figure 5.8. Amplitude density plots for crossply specimens (a) 5 mm/min (b) 2 mm/min (c) 0.5 mm/min.

In addition to amplitude, other features of the signals were examined to reveal the changes in acoustic emission behavior due to variations in the crack growth rates. Feature selection was made based on an examination of the scatter and cumulative distributions of the recorded AE features. In Figures 5.9 and 5.10, the energy of the AE signals is shown for two of the tests.

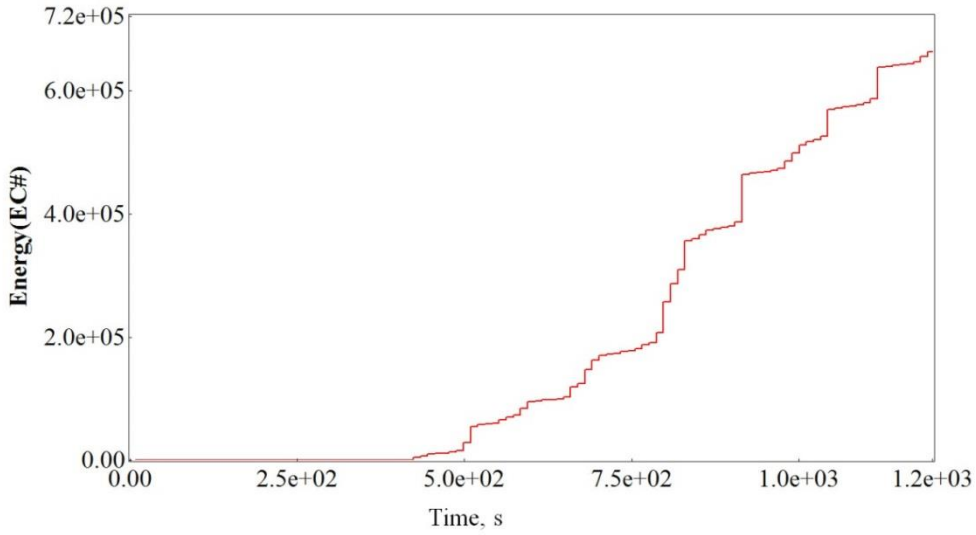

(a)

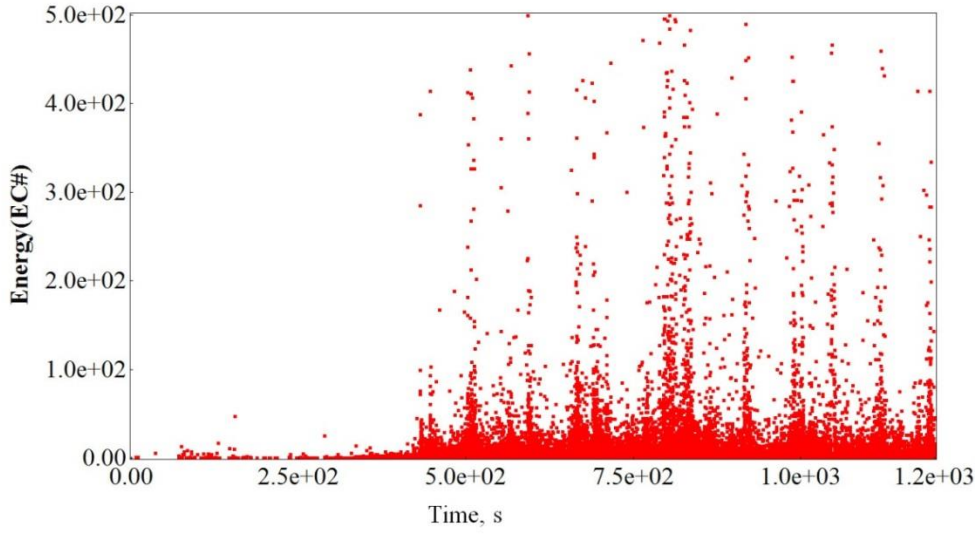

(b)

Figure 5.9. Energy of AE signals from test A1 (a) scatter plot (b) cumulative distribution.

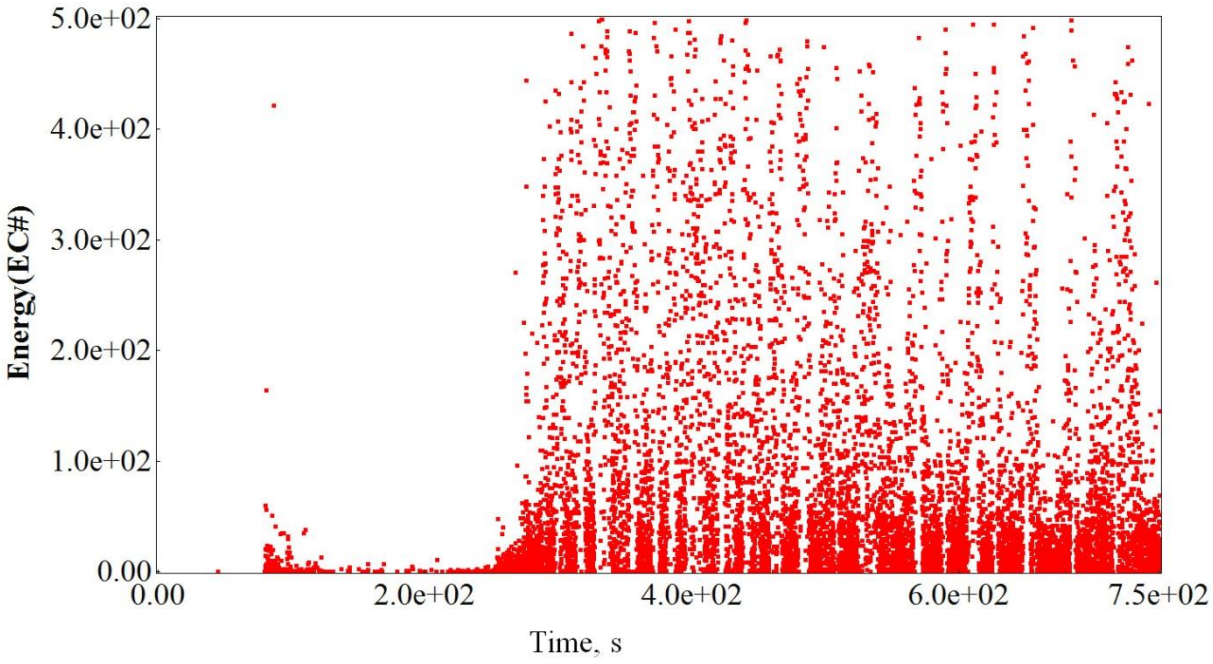

(a)

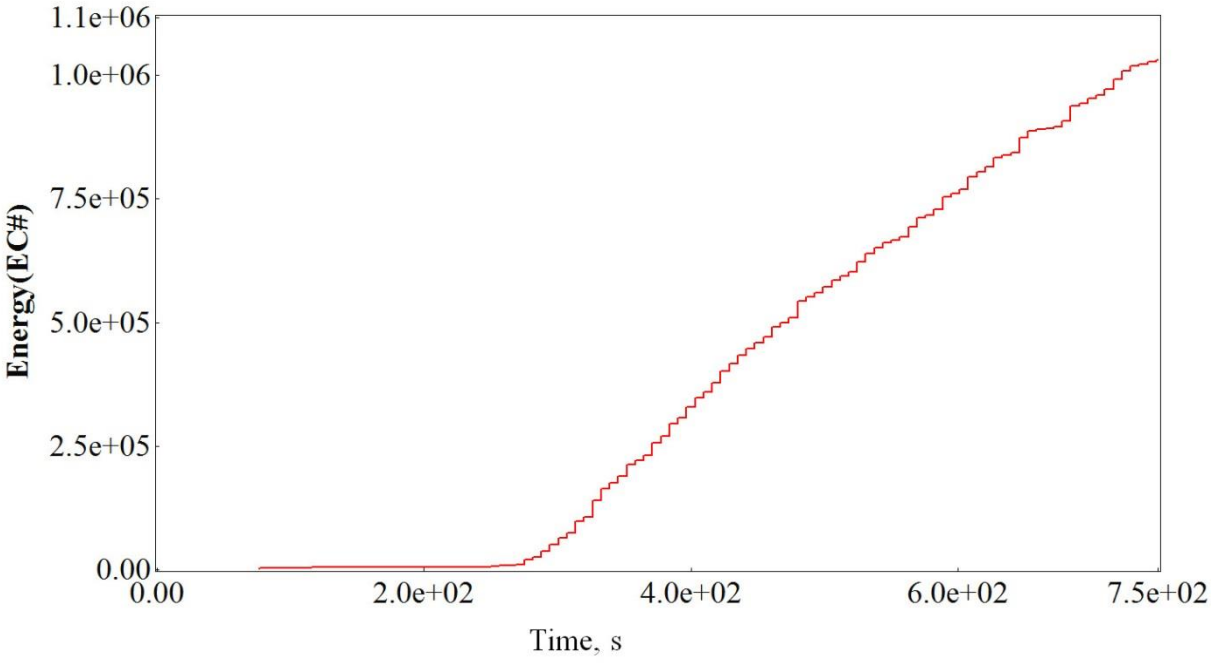

(b)

Figure 5.10. Energy of AE signals from test C1 (a) scatter plot (b) cumulative distribution.

Scatter plots of energy in Figures 5.9(a) and 5.10 (a) shows discrete segments of events on the time scale. However, the size of the intervals between the segments in the case of quasi-isotrpic specimen is much smaller than in the case of the crossply specimen. This is also confirmed by the cumulative distribution of events, Figures 5.9(b) and 5.10 (b). In the quasi-isotropic specimen, the curve increases steadily with the increase in delamination length or time. This indicates the increment in the cumulative energy caused by a new event or by a group of events at an instant of time is bound by values that maintain the uniform slope of the curve. However, in the crossply specimens, abrupt increments in the cumulative plot were seen. Unlike the case of quasi-isotropic specimens, a group of events at some instant or over a narrow interval of time had relatively higher energy which adds significantly to the cummulative plot. This causes a jump in the cumulative plot curve causing a shift in the slope. A similar description holds true for the duration of the signals.

5.4 Evolution of Damage Mechanisms with Delamination Growth Rate

The observations from the density, scatter and cumulative plots of the acoustic emission signal features are indicative of variations in the damage accumulation and interaction among the different cases considered. The abrupt increase in the cumulative energy and duration of events for crossply specimens shows the release of higher energy in the delamination area which results in longer duration events. The region between the abrupt changes indicates a stable release of energy or increment of delamiantion growth. In this section, the failure mechanisms involved and their impact on the damage progression have been examined. Multiple SEM images of the fracture surfaces of the specimens, both crossply and quasi-isotropic were taken.The SEM images were used to correlate the different failure mechanisms with the acoustic emission patterns displayed in Figures 5.7 through 5.10.

In the amplitude density plots, it was shown that, for test C2, the amplitude density in the amplitude range 65 – 75 dB was stronger and the amplitude density for the same amplitude range was weaker with decrease in the opening rates. SEM images of the fracture surfaces were taken for tests C2 and C6 which were tests corresponding to opening rates of 5 mm/sec and 0.5 mm/sec. Images were taken at equal intervals of 1 mm from the insert film tip where delamination started to grow. Figure 5.11 shows some of the images taken for both types specimen.

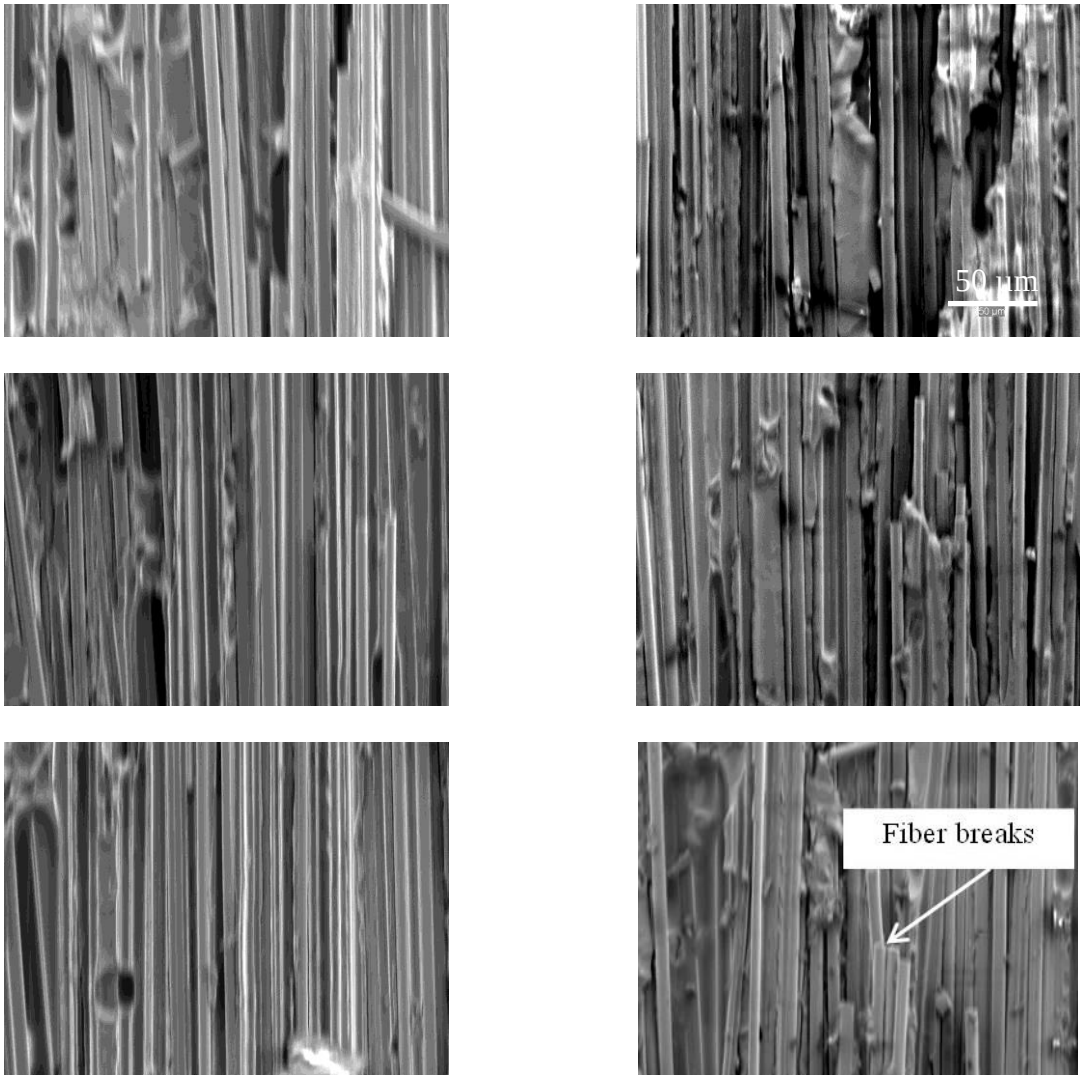

Figure 5.11. SEM images of fracture surface from specimens C2 (left) and C6 (right) at 500X.

The images revealed that three types of damage mechanisms were noticed along the entire scan area covered. The relative composition of the damage mechanisms, however, varied from one scan area to another. Matrix cracking and debonding between the fiber and the resin material were very prevalent over the fracture surfaces. This has been true with the fracture surfaces of both specimens C2 and C6. However, the distribution of one type of damage mechanism, i.e, fiber fracture, was different for the two cases. The images revealed that, the fracture surfaces of specimen C2 had more density of fiber fracture, which occurred either individually or in a group. While there were hardly any visible fiber cracks in the Figure 5.11(left), in the figure to the right, noticeable number of fiber cracks were visible. In the images compared for this, a larger number of fiber breaks were observed in the case of specimen C2. It was found from the amplitude density plots that, events with amplitude above 60 dB were dominantly present for specimen C2. Correlation of these two findings indicates that, the fiber fractures made a significant contribution to the strength of the amplitude density over the specified range. Also, the SEM images from the whole range of scan areas indicated the presence of matrix cracking and debonding between the fibers and the matrix material. For all amplitude density plots, events in the amplitude range less than 60 dB had a strong presence. These signals were, thus, correlated with resin cracking and failure of the bond between the fibers and the matrix material.

As part of this research, a series of tensile tests were done on specimens of similar size. It was found that, when the tensile specimens are subject to quasi-static type of load, at the beginning, consistent with the discussion of chapter two, the matrix cracking events were very dominant. However, an eventual shift was noticed in the concentration of events. As the damage progresses further, more number of fiber fracture events were recorded. The amplitude range for

these series of events was examined and found to be consistent with the amplitude distribution of Figures 5.7 and 5.8.

The delamination growth for the crossply specimens was characterized by abrupt changes of the delamination profile. The cumulative energy and duration plots confirmed these were zones where high energy and high duration events were generated. A series of images taken near such zones revealed that breaking of fiber bundles occurs with the release of massive energy resulting in high energy and longer duration events, as seen in Figure 5.12. Thus, the fiber breaks, under the settings used for data acquisition appeared to be the driving mechanisms for the emission of high amplitude and high energy events. Also, they occur in large numbers when the opening rates are higher. A shift or jumping of fracture propagation from one interface to another or one ply to another was also shown in the same image.

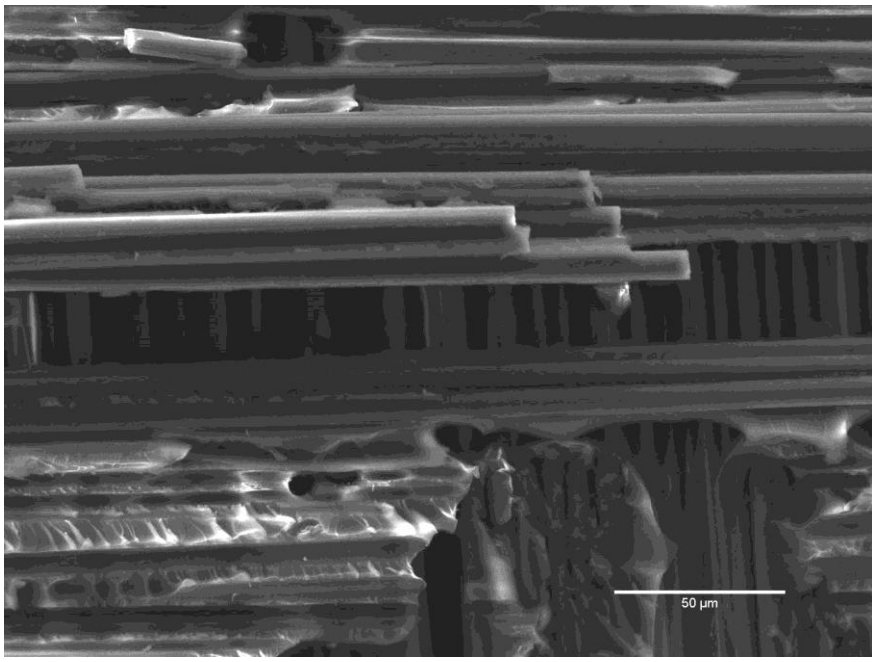

Figure 5.12. SEM image of fracture surfaces from specimen A5 (500X).

In the cumulative and scatter energy plots, the majority of events were shown to be of lower energy. The SEM images show contours on the resin material that are indicative of the

formation of new crack surfaces due to successive incremental failure. These events occur in quiet large numbers and the images depict such contours in several parts. Thus, the lower energy events were associated with matrix cracking. The remaining events were associated with debonding which occurs at fiber-matrix interface.

5.5 AE in Crossply vs Quasi-isotropic laminates

The acoustic emission behavior in the two types of laminates differed largely due to the difference in the fiber orientation at the delamination interface. The fracture toughness or delamination resistance of the crossply laminates was larger than that of quasi-isotropic laminates. Because of a higher resistance to delamination, the crossply tests took nearly double the time that was required for the quasi-isotropic specimens to achieve a delamination length of 50 mm. Under the settings used for the acquisition, however, the cumulative number of events has not shown much variation. The amplitude distribution for each of the tests indicated that, the peak values of the amplitude density were equivalent among tests under similar loading rates. The pattern of displacement and the pattern of damage accumulation in response to the different opening rates were, however, different. As discussed in section 5.2, the fracture propagation exhibited a steady growth in the quasi-isotropic specimens while the progress was uneven in the case of the cross ply specimens. Related to this; the acoustic emission plots in the earlier section indicated that, due to the contrast in the fiber orientation with respect to the delamination growth direction in the two types of specimens, the pattern with which events occurred in the two laminates varied. In the pattern of amplitude density distribution, it was learned that high amplitude signals were coming in large numbers continuously particularly at higher opening rates for the quasi-isotropic laminates which, otherwise exhibited an intermittent occurrence of events which happens at certain intervals in the crossply laminates.

5.6 Numerical Simulation of Failure Modes in Composites

5.6.1 Geometry and material properties. In the earlier chapter, acoustic emission events consisting of symmetric and antisymmetric modes of wave propagation were numerically simulated. A similar method of simulating AE events was used here to simulate transverse matrix cracking and interlaminar separations between plies. The focus of this chapter has been to see how acoustic emission waveform features change depending on the rate at which damage advances. Energy release during an acoustic emission event in the previous chapter was mimicked by pulse type loads applied to the numerical model. A numerical study (Rajendra et al., 2011) based on this idea has shown that the width of the pulse type load has strong influence on the features of the resulting waveforms. The frequency feature, in particular, was highly sensitive to the pulse width. Two values for the pulse width were used for the simulation of the interlaminar separation discussed in the following subsections. The material properties used here are similar to those used in the previous chapter. Quasi-isotropic laminate with slightly different layup from the one used in the experiments was modeled in the simulations. The geometry of the model used for the simulations is shown in figure 5.13.

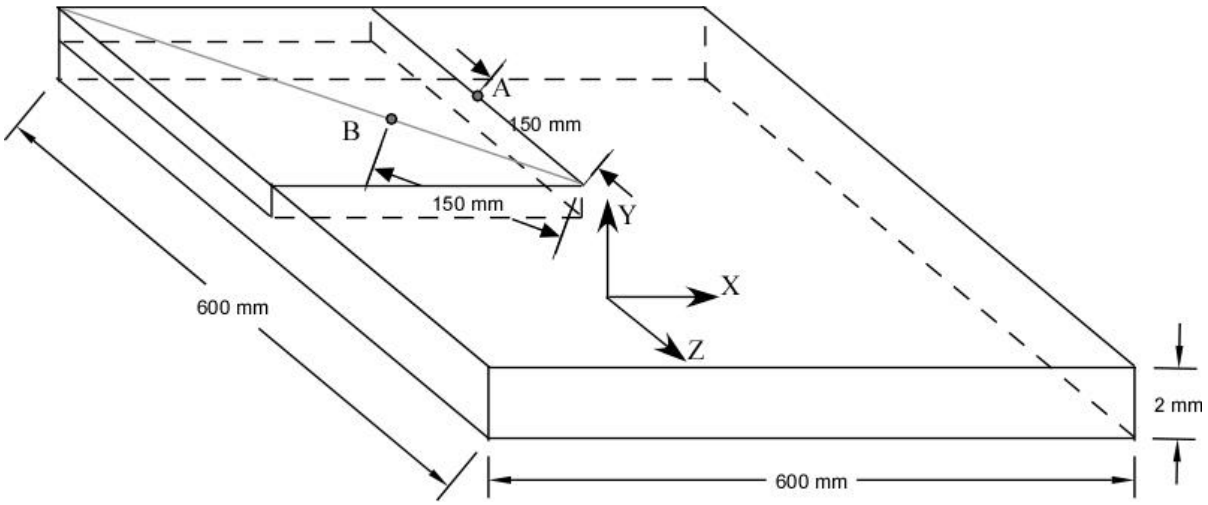

Figure 5.13. Geometry of FE model.

5.6.2 Transverse matrix cracking. A 5 mm long transverse crack is assumed to propagate at the center of the laminate and is assumed to be confined to the middle of two laminae with fibers orientated along the 0 degree direction. Since these two laminae are symmetrically located with respect to the neutral axis, the center of the transverse crack coincides with the neutral axis of the laminate. Acoustic emission generated by this transverse crack propagation was simulated with a series of 25 impulses applied sequentially to consecutive nodes 0.2 mm apart along the path of the transverse crack. The shape of each impulse is set such that effectively a constant amplitude impulse travels both in time and space without amplitude fluctuations to represent a crack that propagates with uniform velocity. Figures 5.14 and 5.15 show snapshots of the 3D and 2D animation, respectively, of the y-strain (in-plane strain) animation from the simulations.

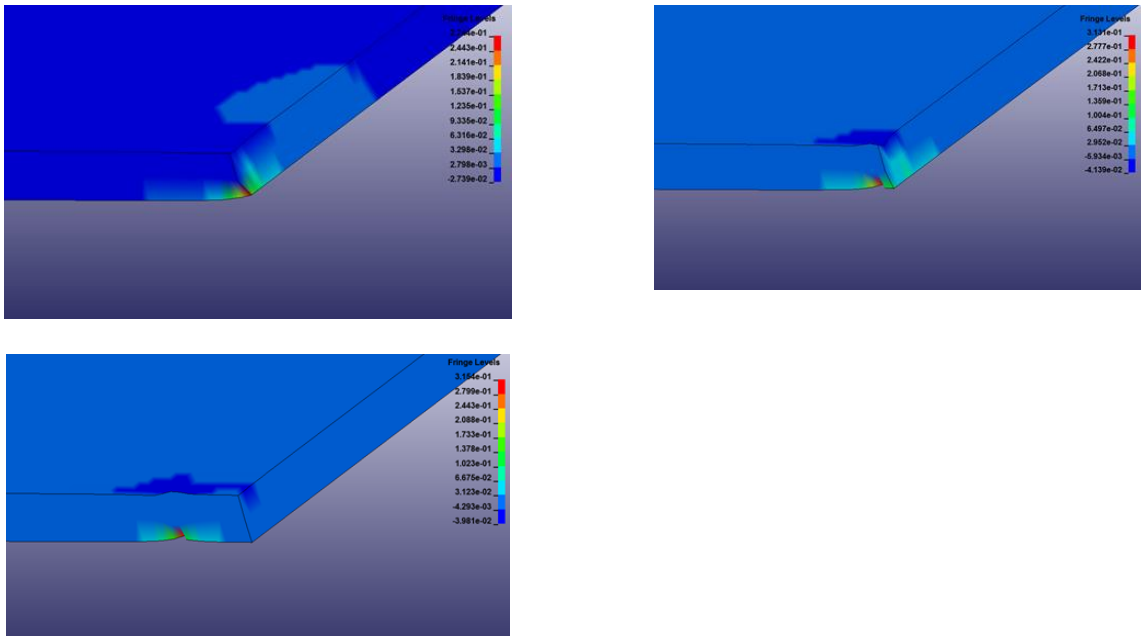

Figure 5.14. Snapshots of 3D animation of y-strain in matrix cracking.

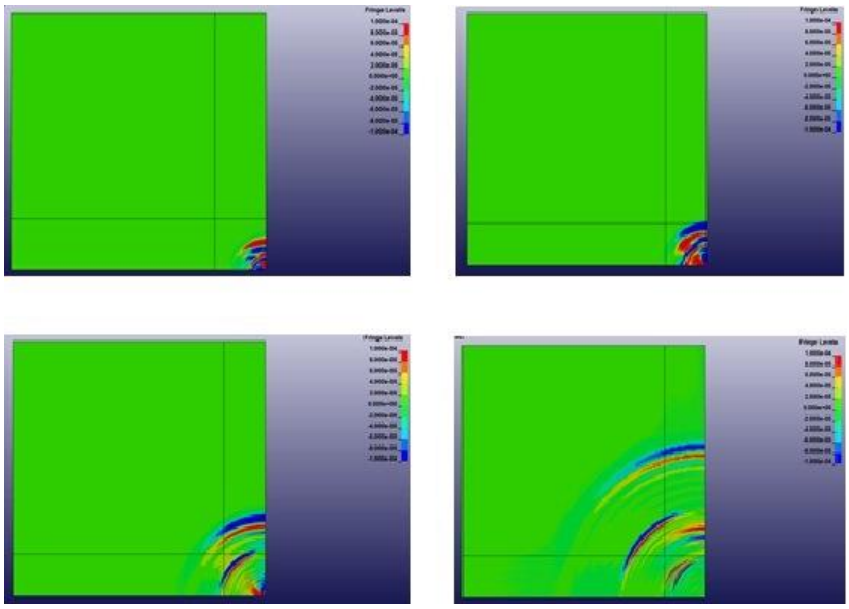

Figure 5.15. Snapshots of 2D animation of y-strain in matrix cracking.

5.6.3 Mode I interlaminar fracture. Mode I delaminations are assumed to result in excitations normal to the plane of the laminate but acting on the surfaces of the participating laminae. As in the case of transverse crack propagation within a lamina, delaminations were simulated as a series of seventeen impulses, each with a width of 2 μs. Figures 5.16 shows snapshots of the 2D animation of the y-strain (in-plane strain) from the simulations.

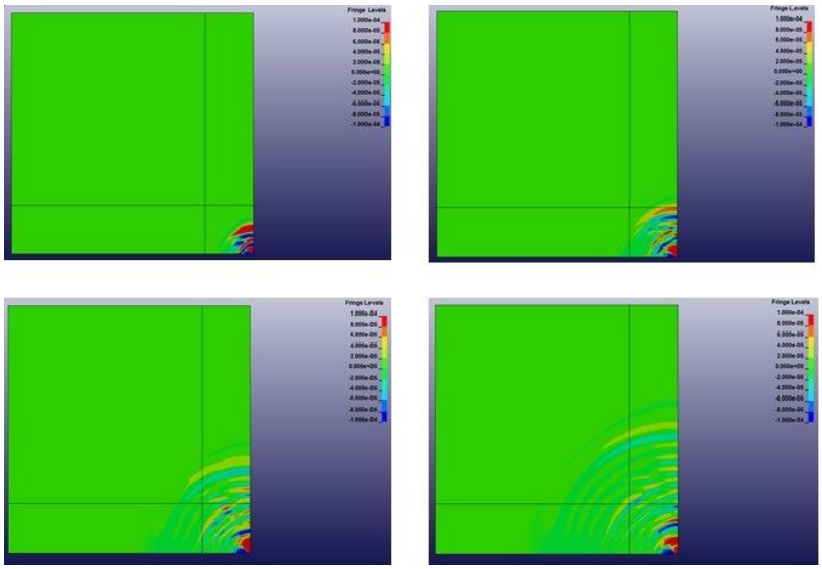

Figure 5.16. Snapshots of 2D animation of y-strain in delamination.

Two cases were considered to simulate the delaminations. The width for the pulse type loads applied on the numerical model had two values. In the first case, the pulse had width of 2 μs, while in the second case, the pulse width was reduced to 1.5 μs. The waveforms forms from each case are presented in the following section.

5.6.4. Waveforms corresponding to individual failure modes. Simulated acoustic emission waveforms corresponding to the different failure modes are shown in figure 5.17. Only the waveform shapes were considered in these simulations, without considering the amplitude of the source event or the energy released. Widely different features are seen in these figures. The basic Lamb wave modes including the S_o, A_o, and shear modes, appear to be prominent in the waveforms. Their participation in waveforms vary depending on the source event and the inclination of the propagation path to the normal to the crack plane. When the propagation path is at or close to the normal to the crack plane, S_o and A_o Lamb wave modes appear to dominate. But, when the propagation path deviates from the crack plane's normal, the shear wave mode become significant and appear to reach maximum amplitude around an inclination of 45 degrees, encircled in the figure.

The frequency content and the dispersion characteristics depend on the duration of the source event. The composition of features is recognizable within these waveforms and is useful in identifying the corresponding source mechanism. In addition, the source-to-sensor distance and the angle of incidence of the waveform with respect to the sensors vary over a large extent, and such variations are likely to introduce significant variations in the detected signal characteristics. The features from these events were used for classification of the source events in (K. Asamene, Knighton, T., Rajendra, D., Ali, B., Whitlow, T., Sundaresan, M., , 2011).

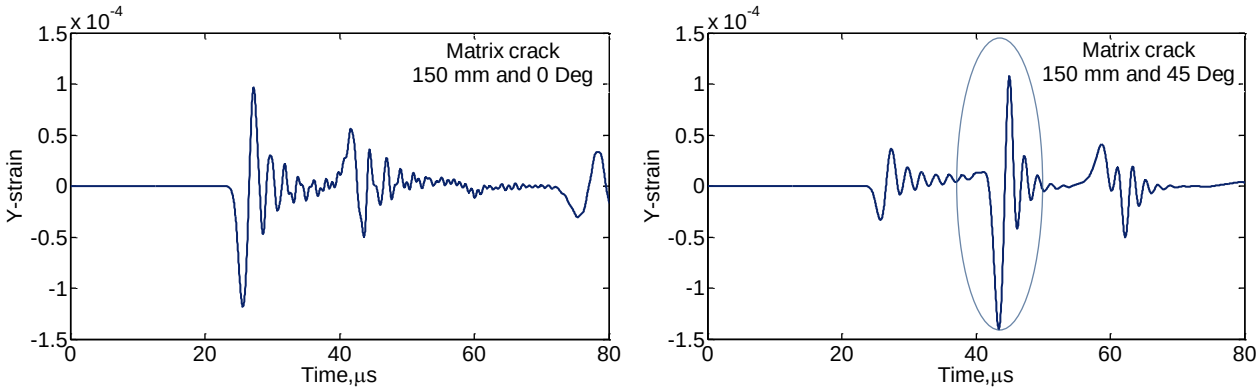

(a)

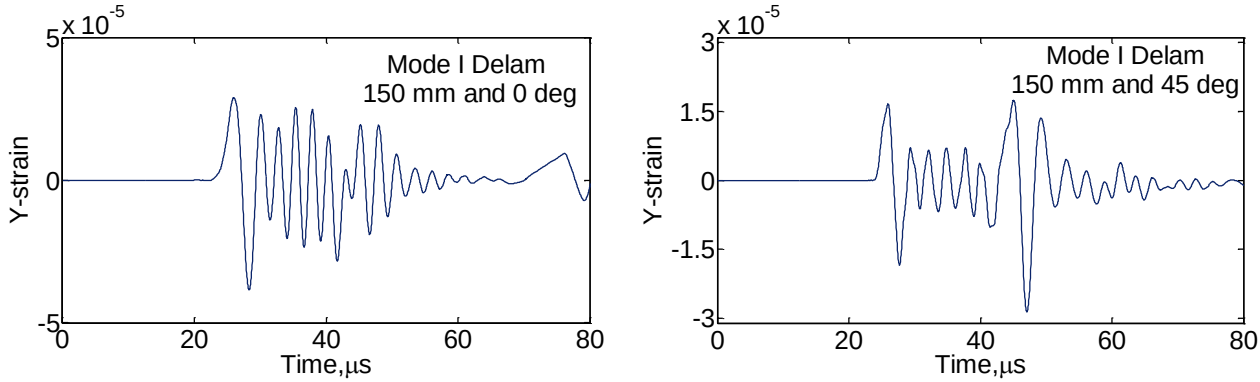

(b)

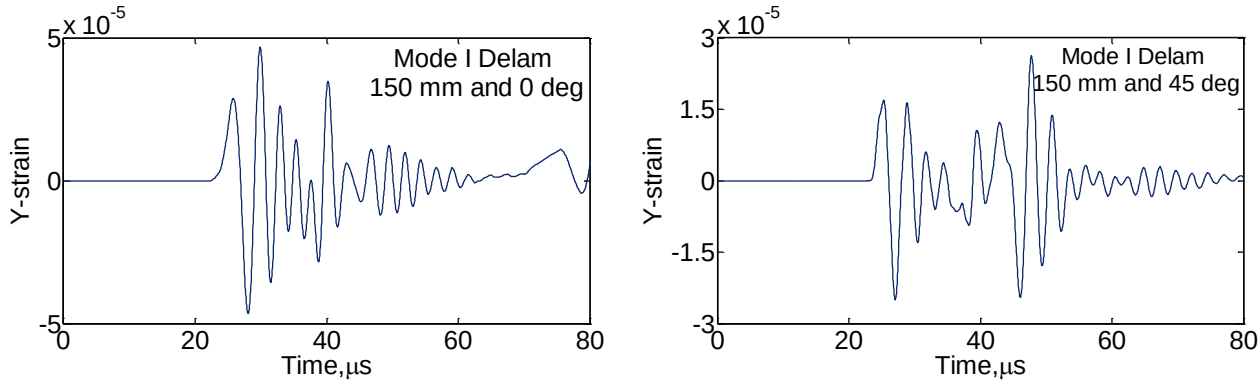

(c)

Figure 5.17. Waveforms from simulated damage modes (a) matrix cracking (b) delamination at 2 μs pulse width and (c) delamination at 1.5 μs pulse width.

It can be seen that the shear wave component, encircled in figure 5.17 (a) to the right, has a strong presence at an angle of 45 degrees. Figures 5.17 (b) and (c) show the delamination waveforms obtained under the application of pulses of different width. In these cases, the pulse width applied on the model was varied to simulate variations in the crack growth rate. Past studies at classifying the waveforms according to the source mechanisms relied on empirical features of acoustic emission signals such as amplitude, rise-time, duration, frequency content etc. It was shown in the plots that these features such as amplitude, frequency content and the duration and energy of the signals (by definition) varied significantly for the two cases. In addition, the quantity used here to display the waveform patterns is the in-plane strain. Traditional AE sensors are quite sensitive to out of plane displacements. A similar trend in the variation among the waveforms is expected in other quantities as well. These are important findings as these features of signals have been used in most of traditional AE analysis regarding source identification and pattern recognition.

(Rajendra, et al., 2011) classified acoustic emission signals in a similar fashion based on the constituent modes present in the waveforms. Thus, the relative composition of the waveforms or the relative presence of the modes in the waveforms becomes an important parameter. The numerical waveforms obtained here exhibited difference in the type and magnitude of the different modes present. The numerical waveforms from the simulation reported here are subject to further refinement. Due to the complex nature of wave propagation in anisotropic media, assumptions have been introduced that could affect the accuracy of the reported results. Nonetheless, dispersion properties of the waveforms were compared with the experimentally generated dispersion curves for the CFRP panels, (Section 3.5), and were found to be in good agreement.

5.7 Summary

In this part of the research, acoustic emission events from the growth of delamination in CFRP structures were analyzed. Delamination test specimens were prepared according to test standards and instrumented with AE sensors. Tests under different sets of parameters, viz., delamination growth rates and fiber layups were done. The AE signals and their features from the tests were recorded and evaluated. The signals were characterized with regard to damage growth rates and fiber orientation at damage growth zones. The features of the signals were also correlated with the different damage mechanisms in composites.

Some features of the acoustic emission signals were indicative of delamination growth even with a narrow margin of variation. The amplitude density was sensitive to the delamination growth rate. Cumulative and scatter energy plots were also sensitive to the rate at which damage was propagating in the laminates.

Differences in the fiber layup at the delamination growth zones were apparent. The load at which delamination initiated was nearly doubled as the fiber orientation was changed from a direction parallel to the delamination growth to a perpendicular direction. The pattern of damage progression and the associated acoustic emission were also different.

The different failure mechanisms were classified based on the AE signals and their features. Events from fiber breaks were classified into high amplitude and high energy events. Based on the distribution and cumulative presence on the SEM images and energy plots, matrix crack events were related with low energy and low amplitude signals.

Different types of wave propagation modes were identified with waveforms from numerically simulated acoustic events. The relative presence of the modes was affected by the location where the measurement was taken. Consistent with the experimental waveforms, the

features of the numerical waveforms were sensitive to the damage growth rate, which in this research was simulated by varying the width of the impulse type load applied on the numerical models.

Characterization of AE signals with regard to different parameter values at which damage could advance in a material is considered an essential step towards establishing a baseline for AE based monitoring of composite structures. Correlation of the signals with the damage mechanisms is also useful in assessing the stiffness and strength of the structures.

CHAPTER 6

Friction and Crack Growth Related Acoustic Emission Tests

6.1 Introduction

Crack growth and friction between surfaces are two of the processes in metallic materials, which give rise to acoustic emissions. In some structures such as bearings, gears, and turbine blade root joints as well as bolted and riveted joints, these processes could occur simultaneously. In such cases, it becomes important to differentiate the signals from the two sources. On the other hand, the characteristic features of acoustic emission signals generated by sliding friction between two surfaces could vary depending on the conditions prevailing at contact. Thus, this part of the research had two main objectives: to characterize friction related signals with respect to parameters of the friction process, and to differentiate characteristic features of crack and friction related acoustic emission signals. To accomplish these, a test fixture to simulate reciprocating motion between the two surfaces under controlled conditions is developed. Sliding friction under several combinations of surface roughness, relative velocity, and normal pressure was examined. Also, a steel bar was fatigue loaded under three point bending test to propagate crack growth. The acoustic emission signals generated in the process were recorded. The features of the signals were compared with those of the signals from friction. The details of each test are presented in the following sections.

6.2 Friction Test Fixture and AE Instrumentation

Figure 6.1 shows the test fixture designed for studying acoustic emission signals generated due to friction. This fixture is capable of simulating friction between surfaces under controlled conditions including normal pressure and sliding velocity. The fixture consisted of two identical friction pads pressed against the opposite surfaces of a long steel bar near its

midpoint. The relative motion between the friction pads and the steel bar could be controlled from about five microns to several millimeters.

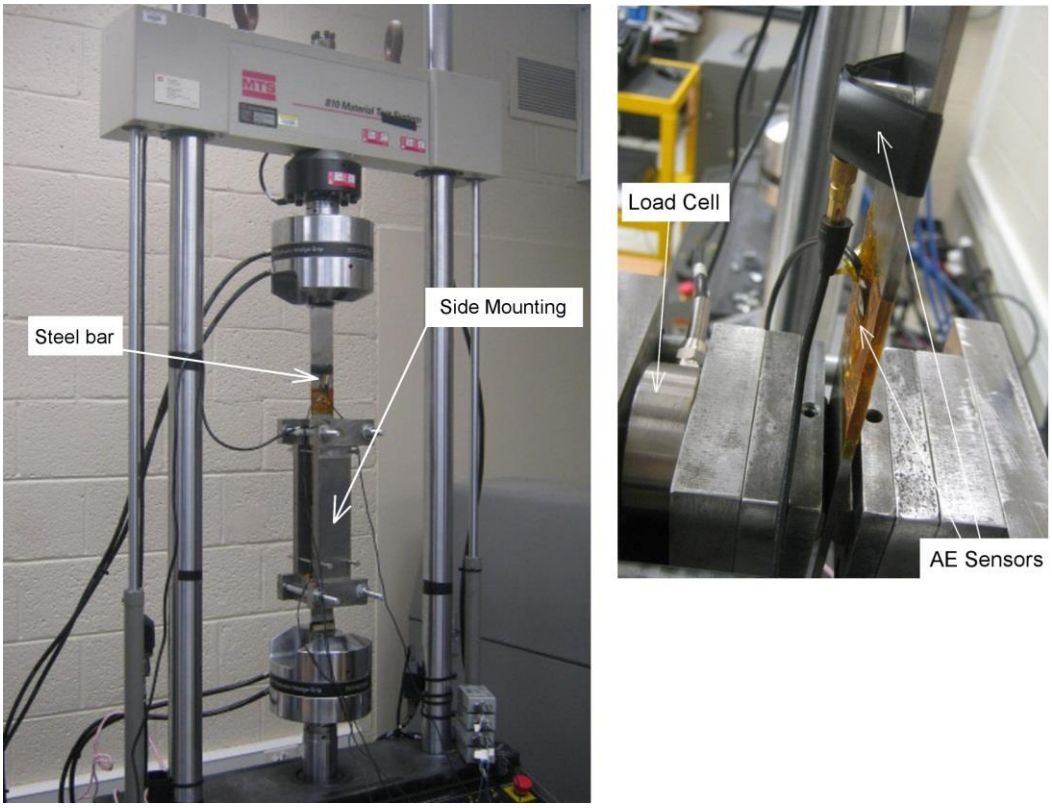

Figure 6.1. Friction test fixture.

The fixture is mounted on 810 Material Test System (Ch.3) machine and the friction pads could be subjected to either unidirectional or oscillatory motion with respect to the steel bar, as shown in Figure 6.2. The results reported in this paper were obtained while the pads were subjected to sinusoidal motion relative to the steel bar.

Cyclic loading resulted in repeated stick-slip motion between the pads and the bar. The bar's dimensions were 530 mm X 50 mm X 3 mm, as shown in Figure 6.3, and it was cut from precision ground A2 tool steel bar with surface roughness, R_{ab}, of 0.48 µm and R_{zb} of 2.76 µm. Pairs of friction pads with two different surface roughness values were used in this study. The surface roughness values, R_{ap}, of the first and second pairs were, respectively, 0.15 µm and 1.54

μm. These surface roughness measurements were taken parallel to the direction of relative sliding between the pads and the bar. The steel friction pads were 50 mm long and their contact surfaces were flat with round corners, as shown in Figure 6.4. The Rockwell hardness values for the pads and the steel bar were respectively HRB 123 and HRB 96.

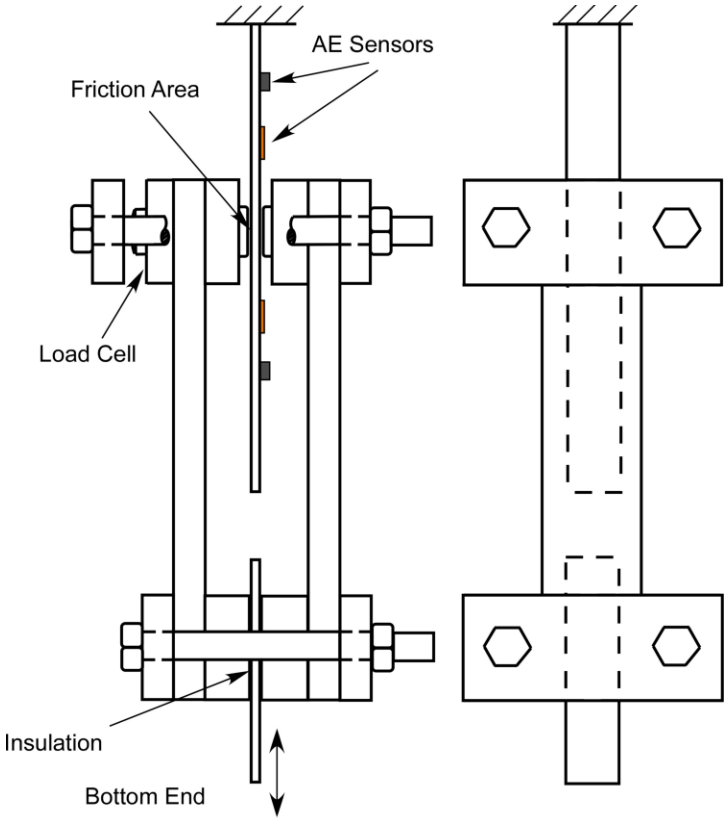

Figure 6.2. Schematic representation of the test fixture.

The bar was instrumented with wide band and resonant frequency acoustic emission sensors placed on either side of the friction region. The side mountings which held the friction pads were designed to be stiff compared to the steel bar participating in the friction process. The contact pressure between the pads and the bar was monitored using a load cell. The readings of the load cell during the cyclic motion were monitored on an oscilloscope.

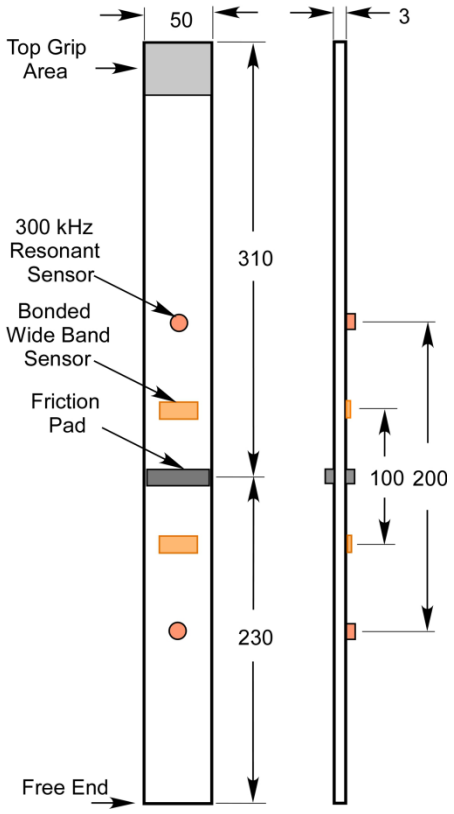

Figure 6.3. Steel bar dimensions.

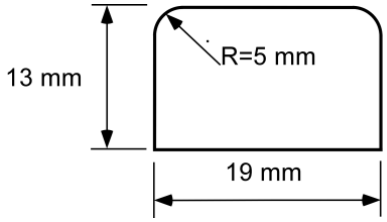

Figure 6.4. Dimensions of friction pads.

Four AE transducers were used to detect the friction related acoustic emission signals. The first set of transducers were PAC R30 (Ch.3) sensors. The second set of transducers were piezoelectric wafers (Ch.3) bonded to the surface of the steel bar as shown in Figure 6.3. The two types of sensors had comparable sensitivities, but their frequency responses were widely different. Sensor locations are also shown in the figure. AE source location capability with sensors positioned on opposite sides of the friction region helped in isolating signals of interest in the present study. The results included in this paper were obtained using the bonded

piezoelectric wafer sensors. Most of the data acquisition was performed using PAC preamplifiers with 40 dB gain and PIC-2 data acquisition system (Ch.3).The complete waveforms were acquired at a rate of 5 x 10^6 samples/second and a 35 dB threshold was set for acquisition. These waveforms were further processed on a personal computer.

6.3 Friction Test Procedure

The results included in this paper correspond to sinusoidal motion of the friction pads while the steel bar was held stationary by gripping at its top end. The steel bar was free at the bottom end. Acoustic emission signals corresponding to different combinations of parameters such as surface roughness, normal pressure, stroke length, and velocity were recorded and examined. The range of variations in these parameters governing the friction condition is listed in Table 6.1.

Table 6.1

Parameters for which AE signals were generated

Friction Parameter	Value 1	Value 2
Contact pressure, P, MPa	2	4
Loading frequency, F, Hz	0.5	1
Axial grip disp. amplitude, A, mm	0.25	0.5
Bar surface roughness, R_{ab}, μm	0.48	---
Friction pad roughness, R_{ap}, μm	0.15	1.54

Table 6.2 lists the eight different combinations of friction parameters for which acoustic emission data were acquired. The first four tests with prefixes RS, involved the steel bar with relatively rough surface (R_{ab} = 0.48 μm) and friction pad with relatively smooth surface (R_{ap} =

0.15 μm). The last four tests with prefixes RR involved the same steel bar with relatively rough surface and friction pads of comparable roughness (R_{ap} = 1.54 μm). These four tests had the same pattern of normal pressure, stroke length applied at the lower grip, and cyclic frequency as the first four tests. The axial load generated in the bar depended on the contact pressure, surface roughness, axial displacement, and the stick-slip conditions prevailing at the frictional interface. The axial load was measured by the MTS load cell. The relative displacements of the lower grip as well as the frictional force transferred through the friction pads during the reciprocating motion were recorded by the acoustic emission data acquisition system.

Table 6.2

Combinations of parameters for which AE signals were generated

Test	Roughness, R_{ap}, μm	Pressure, P, MPa	Frequency, F, Hz	Amplitude, A, mm
RST1	0.15	2	0.5	0.25
RST2	0.15	2	1	0.5
RST3	0.15	4	0.5	0.25
RST4	0.15	4	1	0.5
RRT1	1.54	2	0.5	0.25
RRT2	1.54	2	1	0.5
RRT3	1.54	4	0.5	0.25
RRT4	1.54	4	1	0.5

Two sets of experiments, termed Set A and Set B, were performed separately to measure different parameters of interest. The contact surfaces used in these two sets had nominally identical roughness values. Tests on Set A were performed to check if measurable surface

degradation was taking place during the tests RST1 to RST4 listed in table 6.2. Surface roughness values at the initial condition as well after 1000, 1300, 1600, 1900, and 2200 cycles were measured. Both R_a and R_z values were measured for the pair of pads and the bar at 40 different spots distributed over the contact area. These results, presented in the next section, indicate that the surface roughness values remained essentially unchanged during these experiments. Further since the hardness of the bar was significantly lower than the friction pads (HRB 96 for the bar versus HRB 123 for friction pads), if measurable wear occurred during these experiments, the bar surface would have been the first to indicate such changes. Hence at the end of eight segments of cyclic loading used in Set B, the final roughness values of the steel bar, were measured at 40 locations and was found to be substantially same as that of its initial value.

Individual tests corresponding to each of the eight combinations of parameters listed in Table 6.2 lasted only 300 cycles of reciprocating motion to ensure that the surface roughness remained nearly constant during these tests. The pair of surfaces comprising of the bar (R_{ab} = 0.48 μm) and smooth pad (R_{ap} = 0.15 μm) were subjected to 1000 cycles for initial test setup and four segments of 300 cycles each for the four tests RST1 to RST4. Similarly the pair of surfaces comprising of the bar (R_{ab} =0.48 μm) and rough pad (R_{ap} = 1.54 μm) were subjected 1000 cycles for initial test setup and four segments of 300 cycles each for the four tests RRT1 to RRT4. Further, these surfaces were also cleaned before the fixture was reassembled for the next segment of the test.

6.4 Roughness of Contact Surfaces

The results from cyclic loading of surfaces in set A are shown in Figure 6.5. The surface roughness values R_a and R_z were measured for the friction pads corresponding to the conditions in tests RST1 to RST4, each lasting 300 cycles, and their variation is plotted in Figure 6.5 (a) and

(b). The percentage variation in the values of R_a and R_z over the 1200 cycles, respectively were 5.8 % and 5.4 %, suggesting that the surface conditions remained nearly constant. This level of variability was seen between different regions of the same surface.

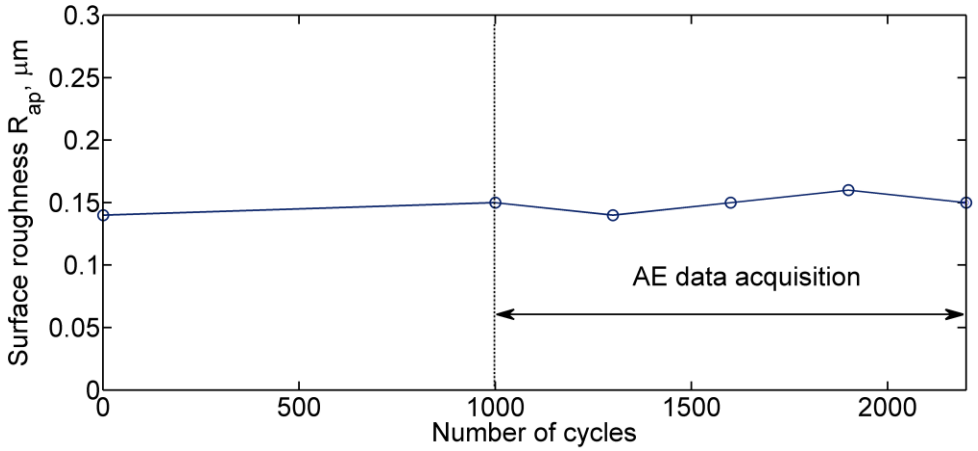

(a)

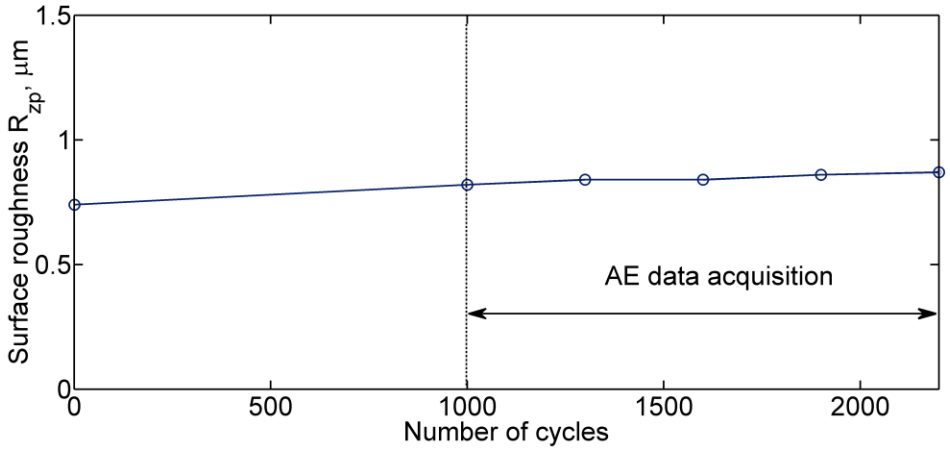

(b)

Figure 6.5. Surface roughness measurements (a) R_a and (b) R_z.

6.5 Stick-slip and Acoustic Emission Events

Figure 6.6 shows the variation of bottom grip displacement as well as the load transferred through the frictional interfaces for different test conditions. While the bottom grip was undergoing sinusoidal displacement, the load transferred across the frictional interface, as

measured by the MTS load cell, was deviating significantly from the sinusoidal shape, indicating slip at the frictional interfaces. In these figures, downward displacements are considered positive.

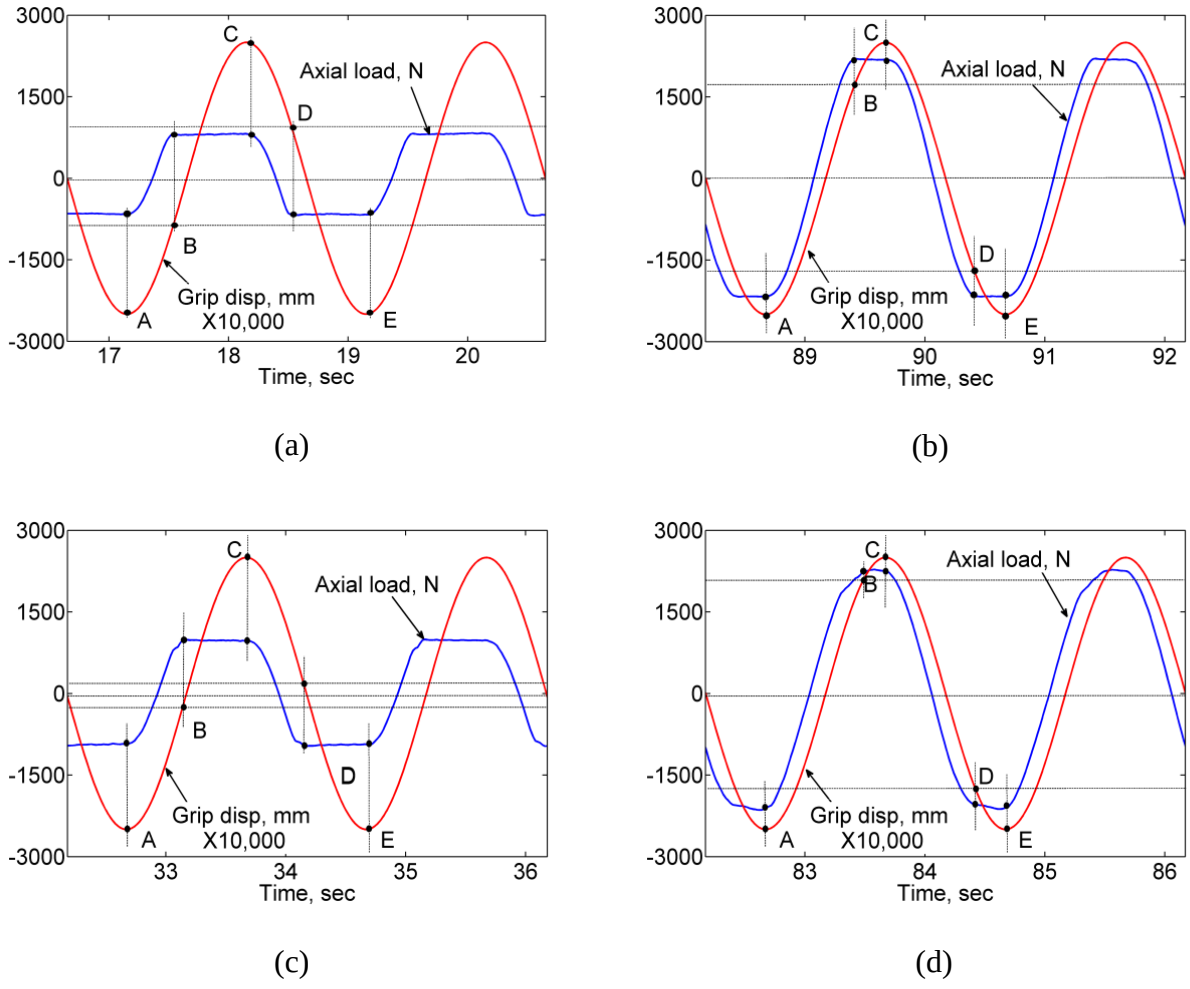

Figure 6.6. Relationship between the lower grip displacement and axial load in the steel bar indicating repetitive stick-slip motion during cyclic loading of four different tests.

In Figure 6.6(a), as the bottom grip moves from point A to point B, there is a proportional increase in axial load induced in the bar, indicating that the steel bar's surface that is in contact with the friction pad was experiencing essentially the same displacement as the pad – stick phenomenon. However, at point B, the proportionality between the displacement and the load ceases. In the segment B to C, the axial load induced in the steel bar essentially remains constant

while the displacement keeps increasing – this is the slip phenomenon. As the grip reverses direction at point C and moves towards point D, the load starts following the displacement in a proportional manner – this is the stick phenomenon. At point D, there is slip between the plate and the friction pad in the reverse direction. This stick-slip phenomenon repeated itself without recognizable variation throughout the nearly 300 cycles applied at this load. Stick-slip phenomenon for other combinations of surface roughness and normal pressure are shown in Figures 6.6 (b) to (d). A comparison of figures 6.6 (a) and (b) or (c) and (d) indicates that the surface roughness of the friction pad (R_{ap} = 1.54 μm vs. R_{ap} = 0.15 μm) has a small influence on the load level at which gross slip begins.

The displacement of the friction pads appeared to follow the same sinusoidal shape of the bottom grip. However, the magnitude of displacement was much smaller because during the "stick" period, the bar was extending and contracting due to the applied load. Based on the maximum load generated on the steel bar and corresponding displacement of the steel bar's surface that is in contact with the friction pads, the amplitude of displacement of the friction pads for each of the cases RST1 and RRT1 shown in Figure 6.6 is estimated to be about 27 μm. The estimated distance of slip for the cases of RST1 and RRT1 is about 18 μm; for the cases of RST3 and RRT3 is about 4 μm.

Figure 6.7 shows the plot of the time of occurrence of AE events during the stick-slip cycles for the case of RRT2 (F = 1 Hz, R_{ap} = 1.54 μm, A = 0.5 mm, P = 2 MPa). Red circles on the load curve indicate the instants at which AE events were recorded. AE events occurred predominantly during the slip portions. No significant variation of the AE pattern was seen over the nearly 100 cycles, corresponding to the duration of the test.

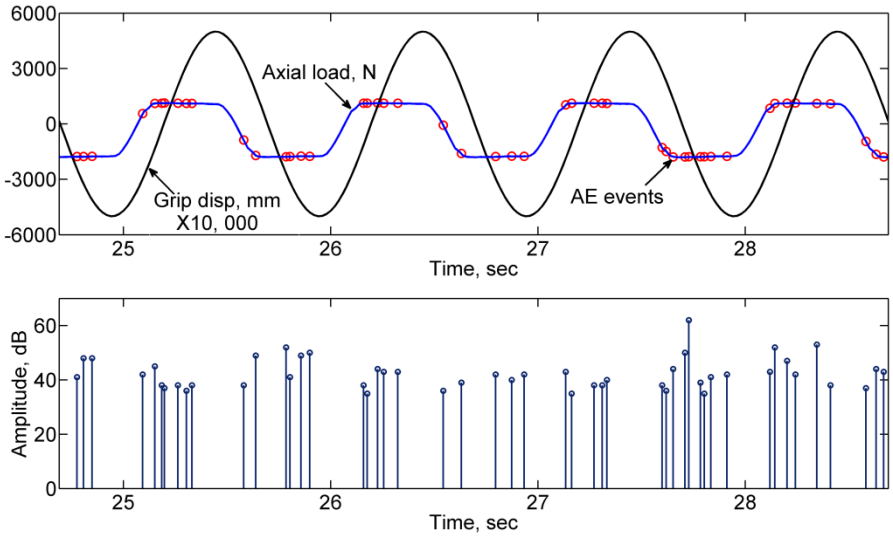

Figure 6.7. The time of occurrence and amplitudes of AE events for RRT2.

During each of the slip segments of the cyclic motion, such as BC in Figure 6.6(a), whose duration is one second, a large number of acoustic emission events are likely to be generated because of the numerous collisions of asperities present on the friction pads with those on the steel bar. However, in these tests, on average about 5 acoustic emission events of varying amplitudes and durations were recorded per half cycle. It is likely that among many AE events generated during this period, only a few that exceeded the threshold value were recorded. In addition, for the events recorded, there might be a superposition of a number of acoustic emission signals corresponding to numerous individual collisions occurring either simultaneously or in short succession within a few tens of microseconds of each other.

6.6 Friction Related Waveforms

Nearly 70% of the AE events recorded during these tests originated from the region of frictional contact between the friction pads and the steel bar. Signals originating from other locations were excluded from this analysis based on source location. Figure 6.8 shows a typical waveform corresponding to friction related AE event obtained during the slip phase of test RST4

(R_{ap} = 0.15 µm, P = 4 MPa, A = 0.5 mm, F = 1 Hz). Most waveforms are characterized by large amplitude at the start of the waveform followed by gradually decreasing amplitude, which extended to a little over 500 µs. Further, as in lead-break tests, the arrival of the reflections from the ends of the bar could also be observed. A major difference is that the quiet period between the initial pulse and reflections seen in the lead-break events was not present in the friction related events.

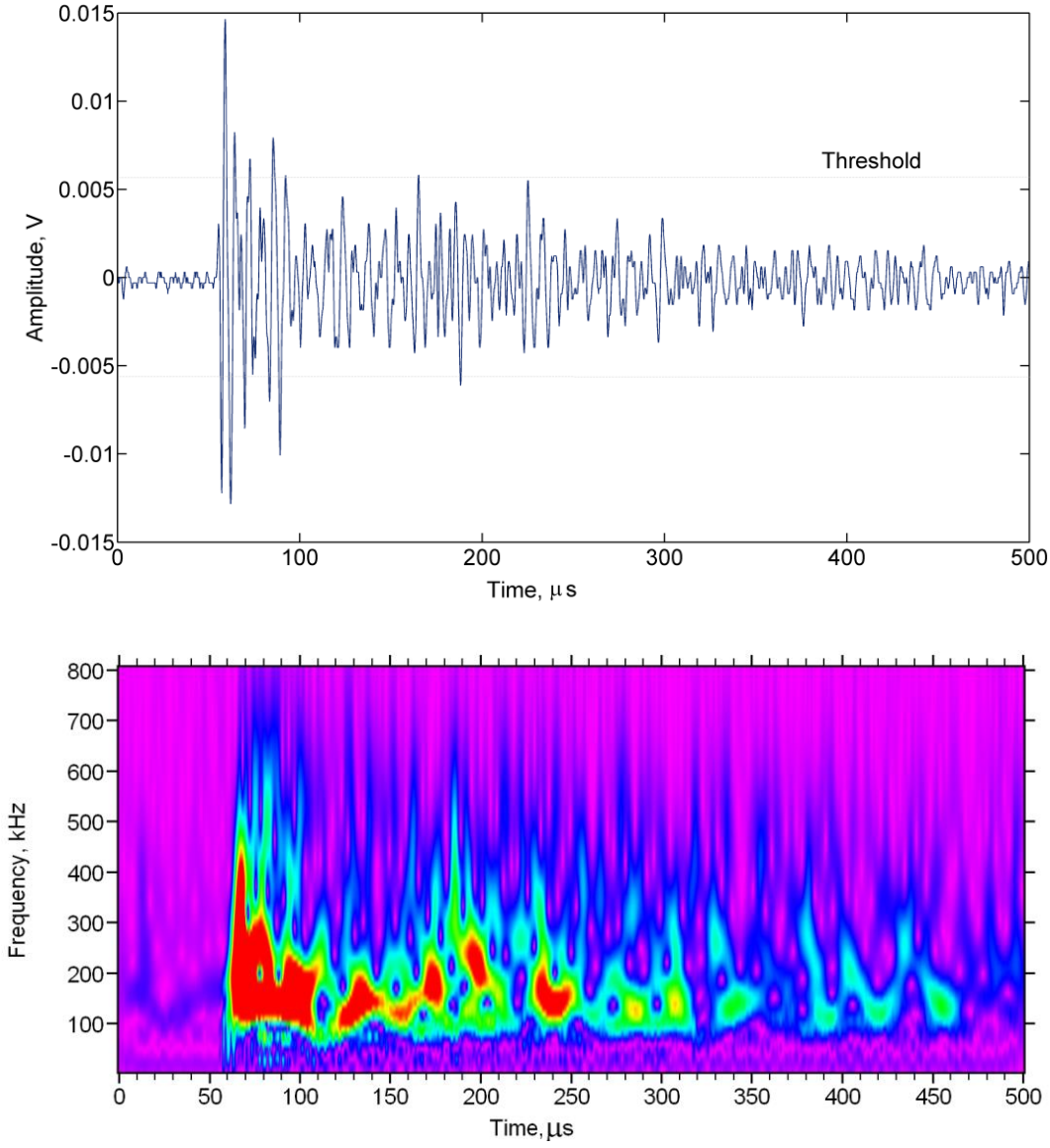

Figure 6.8. AE waveform and wavelet diagram for friction related event from test RST4.

The peak amplitudes of individual friction related AE events rarely exceeded a level of 50 dB for the frequency band above the 100 kHz used in these tests. The amplitudes of friction related events corresponding to RRT2 are shown in Figure 6.7. Friction related events under other conditions reported in this paper were also having similar amplitude distributions. The relatively low amplitudes seen in these experiments can be attributed to the modest normal pressures used in these experiments, chosen mainly to avoid surface damage during these experiments and the deliberate choice of frequency band above 100 kHz to avoid ambient noise.

6.7 Characterization of the Friction Related Acoustic Emission Waveforms

Recent studies have revealed that acoustic emission technique can be useful tool to monitor surface damage in bearings and gears. In the following section, we will examine whether the features embedded in the acoustic emission waveform are indicative of differences in the operating conditions at the interface of such surfaces during their relative motion. The study included the acquisition and analysis of AE signals corresponding to different combinations of the parameters listed in table 6.1. The effect of the surface roughness of the friction pad, the normal pressure between the contact surfaces, and the sliding velocity on the acoustic emission waveform and its frequency content are examined.

The amplitude distributions of AE events did not have recognizable variations for the different tests performed under this study. Figure 6.9 shows the amplitude distribution for the cases RST2 and RRT2. However, it should be noted that the normal pressure values used in these experiments were relatively small with limited range of variation. Further, the frequency range that is considered here is above 100 kHz for the most part so as to avoid ambient sources of acoustical signal which dominate in the lower frequencies.

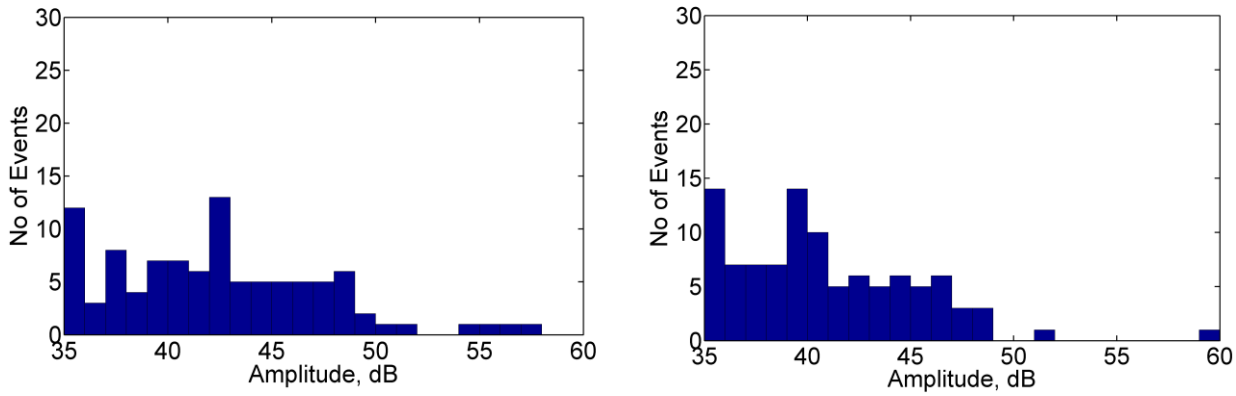

(a) (b)

Figure 6.9. Comparison of amplitude distribution for different tests (a) RST2 and (b) RRT2.

6.7.1 Effect of surface roughness. The features of the AE signals corresponding to variations in the operating conditions such as surface roughness, normal pressure, and sliding velocity that are highlighted in the following sections were identified after examining a collection of waveforms and their wavelet diagrams corresponding to each type of test. To obtain a consistent interpretation, for each test condition, the average pattern seen in 25 randomly selected waveforms was used. The selection of the waveforms considered the amplitude of the signal waveforms which helped to compare signals of equivalent amplitude.

The differences between the acoustic emission signals generated in test RST1 (R_{ap} = 0.15 µm) and test RRT1 (R_{ap} = 1.54 µm) are considered first. The only difference between these two tests was the surface roughness of the friction pads. The randomly selected waveforms obtained during each of the two tests were used to examine the frequency-time patterns of the AE signals. To highlight the common features found in these tests and make comparison between the two, representative waveforms and their wavelet diagrams from the tests are shown in Figure 6.10. A similar comparison between test RST3 and RRT3 is also in Figure 6.11.

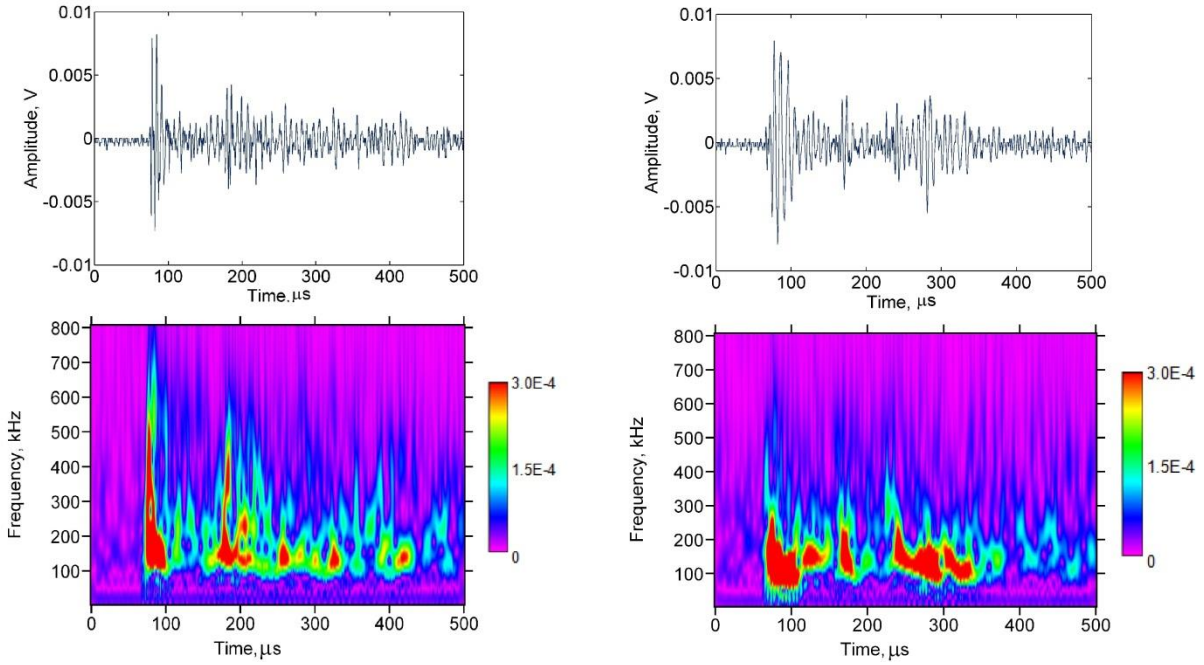

Figure 6.10. Effect of roughness shown by wavelet diagrams (a) test RST1 (b) test RRT1.

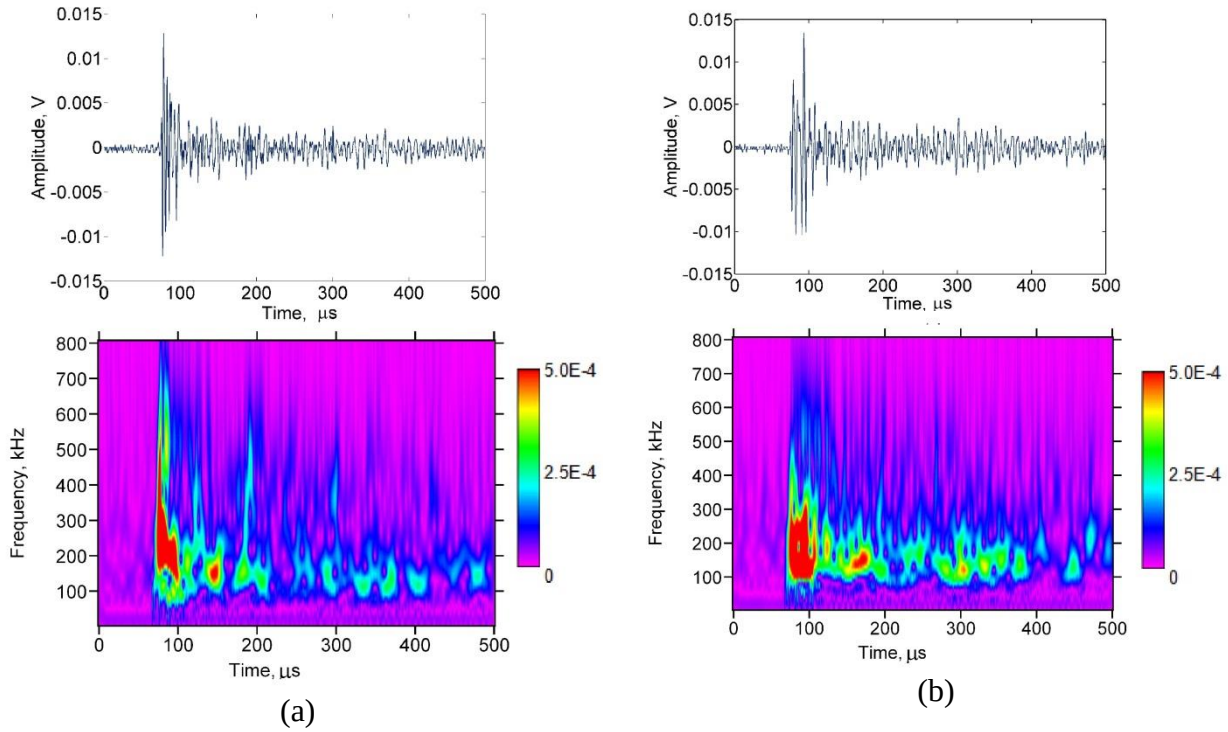

Figure 6.11 Effect of surface roughness shown by wavelet diagrams (a) test RST3 (b) test RRT3.

The wavelet diagrams corresponding to AE signals from the RS cases included in Figure 6.10 and Figure 6.11 show the presence of components in excess of 500 kHz at the leading edge of the signals whereas the wavelet diagrams corresponding to AE signals from the RR cases had no significant amplitude above this frequency range. It was found that, for tests involving smooth pads, more than 70% the signals had this distinct high frequency component while only 20% of the waveforms for rough pads had such components, irrespective of the amplitude of the signal.

It should also be noted that the sensors used in these experiments were not sensitive to frequencies greater than 700 kHz. Further, as noted earlier, the instrumentation used for these experiments had reduced sensitivity for frequency components outside 200 kHz to 400 kHz band. The presence of frequency components from 600 kHz to 700 kHz for RST1 and RST3 are significant considering that the gain at 600 and 700 kHz were only 33% and 21% of the gain in the frequency band spanning 200 to 400 kHz. These differences in the frequency content seen in the wavelet diagrams were not easily observable in the FFT diagram of these signals. The dependence of the frequency content of the AE signal on the surface roughness was predicted from an earlier numerical simulation of friction process (Alam & Sundaresan, 2010)

Another observation from these tests is that RS combination gave rise to larger number of AE signals compared to RR combinations for otherwise similar conditions. The envelopes connecting the peaks of individual oscillations in the AE signal indicate the presence of multiple events and reflections of the waveforms from specimen ends. There were only minor differences in the envelopes of the AE signals obtained within each test. In addition, apart from the differences observed in the frequency content described above, there were no other recognizable differences between the envelopes enclosing the waveforms obtained for the smooth pad versus those for rough pads.

6.7.2 Effect of sliding velocity. The velocity during the relative motion between the mating surfaces in the present study depended on the frequency and amplitude of the reciprocating motion while the other parameters were held constant. For such a comparison, the wavelet diagrams corresponding to the RRT1 case (F=0.5 Hz, A = 0.25 mm) is presented with those for the RRT2 case (F=1 Hz, A = 0.5 mm). The doubling of the loading frequency and displacement amplitude for RRT2 results in quadrupling of the average sliding velocity from RRT1 to RRT2. Corresponding waveforms and wavelet diagrams are shown in Figure 6.12 (a) and (b).

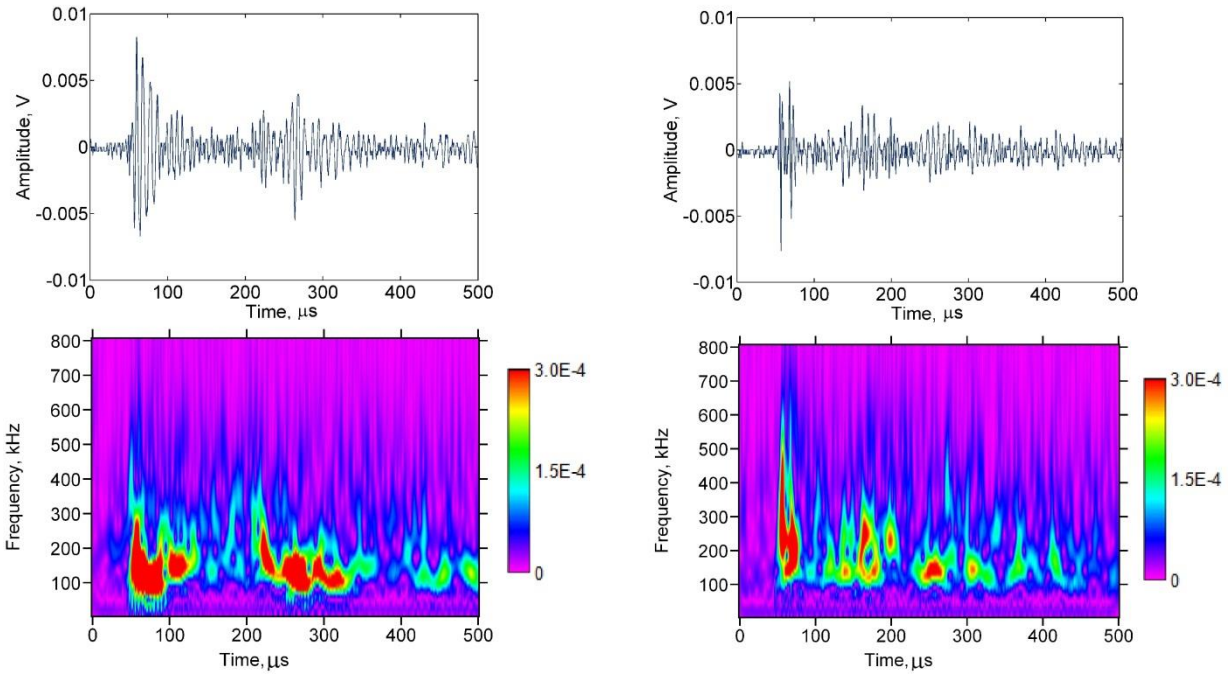

Figure 6.12. Effect of sliding velocity shown by wavelet diagrams (a) test RRT1 (b) test RRT2.

These figures show that signals with frequency content in the range of 100 to 300 kHz decrease and those in the range of 400 kHz and above increase as the sliding velocity is increased. A similar influence of the increase in the sliding velocity on the increase in the AE frequency components was observed also between RST1 and RST2. These tendencies were seen

in a majority of the signals collected. However, there were exceptions to these trends in a few of the AE signals.

6.7.3 Effect of normal pressure. The influence of the normal pressure on the AE signal is examined by comparing the results for RRT1 for which the normal pressure was 2 MPa with those of RRT3 for which the normal pressure was 4 MPa. These results are shown in Figures 6.13 (a) and (b).

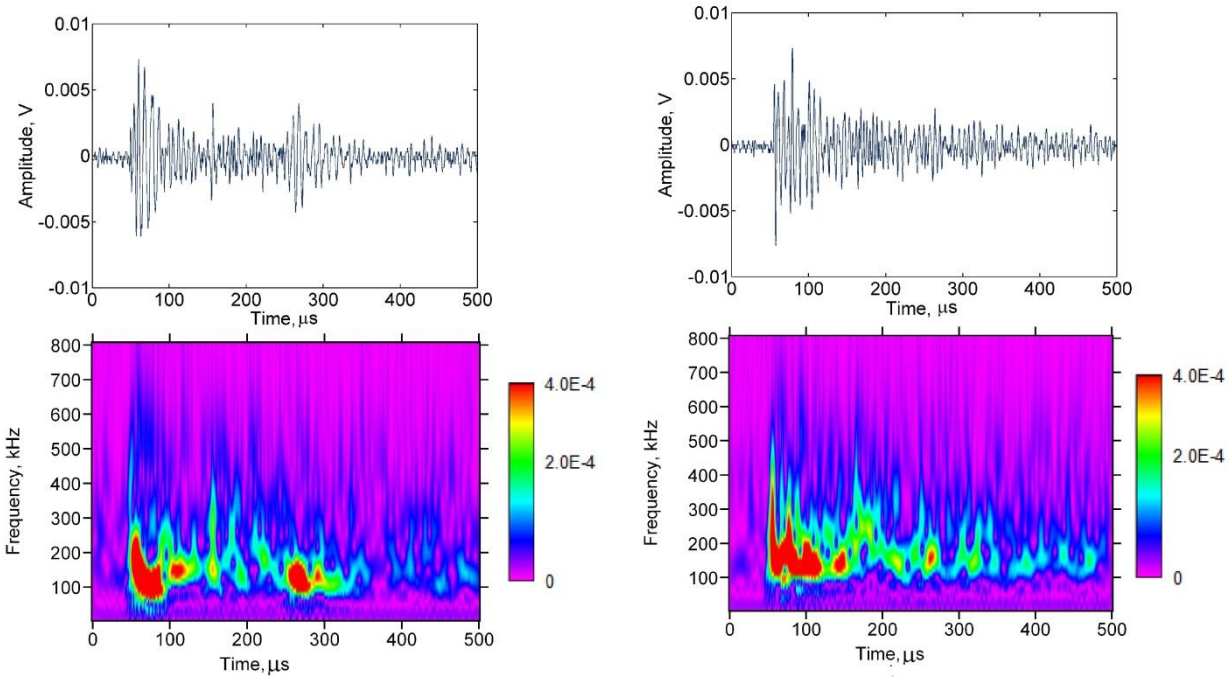

Figure 6.13. Effect of pressure shown by wavelet diagrams (a) test RRT1 (b) test RRT3.

The main difference between the two waveforms was in the intensity of the AE signal between the first arrival and the reflections from the specimen ends. For the case of RRT3, there was significantly greater signal strength before the arrival of the reflection. At higher normal pressures, greater interference between the asperities in the surfaces in contact is likely to be present. As a result, a greater number of asperities are likely to participate in generating the AE signals. Changes in the normal pressure did not seem to affect the frequency of the signals.

6.8 Crack Growth Test

A crack was initiated and grown in a steel bar with properties similar to the one used for the friction test. In order to initiate crack, a 0.4 mm deep notch was cut with EDM wire of 0.05 mm (0.002") diameter. The bar was loaded under three-point bending, figure 6.14, using 642.10B roller block assembly for MTS testing machine (MTS810 reference manual)

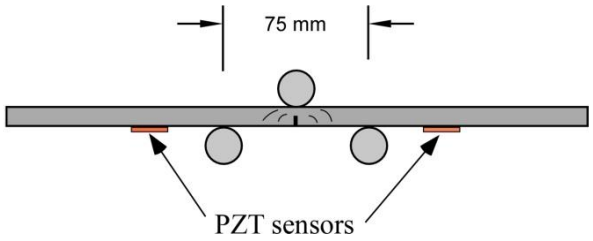

Figure 6.14. Schematic representation of crack growth test.

The bar was loaded under progressively increasing load amplitudes until the load at which crack growth was first noticed. The minimum and maximum values of the load at which crack initiated were 550 N and 1900 N respectively. The frequency of loading was increased to 10 Hz and maintained at this value for approximately 1 and 1/2 Hrs. Noticeable size of crack, figure 6.15, was obtained at this stage. In the following loading phase, at loading frequency of 2 Hz, crack growth continued up to fracture. Approximately, not more than 2000 cycles were required to cause fracture of the bar.

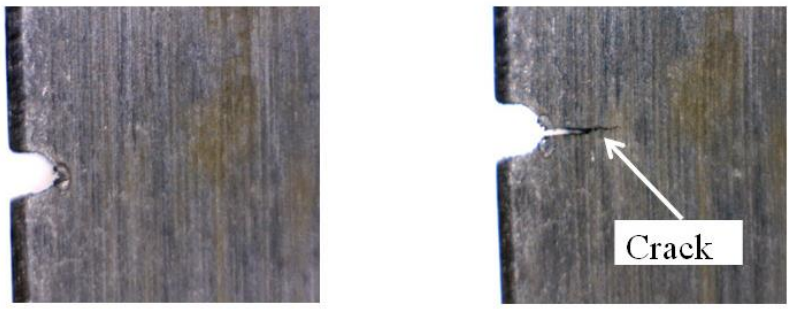

(a) (b)

Figure 6.15. Steel bar: (a) before initiation of crack (b) after crack was fully grown (10X).

Similar to the case of the friction experiment, the bar was instrumented with bonded PZT sensors. The signals generated during incremental crack growth were picked by these sensors and recorded by PCI-2 data acquisition system. The acquisition settings used in this experiment were similar to those used in the friction experiments. Figure 6.16 shows a waveform and its wavelet diagram obtained from incremental crack growth test.

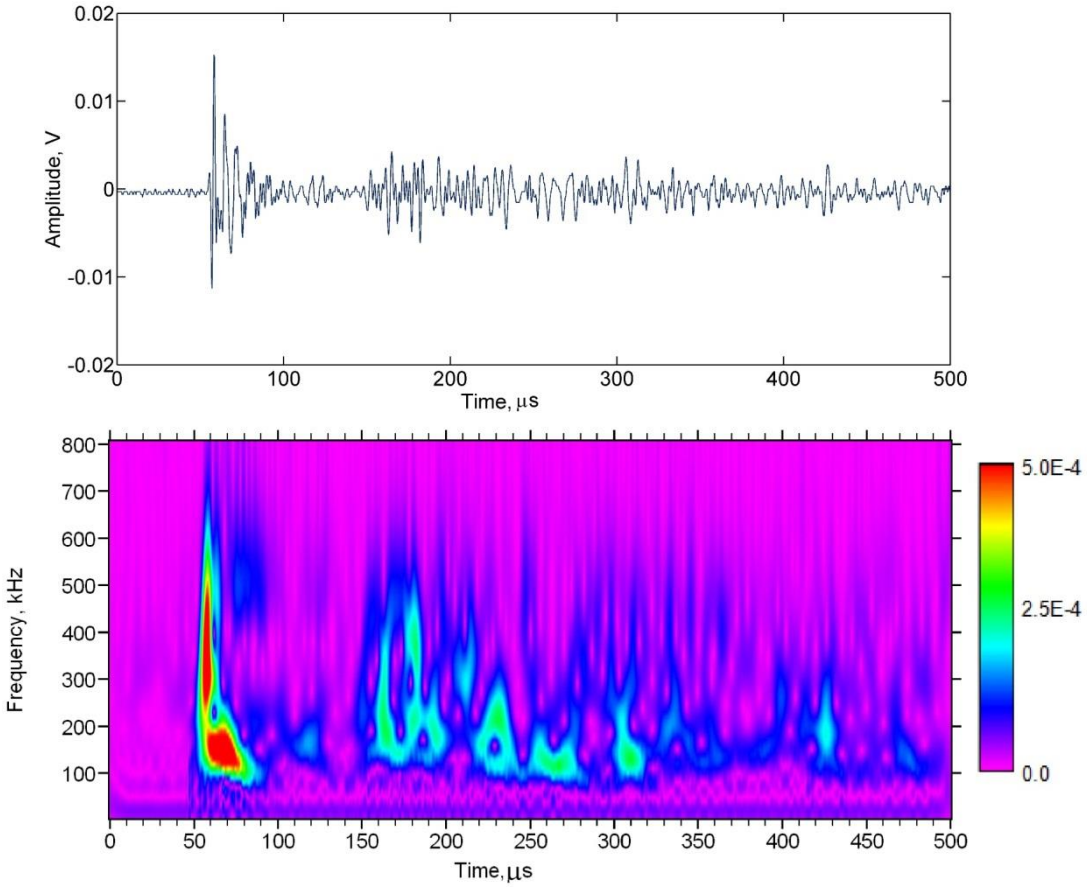

Figure 6.16. AE waveform and wavelet diagram for crack growth event.

Since the sensors were placed in similar manner to the sensors in the friction test, the activities beyond 120 µs from trigger point are reflections of the "first components" from the end of the bar. Depending on the increment in crack size, the strength of the signal varies and in this experiment, the amplitude distribution for the signals varied between 35and 99dB. Most signals

at the beginning of the test had amplitude distribution bound between 35 and 60dB. However, at stages close to rupture, the strength of the signals shifted to the higher values.

6.9 Friction AE Signals vs Crack Related AE waveforms

6.9.1 Identification of symmetric and anti-symmetric modes. One of the most visible differences between crack and friction signals, found during the experiment, is distinguishability of symmetric and antisymmetric modes. Comparison of Figure 6.8 and Figure 6.16 reveals that the symmetric and antisymmetric modes of the waves were clearly present, at the point of trigger, in the crack related signals while the same components could not be distinguished in friction related signals. Survey of 360 friction related waveforms and 70 crack related waveforms indicated that these modes of wave propagation were present in 89% (62/70) of the crack signals, and were missing in 83% of friction related waveforms.

Acoustic emissions from crack growth, as the bar is loaded under fatigue, are associated with the release of strain energy due to new surface formation. The experimental results prove that the waves generated during this process depict a single event behavior in which the symmetric and antisymmetric modes can be identified. In addition to the above crack signals, visual assessment of more than 500 waveforms proves most of the signals show this behavior. The relative presence of the symmetric and antisymmetric modes of wave propagation is affected by the location of crack growth along the thickness and the mode of crack growth. For example, a bar, for which crack was simulated at the neutral axis, revealed stronger symmetric modes (Rajendra, et al., 2011)

The mechanism behind generation of AE events during friction is at most attributed to collisions of asperities present on the surfaces. Superposition of a number of acoustic emission signals corresponding to numerous individual collisions occurring either simultaneously or in

short succession within a few tens of microseconds of each other makes the waveform patterns different from crack growth waveforms. This makes the distinguishability of the fundamental modes difficult in friction related signals. The difference in AE activity is further discussed in the next section.

6.9.2 Duration of waveforms. Presence of stronger AE activity following the "first" pulses contributes to higher duration signals. The illustration of this fact is shown in Figure 6.8 and Figure 6.16. The strength of AE activity following the initial pulses is stronger in the case of friction related signals. Randomly selected waveforms were visually compared for duration. Fretting waveforms from the different cases were selected and visual comparison was done with 10 crack signals. Figure 6.17 shows, during the interval 70 to 160 μs, the activity in the fretting signal is stronger than that of the crack signal. Comparison of the points at which the strength of the signal passes the threshold level shows fretting related signals stay on average of 20us and more beyond that of crack related signals.

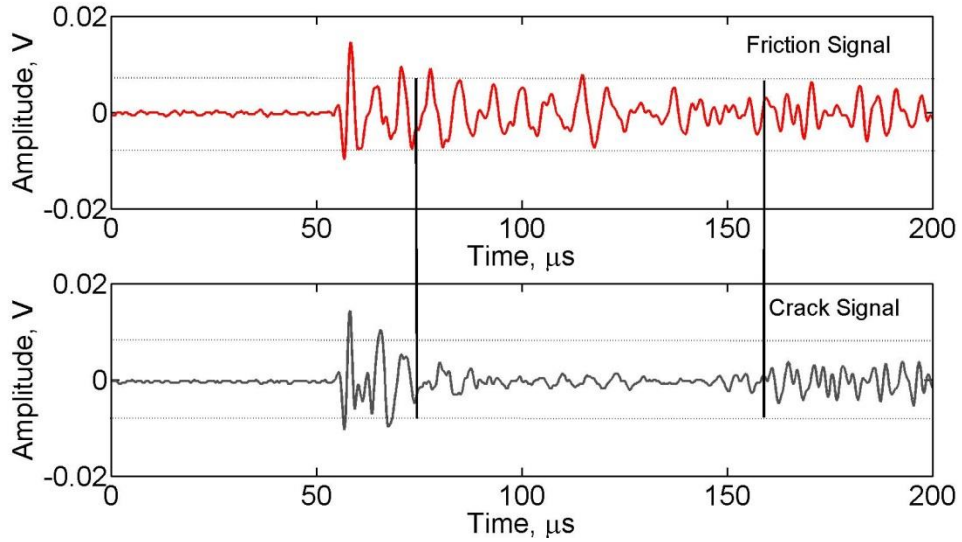

Figure 6.17. Duration comparison.

Waveforms of similar amplitude from each friction experiment were selected and the duration for the group was compared with duration of a group of crack signals of similar amplitude. Figure 6.18 shows the comparison of the group of waveforms at 37dB and 38dB. The interpretation of the graph is: for example, among those friction signals having amplitude of 37dB, 55% of them have duration of 20 µs or less, while 97% of the crack events have duration of 20 µs or less. Similarly, of those friction waveforms at amplitude of 38dB, 50% have duration of 20 µs or less. However, 92% of crack signals at the same amplitude have duration of 5 µs or less. Such analyses were carried out for amplitudes 36-41 dB, and the same tendency was witnessed in all the cases. The extended AE activity region shown in fretting signals, which is attributed to multiple AE sources in friction was seen in the duration of these signals Results from numerical simulation (Alam 2010) also proved continued AE activity zones as compared to the crack signals.

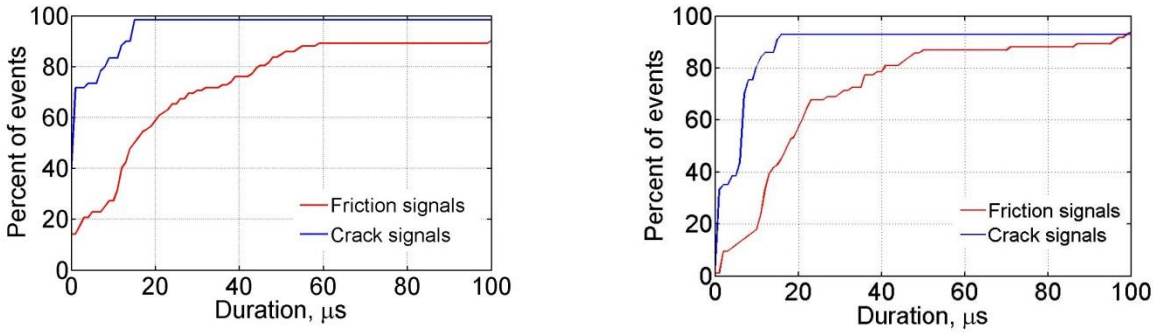

(a) (b)

Figure 6.18. Events vs duration: a) 37dB amplitude b) 38dB amplitude.

6.9.3 Correlation with simulated AE signals. To show the difference between the source mechanisms in these two cases, a single event acoustic emission was simulated on steel bar for which the material properties were exactly the same as the one used in the tests. The simulation was done by applying an impulse load discussed in chapter four to the FEM model.

The duration for the pulse type load applied on the model was 2μs. Figure 6.19 shows the crack signal and the numerical AE event signal plotted together.

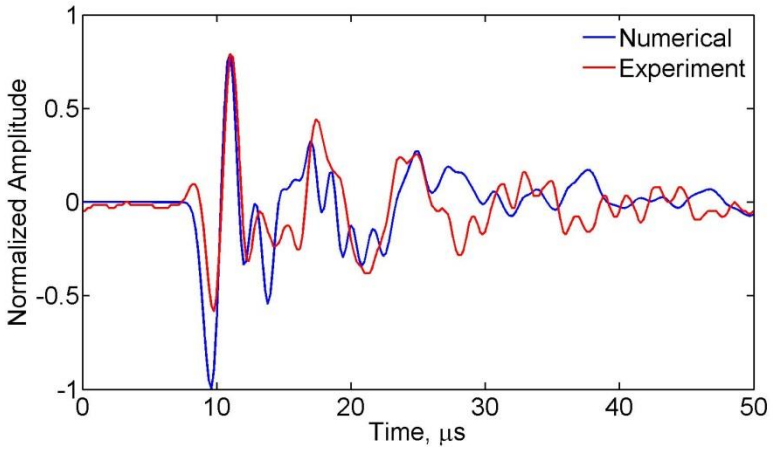

Figure 6.19. Numerically simulated and experimental crack growth signal.

It can be seen on the figure that, the basic pattern of the waveforms, both numerically simulated and experimentally obtained crack growth signal waveforms, are similar. The symmetric and antisymmetric modes can be seen, even though affected by the reflections from side edges. This indicates that the crack related signals largely exhibit single event behavior.

Sample crack growth and friction related signal waveforms were correlated with the numerical signals to examine the above stated fact of single event vs multiple event behavior. MATLAB code was generated which resamples the numerical signals at 0.2 μs which is equal to the data acquisition rate for the experimental signals and correlates the resampled numerical waveforms and the experimental signals. The code is attached in Appendix B of this manuscript.

Several crack and friction waveforms at amplitude of 38dB, 43dB and 47 dB were selected and correlated with the numerical waveforms. It was found that the crack signals, on average, have shown 65% correlation with the numerical waeforms, while, the level of correlation with the friction related signals remained, on average, at 40%. The numerical models did not take into account the attenuation or material damping effects on the waveforms, even

though, these effects are far less in steel as compared to CFRP panels. In addition, the waveform for an acoustic emission event during crack growth is dependent on the location. Thus, these factors could have effect on the correlation of crack signals with the numerical signals which remained at 65%. Also, definition of appropriate boundary condition and material definition could have an impact. Nonetheless, comparison of the two average correlation coefficients indicates difference in the characteristics of the two types of waveforms.

6.10 Summary

In this part of the research, we explored if the parameters controlling the interaction of two contacting surfaces during the friction process were recognizable in the acoustic emission waveforms and if those features could be clearly identified. A test fixture to simulate the reciprocating motion between two flat surfaces in contact was developed. In this fixture, the parameters such as normal pressure, surface roughness, sliding velocity could be closely controlled. Acoustic emission signals generated by the friction process for different combinations of surface roughness, normal pressure, and the velocity of sliding were evaluated.

Friction related waveforms, in general, depicted patterns that were consistent with multiple asperity interactions during slip. The basic features of friction related AE signals were distinct from those of other AE sources. Clear and systematic changes in the signal characteristics that could be related to the parameters operating at the frictional interface were found. Acoustic emission frequency components well in excess of 700 kHz were generated by the friction process. Frequency of the signals was found to increase as the roughness of one of the surfaces was decreased. In addition, the frequency content was also found to increase with the increase in sliding velocity. AE signal duration appears to increase with an increase in normal pressure.

Crack related events were, in some respects, similar to that of lead-break waveforms. These waveforms are characterized by a strong initial component followed by a relatively quiet period after which reflected signals are seen. This, however, is in contrast to friction related signals for which there is sustained signal amplitude between the initial segment and the segment due to reflections. Comparison of the wavelet diagrams corresponding to the lead break test and the crack growth tests with the wavelet diagram due to the friction related signal is useful in understanding the source mechanisms in these three cases. The first two types of events are generated by a single impulse and the resulting initial segment is well separated from the segment corresponding to reflections from the specimen ends, as seen clearly in the waveforms as well as wavelet diagrams. In the case of friction related signals, the sustained activity between the initial segment and the reflected segment is indicative of multiple impulses occurring within microseconds of each other. Such a process of simultaneous or sequential interaction of asperities belonging to the contact surfaces has been postulated in the literature (Alam & Sundaresan, 2010; V.M. Baranov, et al., 2011; Fan, et al., 2010).

AE waveform features obtained during these experiments were indicative of the tribological conditions. Frequency components in excess of 700 kHz were seen during these experiments. The characteristics of the experimentally observed acoustic emission signals were in general agreement with earlier numerical predictions. Friction related acoustic emission signals were distinguishable from those from other sources such as fatigue crack growth. The distinguishing features of crack related and friction related signals could serve the purpose of identifying signals from different sources, particularly from sources generating false positives which are critical in AE analysis. Also, the characterization of friction related acoustic emission

with the parameters governing friction conditions signals is likely to be of value in many tribological and structural health monitoring applications.

CHAPTER 7

Conclusions and Future Work

Three important problems that could help advance, implement AE based structural health monitoring on structures were addressed in this dissertation. These were examining the influence of attenuation on acoustic emission signals and their features, investigating damage progression in CFRP laminates, and identifying distinguishing features of acoustic emissions related to actual crack growth and emissions from other sources that give rise to false positive signals. Experiments were part of each research problem dealt with in the research. In addition, numerical simulation of acoustic emission events and wave propagation in metallic and CFRP laminates were also included. Numerical simulations of friction related events were reported (Alam & Sundaresan, 2010) and were considered preliminaries for the experimental work in chapter 6.

In addition to the acoustic emission tests, several other tests were conducted. Results of thermography scans of the CFRP laminates used for attenuation and delamination tests were reported in Chapter 4. Trial tests were conducted to compare the features of wave propagation in composite and aluminum panels. Different sets of tests were conducted to assess the frequency and amplitude responses of the three types of transducers used in the experiments. The results from these trial tests were reported in Chapter 3.

The important results from each part of the research are summarized below:

Attenuation tests

- The attenuation coefficients obtained from the experiments indicated that the fundamental modes of wave propagation had varying attenuation levels. The

antisymmetric wave propagation modes in the signals had attenuation levels that were three to four times those of the symmetric modes.

- The amplitudes of the signals were dependent on the directions along which measurements were taken
- The direction dependency of the attenuation coefficients was very limited. The obtained values were in the same order of magnitude.
- The degree of influence of the different attenuation mechanisms on the symmetric and antisymmetric modes were different. The antisymmetric modes were also found to be more dispersive than their symmetric counterparts.

Delamination tests

- Some features of the acoustic emission signals were indicative of delamination growth even with narrow margins of variation.
- Differences in the fiber layup of plies at the delamination growth zones were apparent in several of the AE related analyses and fracture mechanics behavior.
- The different failure mechanisms were classified based on the AE signals and their features. Events from fiber breaks were classified into high amplitude and high energy events. Based on the distribution and cumulative presence on the SEM images and energy plots, matrix crack events were related to low energy and low amplitude signals.
- Different types of wave propagation modes were identified with waveforms from numerically simulated acoustic events. The relative presence of the modes was affected by the location where the measurement was taken. Consistent with the

experimental waveforms, the features of the numerical waveforms were sensitive to the damage growth rate

Friction and crack related acoustic emission tests

- Friction related waveforms, in general, depicted patterns that were consistent with multiple asperity interactions during slip.
- The basic features of friction related AE signals were distinct from those of other AE sources.
- Acoustic emission signal frequency components in excess of 700 kHz were generated by friction process.
- Crack related signal waveforms were, in some respects, similar to lead-break signal waveforms.
- AE waveform features obtained during these experiments were indicative of tribological conditions. Clear and systematic changes in the signal characteristics that could be related to the parameters operating at the frictional interface were found.

The results reported in each chapter highlight the significance of material in this manuscript. In traditional acoustic emission analysis, particularly AE from damage growth, the influence of attenuation on acoustic emission signals has been paid little attention. The findings from the attenuation measurements indicate that the signals experience changes within reasonably short distances. This could impact the interpretation of signals from different sources. Damage identification using AE should thus include attenuation effects. The results from delamination tests indicated sensitivity of AE to damage initiation and growth. Some literature sources are available that focus on correlation of damage mechanisms with features of acoustic emission signals. The results from this research are deemed to expand the current understanding

of damage mechanisms and their features. The other major issue in acoustic emission method has been the presence of noise interference. The results from the last part of this research are considered a significant contribution to the effort to differentiate false signals from actual damage related signals.

In this research, as mentioned earlier, several problems were addressed. During the course of this research, some important issues were identified that could potentially be areas of further research. Some are listed below:

- The frequency response of PZT transducers and the width of electrode material on the wafers
- The evolution of attenuation behavior with loading
- The selection of transducer and coupling material for sending and receiving acoustic waves in composite laminates
- The examination of wave propagation features in anisotropic materials, both numerical and experimental
- The numerical modeling of damage mechanisms in composite laminates
- The analysis of acoustic emission signals generated by surface damage and wear

References

Al-Balushi, K. R., Samanta, B. (2002). *Gear fault diagnosis using energy-based features of acoustic emission signals.* Paper presented at the Proc. Inst. Mech. Eng., Part I: J. Systems and Control Engineering.

Al-Dossary, S., Hamzah, R. I. R., & Mba, D. (2009). Observations of changes in acoustic emission waveform for varying seeded defect sizes in a rolling element bearing. *Applied Acoustics, 70*(1), 58-81. doi: http://dx.doi.org/10.1016/j.apacoust.2008.01.005

Alam, M. T., & Sundaresan, M. (2010). *Characterization of fretting related acoustic emission signals.* Paper presented at the Proceedings os the SPIE.

Arumugam, V., Sajith, S., & Stanley, A. J. (2011). Acoustic Emission Characterization of Failure Modes in GFRP Laminates Under Mode I Delamination. *Journal of Nondestructive Evaluation, 30*(3), 213-219. doi: 10.1007/s10921-011-0109-5

Asamene, K., Knighton, T., Rajendra, D., Ali, B., Whitlow, T., Sundaresan, M., . (2011). *Monitoring the Structural Integrity and Prognostics of Composite Aircraft Components.* Paper presented at the Proceedings of the International Conference on Composites for 21st Century Current and Future Trends, Bangalore, India.

Asamene, K., & Sundaresan, M. (2012). Analysis of experimentally generated friction related acoustic emission signals. *Wear, 296*(1–2), 607-618. doi: http://dx.doi.org/10.1016/j.wear.2012.07.019

Baranov, V. M., Kudryavtsev, E. M., & Sarychev, G. A. (1997). Modelling of the parameters of acoustic emission under sliding friction of solids. *Wear, 202*(2), 125-133. doi: http://dx.doi.org/10.1016/S0043-1648(96)06969-4

Baranov, V. M., Kudryavtsev, E. M., Sarychev, G. A., & Schavelin, V. M. (2011). *Acoustic Emission in Friction*: Elsevier Science.

Barbero, E. J. (2008). *Finite Element Analysis of Composite Materials*: Taylor & Francis Group.

Ben Abdelounis, H., Le Bot, A., Perret-Liaudet, J., & Zahouani, H. (2010). An experimental study on roughness noise of dry rough flat surfaces. *Wear, 268*(1–2), 335-345. doi: http://dx.doi.org/10.1016/j.wear.2009.08.024

Biwa, S., Watanabe, Y., & Ohno, N. (2003). Analysis of wave attenuation in unidirectional viscoelastic composites by a differential scheme. *Composites Science and Technology, 63*(2), 237-247. doi: Pii s0266-3538(02)00202-6

10.1016/s0266-3538(02)00202-6

Bussiba, A., Kupiec, M., Ifergane, S., Piat, R., & Böhlke, T. (2008). Damage evolution and fracture events sequence in various composites by acoustic emission technique. *Composites Science and Technology, 68*(5), 1144-1155. doi: http://dx.doi.org/10.1016/j.compscitech.2007.08.032

Cesari, F., Dal Re, V., Minak, G., & Zucchelli, A. (2007). Damage and residual strength of laminated carbon–epoxy composite circular plates loaded at the centre. *Composites Part A: Applied Science and Manufacturing, 38*(4), 1163-1173. doi: http://dx.doi.org/10.1016/j.compositesa.2006.04.013

Corigliano, A., Mariani, S., & Pandolfi, A. (2006). Numerical analysis of rate-dependent dynamic composite delamination. *Composites Science and Technology, 66*(6), 766-775. doi: 10.1016/j.compscitech.2004.12.031

Corigliano, A., & Ricci, M. (2001). Rate-dependent interface models: formulation and numerical applications. *International Journal of Solids and Structures, 38*(4), 547-576. doi: 10.1016/s0020-7683(00)00088-3

D5528, A. (2007). Standard Test Method for Mode I Interlaminar Fracture Toughness of Unidirectional Fiber-Reinforced Polymer Matrix Composites: ASTM International.

Davijani, A. A. B., Hajikhani, M., & Ahmadi, M. (2011). Acoustic Emission based on sentry function to monitor the initiation of delamination in composite materials. *Materials & Design, 32*(5), 3059-3065. doi: DOI 10.1016/j.matdes.2011.01.010

Diao, X., Ye, L., & Mai, Y.-W. (1997). Fatigue behaviour of CF/PEEK composite laminates made from commingled prepreg. Part II: statistical simulations. *Composites Part A: Applied Science and Manufacturing, 28*(8), 749-755. doi: http://dx.doi.org/10.1016/S1359-835X(97)00024-9

Donnet, J. (1998). *Carbon Fibers 3e*: Marcel Dekker.

Dornfeld, D., & Handy, C. (1987, Mar 1987). *Slip detection using acoustic emission signal analysis.* Paper presented at the Robotics and Automation. Proceedings. 1987 IEEE International Conference on.

Drinkwater, B. W., Castaings, M., & Hosten, B. (2003). The measurement of A(0) and S-0 Lamb wave attenuation to determine the normal and shear stiffnesses of a compressively loaded interface. *Journal of the Acoustical Society of America, 113*(6), 3161-3170. doi: 10.1121/1.1568754

E1316, A. (2013). Standard Terminology for Nondestructive Examinations: ASTM International.

Fan, Y., Gu, F., & Ball, A. (2010). Modelling acoustic emissions generated by sliding friction. *Wear, 268*(5–6), 811-815. doi: http://dx.doi.org/10.1016/j.wear.2009.12.010

Ferrer, C., Salas, F., Pascual, M., & Orozco, J. (2010). Discrete acoustic emission waves during stick–slip friction between steel samples. *Tribology International, 43*(1–2), 1-6. doi: http://dx.doi.org/10.1016/j.triboint.2009.02.009

Finlayson, R. D., Friesel, M. A., Carlos, M. F., Miller, R. K., & Godinez, V. (2000). *Acoustic emission structural health management systems (AE-SHMS).* Paper presented at the Proceedings of the SPIE.

Fotouhi, M., Pashmforoush, F., Ahmadi, M., & Oskouei, A. R. (2011). Monitoring the initiation and growth of delamination in composite materials using acoustic emission under quasi-static three-point bending test. *Journal of Reinforced Plastics and Composites, 30*(17), 1481-1493. doi: Doi 10.1177/0731684411415140

Ghosh, K. K., & Karbhari, V. M. (2007). Evaluation of strengthening through laboratory testing of FRP rehabilitated bridge decks after in-service loading. *Composite Structures, 77*(2), 206-222. doi: 10.1016/j.compstruct.2005.07.014

Giurgiutiu, V. (2007). *Structural Health Monitoring: with Piezoelectric Wafer Active Sensors*: Elsevier Science.

Harris, B. (2003). *Fatigue in Composites: Science and Technology of the Fatigue Response of Fibre-Reinforced Plastics*: Woodhead.

Hase, A., Wada, M., & Mishina, H. (2008). The relationship between acoustic emissions and wear particles for repeated dry rubbing. *Wear, 265*(5–6), 831-839. doi: http://dx.doi.org/10.1016/j.wear.2008.01.011

Haselbach, W., & Lauke, B. (2003). Acoustic emission of debonding between fibre and matrix to evaluate local adhesion. *Composites Science and Technology, 63*(15), 2155-2162. doi: http://dx.doi.org/10.1016/S0266-3538(03)00193-3

Hisakado, T., & Warashina, T. (1998). Relationship between friction and wear properties and acoustic emission characteristics: iron pin on hardened bearing steel disk. *Wear, 216*(1), 1-7. doi: http://dx.doi.org/10.1016/S0043-1648(98)00138-0

Huguet, S., Godin, N., Gaertner, R., Salmon, L., & Villard, D. (2002). Use of acoustic emission to identify damage modes in glass fibre reinforced polyester. *Composites Science and Technology, 62*(10–11), 1433-1444. doi: http://dx.doi.org/10.1016/S0266-3538(02)00087-8

Jayakumar, T., Mukhopadhyay, C. K., Venugopal, S., Mannan, S. L., & Raj, B. (2005). A review of the application of acoustic emission techniques for monitoring forming and grinding processes. *Journal of Materials Processing Technology, 159*(1), 48-61. doi: http://dx.doi.org/10.1016/j.jmatprotec.2004.01.034

Jibiki, T., Shima, M., Akita, H., & Tamura, M. (2001). A basic study of friction noise caused by fretting. *Wear, 251*(1–12), 1492-1503. doi: http://dx.doi.org/10.1016/S0043-1648(01)00792-X

Johnson, W. S., Fibers, A. C. D.-o. H. M., Composites, T., Aeronautics, U. S. N., & Administration, S. (1989). *Metal Matrix Composites: Testing, Analysis, and Failure Modes*: American Society for Testing & Materials.

Karbhari, V. M. (2004). Fiber reinforced composite bridge systems - transition from the laboratory to the field. *Composite Structures, 66*(1-4), 5-16. doi: 10.1016/j.compstruct.2004.04.026

Kaw, A. K. (2010). *Mechanics of Composite Materials, Second Edition*: Taylor & Francis.

Kerber, F., Sprenger, H., Niethammer, M., Luangvilai, K., & Jacobs, L. J. (2010). Attenuation Analysis of Lamb Waves Using the Chirplet Transform. *Eurasip Journal on Advances in Signal Processing*. doi: 375171

10.1155/2010/375171

Kostopoulos, V., Tsotra, P., Karapappas, P., Tsantzalis, S., Vavouliotis, A., Loutas, T. H., . . . Tanimoto, T. (2007). Mode I interlaminar fracture of CNF or/and PZT doped CFRPs via acoustic emission monitoring. *Composites Science and Technology, 67*(5), 822-828. doi: http://dx.doi.org/10.1016/j.compscitech.2006.02.038

Li, C. J., Li, S Y. (1995). Acoustic Emission Analysis for Bearing Condition Monitoring. *Wear, 185*, 67-74.

Loutas, T. H., & Kostopoulos, V. (2009). Health monitoring of carbon/carbon, woven reinforced composites. Damage assessment by using advanced signal processing techniques. Part I: Acoustic emission monitoring and damage mechanisms evolution. *Composites Science and Technology, 69*(2), 265-272. doi: http://dx.doi.org/10.1016/j.compscitech.2008.07.020

Martin, R. H., Fibers, A. C. D.-o. H. M., & Composites, T. (1995). *Composite Materials: Fatigue and Fracture, Fifth Volume*: ASTM.

Meriaux, J., Boinet, M., Fouvry, S., & Lenain, J. C. (2010). Identification of fretting fatigue crack propagation mechanisms using acoustic emission. *Tribology International, 43*(11), 2166-2174. doi: http://dx.doi.org/10.1016/j.triboint.2010.06.009

Miller, R. K., Hill, E. K., Moore, P. O., & Testing, A. S. f. N. (2005). *Acoustic emission testing*: American Society for Nondestructive Testing.

Milne, I., Ritchie, R. O., & Karihaloo, B. L. (2003). *Comprehensive Structural Integrity*: Elsevier Science.

Moser, F., Jacobs, L. J., & Qu, J. M. (1999). Modeling elastic wave propagation in waveguides with the finite element method. *NDT & E International, 32*(4), 225-234. doi: 10.1016/s0963-8695(98)00045-0

Ndiaye, I., Maslouhi, A., & Denault, J. (2000). Characterization of interfacial properties of composite materials by acoustic emission. *Polymer Composites, 21*(4), 595-604. doi: 10.1002/pc.10215

Ni, Q.-Q., & Iwamoto, M. (2002). Wavelet transform of acoustic emission signals in failure of model composites. *Engineering Fracture Mechanics, 69*(6), 717-728. doi: http://dx.doi.org/10.1016/S0013-7944(01)00105-9

Oskouei, A. R., Zucchelli, A., Ahmadi, M., & Minak, G. (2011). An integrated approach based on acoustic emission and mechanical information to evaluate the delamination fracture toughness at mode I in composite laminate. *Materials & Design, 32*(3), 1444-1455. doi: DOI 10.1016/j.matdes.2010.08.048

Pandya, K. S., Dharmane, L., Pothnis, J. R., Ravikumar, G., & Naik, N. K. (2012). Stress wave attenuation in composites during ballistic impact. *Polymer Testing, 31*(2), 261-266. doi: http://dx.doi.org/10.1016/j.polymertesting.2011.11.006

Rajendra, D., Knighton, T., Esterline, A., & Sundaresan, M. J. (2011). *Physics-based classification of acoustic emission waveforms.* Paper presented at the Proceedings of the SPIE, San Diego.

Ramadas, C., Balasubramaniam, K., Joshi, M., & Krishnarnurthy, C. V. (2011). Numerical and experimental studies on propagation of A(0) mode in a composite plate containing semi-

infinite delamination: Observation of turning modes. *Composite Structures, 93*(7), 1929-1938. doi: DOI 10.1016/j.compstruct.2011.01.025

Ramirez-Jimenez, C. R., Papadakis, N., Reynolds, N., Gan, T. H., Purnell, P., & Pharaoh, M. (2004). Identification of failure modes in glass/polypropylene composites by means of the primary frequency content of the acoustic emission event. *Composites Science and Technology, 64*(12), 1819-1827. doi: http://dx.doi.org/10.1016/j.compscitech.2004.01.008

Reifsnider, K. L., & Case, S. W. (2002). *Damage tolerance and durability of material systems*: Wiley Interscience.

Rose, J. L. (2004). Ultrasonic Waves in Solid Media.

Sause, M. G. R., Müller, T., Horoschenkoff, A., & Horn, S. (2012). Quantification of failure mechanisms in mode-I loading of fiber reinforced plastics utilizing acoustic emission analysis. *Composites Science and Technology, 72*(2), 167-174. doi: http://dx.doi.org/10.1016/j.compscitech.2011.10.013

Scheirs, J. (2000). *Compositional and Failure Analysis of Polymers: A Practical Approach*: Wiley.

Schubert, K. J., & Herrmann, A. S. (2011). On attenuation and measurement of Lamb waves in viscoelastic composites. *Composite Structures, 94*(1), 177-185. doi: 10.1016/j.compstruct.2011.07.003

Shull, P. J. (2002). *Nondestructive Evaluation: Theory, Techniques, and Applications*: Taylor & Francis.

Sridharan, S. (2008). *Delamination Behaviour of Composites*: Woodhead.

Staszewski, W. J., Boller, C., & Tomlinson, G. R. (2004). *Health Monitoring of Aerospace Structures: Smart Sensor Technologies and Signal Processing*: J. Wiley.

Sun, H., Xu, B., & Qian, R. (2009). Numerical simulation of laser-generated Lamb waves in viscoelastic materials by finite element method. *Journal of Applied Physics, 106*(7). doi: 073108

10.1063/1.3238247

Toutountzakis, T., Tan, C. K., & Mba, D. (2005). Application of acoustic emission to seeded gear fault detection. *NDT & E International, 38*(1), 27-36. doi: http://dx.doi.org/10.1016/j.ndteint.2004.06.008

Wandowski, T., Malinowski, P., Kudela, P., & Ostachowicz, W. (2011). Guided wave-based detection of delamination and matrix cracking in composite laminates. *Proceedings of the Institution of Mechanical Engineers Part C-Journal of Mechanical Engineering Science, 225*(C1), 123-131. doi: Doi 10.1243/09544062jmes1907

Appendix A

Attenuation coefficients – Chapter 4

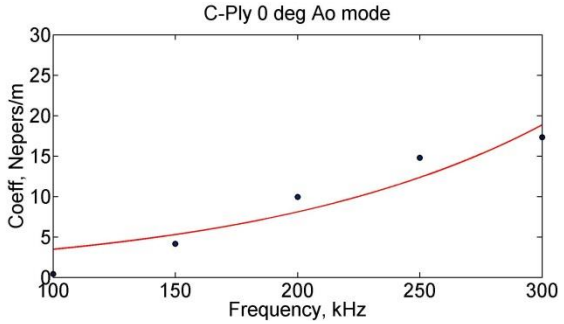

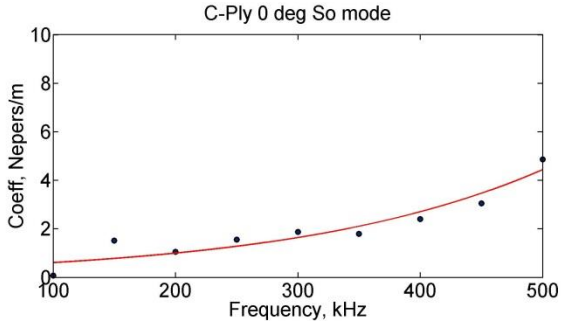

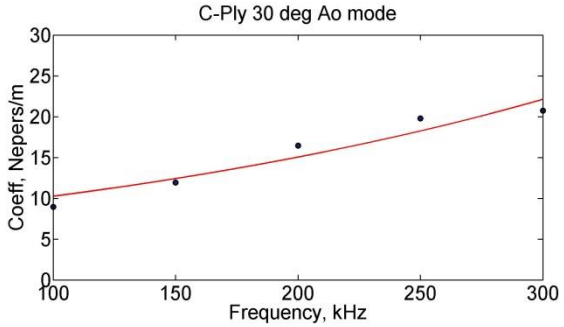

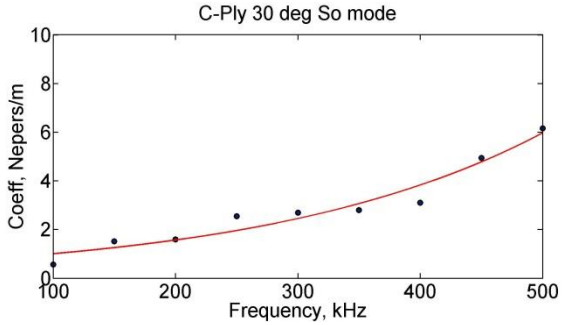

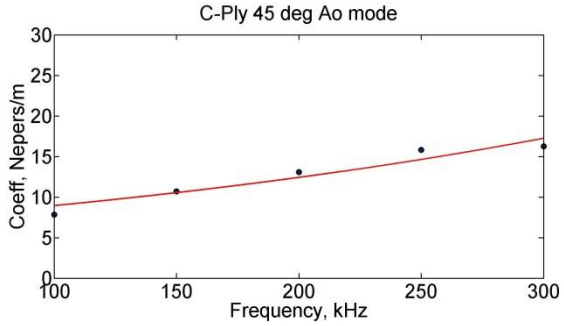

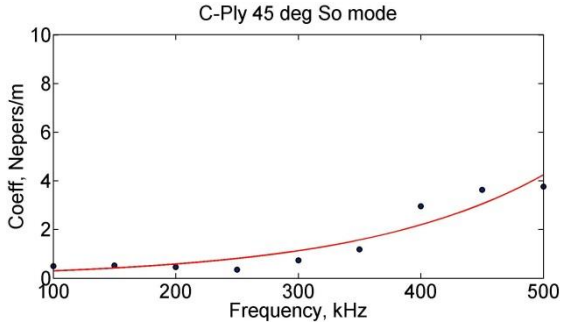

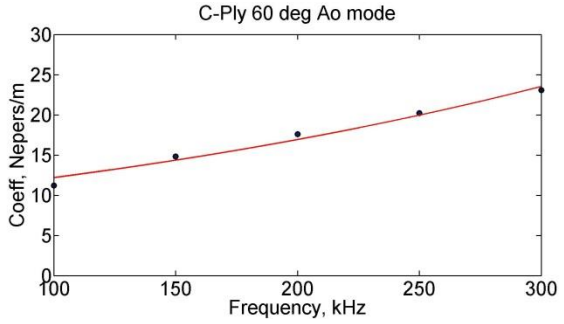

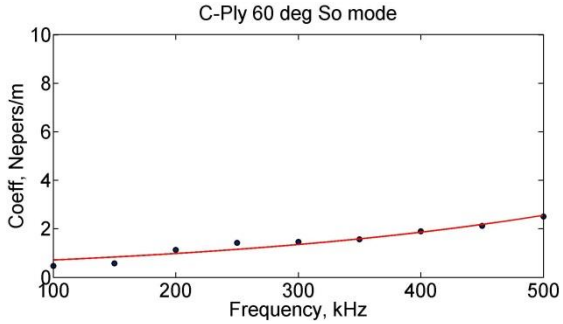

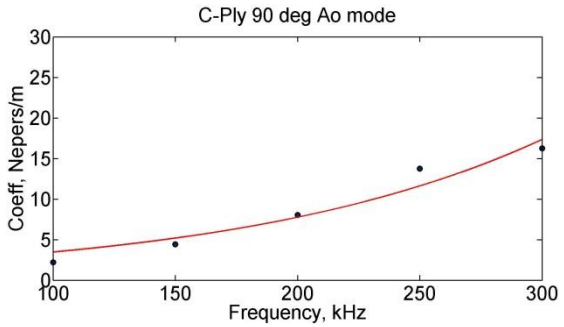
C-Ply 90 deg Ao mode
Coeff, Nepers/m
Frequency, kHz

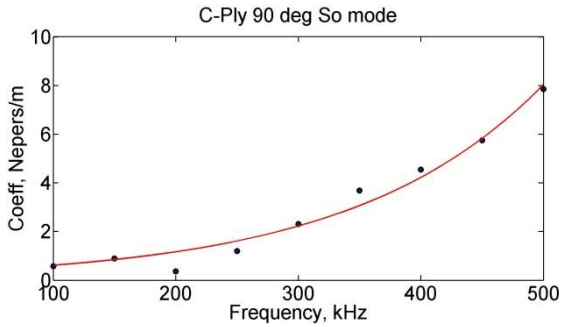
C-Ply 90 deg So mode
Coeff, Nepers/m
Frequency, kHz

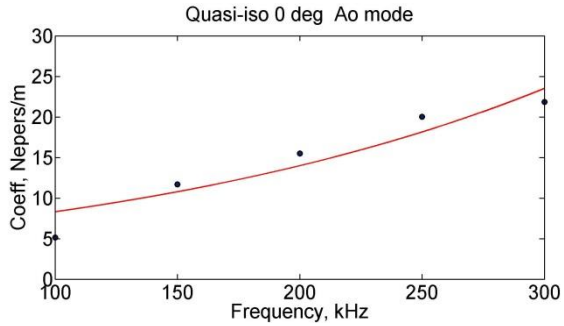
Quasi-iso 0 deg Ao mode
Coeff, Nepers/m
Frequency, kHz

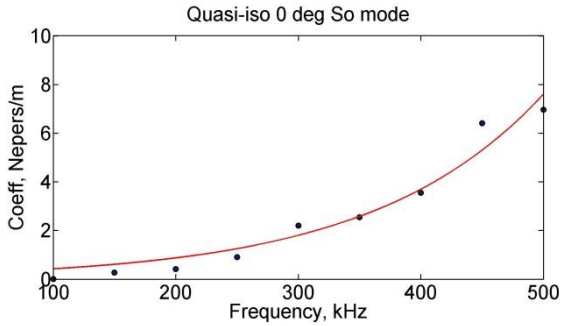
Quasi-iso 0 deg So mode
Coeff, Nepers/m
Frequency, kHz

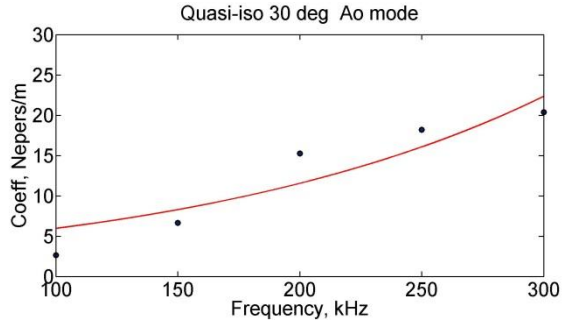
Quasi-iso 30 deg Ao mode
Coeff, Nepers/m
Frequency, kHz

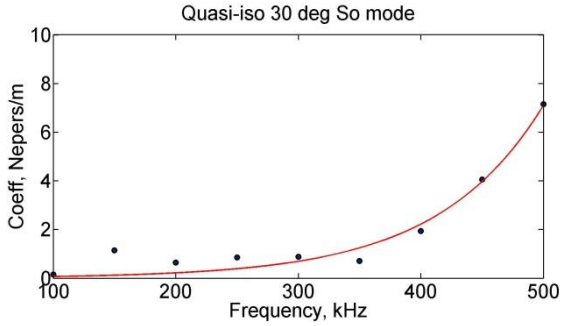
Quasi-iso 30 deg So mode
Coeff, Nepers/m
Frequency, kHz

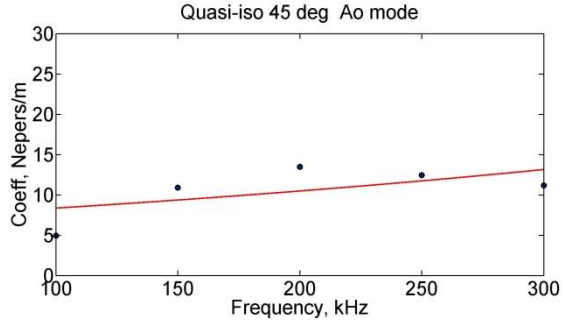
Quasi-iso 45 deg Ao mode
Coeff, Nepers/m
Frequency, kHz

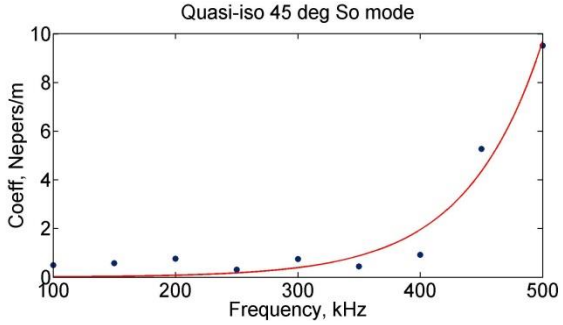
Quasi-iso 45 deg So mode
Coeff, Nepers/m
Frequency, kHz

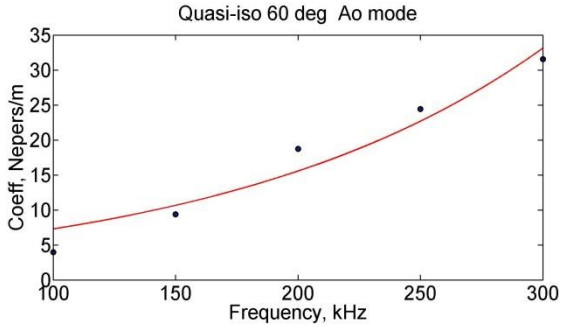
Quasi-iso 60 deg Ao mode
Coeff, Nepers/m
Frequency, kHz

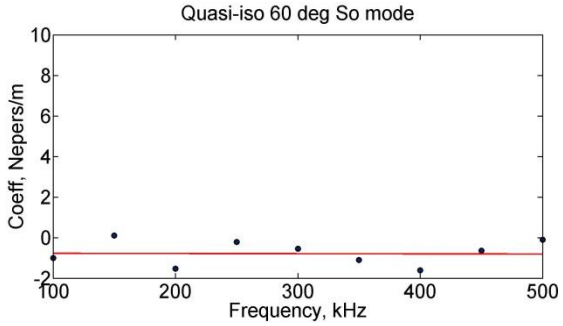
Quasi-iso 60 deg So mode
Coeff, Nepers/m
Frequency, kHz

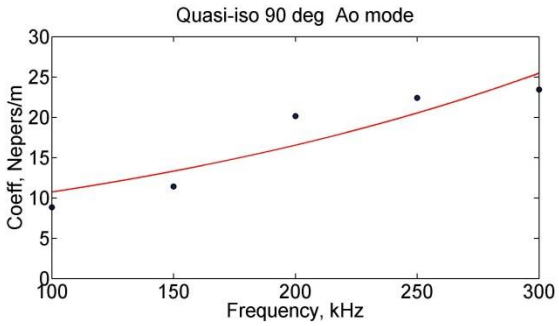
Quasi-iso 90 deg Ao mode
Coeff, Nepers/m
Frequency, kHz
0
5
10
15
20
25
30
100
150
200
250
300

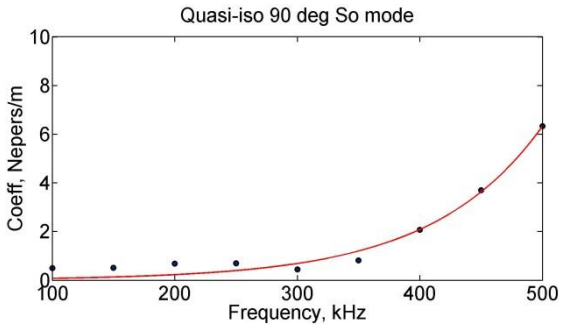
Quasi-iso 90 deg So mode
Coeff, Nepers/m
Frequency, kHz
0
2
4
6
8
10
100
200
300
400
500

Appendix B

MATLAB Code to correlate experimental crack growth signal and numerical AE waveform - Chapter 6

```
% Input the experimental crack and fretting signals
% Input the rectangular pulse with its respective location
clc
clear
n1 = load('60AVERAGE_Task_18.txt'); %rectangular pulse signal from
simulation% don't forget to specify location
n2 = load('43_1.txt'); %crack signal from PAC in one column
n3 = load('FRETTING_SIGNAL.txt'); %fretting signal from PAC in one column

%%%%%%%%%%%%%%%%%%%%%%%%%%%%%% plot of the waveforms %%%%%%%%%%%%%%%%%%

plot(n1(:,1), n1(:,2));
hold on
plot(0:2E-7:(length(n2)-1237)*2E-7,n2(1237:length(n2),1)*max(n1)/max(n2),'r')
hold off

%%%%%%%%%%%%%%%%%%%%%%%% resampling the rectangular pulse to 0.2us interval

x=n1(:,1);%x-xoordinate values
y=n1(:,2);%y-coordinate values
v=0;%initializing the intermediate values
j=1;%index for matrix of interpolated values
m=0;%initializing the matrix for interpolated values

for i=1:1100
    if x(i)== v
        m(j)=y(i);
        j=j+1;
        v=v+2E-7;
    else if (x(i)<= v)&&(x(i+1)>= v)
        m(j)=((v-x(i))/(x(i+1)-x(i)))*(y(i+1)-y(i))+y(i);
        j=j+1;
        v=v+2E-7;
        else
            a = 1;
        end
    end
end

m; %numerical signal resampled at 0.2 us that is the same as crack and
fretting signals


%%%%%%%%%%%%%%%%%% resampling the rectangular pulse at 1 nano-sec interval

b=length(m');
m_01=0;
for j=1:b-1
```

```
    h=(j-1)*200+1;
    for j2=1:200
        m_01(h)= m(j)+((j2-1)/200)*(m(j+1)-m(j));
        h=h+1;
    end
end
m_01;
num_0001=m_01; % numerical rectangular unit signal sampled at 1nano-sec
length(num_0001);

size(num_0001)


%%%%%%%%%%%%%%%%%%%%% resampling crack signals at 1nano-sec interval

b=length(n2);
m_01=0;
for j=1:b-1
    h=(j-1)*200+1;
    for j2=1:200
        m_01(h)= n2(j)+((j2-1)/200)*(n2(j+1)-n2(j));
        h=h+1;
    end
end
m_01;
c_0001=m_01; % crack signal sampled at 1nano-sec
size(c_0001)


%%%%%%%%%%%%%%%%%%%%% resampling fretting signals at 1nano-sec interval

b=length(n3);
m_01=0;
for j=1:b-1
    h=(j-1)*200+1;
    for j2=1:200
        m_01(h)= n3(j)+((j2-1)/200)*(n3(j+1)-n3(j));
        h=h+1;
    end
end
m_01;
f_0001=m_01; % fretting signal sampled at 1nano-sec

%%%%%%%%%%%%%%%%correlation%%%%%%%%%%%%%%%%%%%%%%%%%%%

t=1:1:50000;
t=t*1E-9;

n1_1 = num_0001(1:50000); %
n2_1 = c_0001(247001:247000+50000);
n3_1 = f_0001(247001:247000+50000);

%correlation with crack signal
figure(1)
% subplot(2,1,1)
```

```
plot(t*1E6,n1_1*(1/0.1336)), xlabel('Time, \mus'), ylabel('Normalized
Amplitude')
hold on
plot(t*1E6,n2_1*(max(n1_1)/max(n2_1))*(1/0.1336),'r');%experimental crack red
hold off
R_2 = xcorr(n1_1,n2_1,'coeff');
R2=max(abs(R_2))
% subplot(2,1,2)
% plot(R2)


%correlation with fretting signal
figure(2)
% subplot(2,1,1)
plot(t*1E-6,n1_1*(1/0.1336)), xlabel('Time, \mus'), ylabel('Normalized
Amplitude')
hold on
plot(t,n3_1*(max(n1_1)/max(n3_1))*(1/0.1136),'r');%experimental fretting red
hold off
R_3 = xcorr(n1_1,n3_1,'coeff');
% subplot(2,1,2)
R3=max(abs(R_3))
% plot(R3)
```